

Dissertation for the degree of Philosophiae Doctor (PhD)

# Aspects of Electron Dynamics in Atoms Exposed to Single Cycle Electromagnetic Pulses

*Michaela Chovancová*



Department of Physics and Technology  
Februar 2018



# Abstract

This thesis covers the topic in atomic physics: Interaction of strong external field with Rydberg hydrogen atom. In three scientific publications, we have targeted physical processes such as the field ionization in the strong terahertz field, back-scattering in the Coulomb field and spatial transport of electrons.

First two of them deal with the study of the ionization of the Rydberg atoms in the terahertz field. Rydberg atoms are highly excited stabilized states with very big dipole moments which makes them very sensitive to the external field. As external field we use THz radiation, submillimeter radiation in the range of  $100\text{ }\mu\text{m}$  -  $1\text{ mm}$ , which generators are in the state-of-the-art development. Specifically, we treat with linearly polarized single-cycle pulses with high intensity and picosecond duration. High intensity and low frequency brings us to the strong field, where the field is so strong, that Coulomb potential may be deformed and field ionization is possible.

Driving linearly polarized single-cycle pulse is only bidirectional, the electron is driven mostly to the one direction by the field in the first half of the cycle and to the opposite direction in the second half of the pulse. Affirmation is given by the observing of the probability density during the field propagation.

When some pulse asymmetry is included, then it involves new phenomena, which we have observed at different energy level of initial Rydberg states. While 15-d state may be ionized already in the first half of the pulse, where the sinus pulse has the opposite direction to the second half, lower energy states (6-d and 9-d) are ionized at the second half of the pulse with a higher peak intensity, at the opposite direction. Therefore, 15d electron has lower emission energy compare to lower lying Rydberg states.

We have numerically simulated the experiment published in April 2014 by Li and Sha (University of Virginia), where sodium d-Rydberg atoms have been ionized by single-cycle pulse with the duration 10-100 longer than electron Rydberg period and the ionization probability with increasing field strength has been measured. Curves in our simulation grow sigmoidally with the ionization scaling law  $n^{-3}$  for the field strength. This field strength scaling is inversely proportional to the binding energy of electrons in an atom and is valid for all of the probabilities, since all scaled probability curves meet at the same place on a plot. Explanation of this scaling law and mechanism behind is the main target of this thesis.

Ionization of bounded electrons by strong laser pulses occurs most frequently as over the barrier ionization, tunneling or multiphoton ionization. In the recent studies of single cycle THz pulse ionization, displacement ionization has been introduced: In this case the electron is ionized suddenly, at a specified very short time kick and a specified pulse strength and is displaced in one direction opposite to the field. It follows that during the pulse, the ionized electron never recombines with the parent nucleus.

After our 3D analysis of wavefunction we concluded that the ionization takes the place mostly during the period around the field maxima. We suppose that the ionization is caused partly by the tunneling ionization for the field strength scaled as  $n^{-3}$  and partly as the over the barrier ionization scaled with the field strength as  $n^{-4}$ .

The third paper comes with the spatial transport of an electron, when an electron is driven by

the short strong external pulse(s). To observe this phenomena, the laser pulse frequency and the field intensity must be high enough, so that we can neglect the effect of the Coulomb potential. Then wavefunction is translated almost without any distortion to a well defined distance from the origin. This distance depends just on the set up laser intensity and the frequency.

In quantum mechanics, wavefunction is propagated on the grid by the split-step operator and two-step Euler method. Classical simulations are calculated by the classical Monte Carlo method (CTMC). In this case, the initial state is modelled as the statistical microcanonical ensemble with set up boundary conditions . The classical differential equations are numerically solved by Euler method and Runge-Kutta method.

## Acknowledgement

I want to thank to the whole department for giving me the opportunity to study this doctoral programme. I have been the part of the Optic and Atomic Physics group, where the atmosphere is friendly and supportive.

First of all, I want to thank my supervisor Prof. Jan Petter Hansen for all his work, friendly support and patience with me. I want to also thank to my co-supervisor Prof. Em. Ladislav Kocbach for discussions and suggestions to my work, to Dr. Hicham Agueny, the postdoc. in the Atomic Physics group at UiB, who has been developing code for the paper II. He is also the corresponding author of the paper II. I thank also to Jørgen Rørstad for his valuable master thesis and for all his help with CTMC computations.

My special thanks belongs to MSc. Jakub Višňák for his comments to my thesis and my family for their support.

I feel very grateful for having the opportunity to travel inside Norway and also to other countries for conferences and summer schools.



# Contents

Abstract . . . . .	3
Acknowledgements . . . . .	5
<b>1 Introduction</b>	<b>9</b>
<b>2 Atoms and their interaction with electromagnetic fields: Semiclassical theory</b>	<b>11</b>
2.1 Classical electromagnetic field . . . . .	11
2.2 Schrödinger Equations of the Atom . . . . .	12
2.3 Interaction between atoms and electromagnetic fields . . . . .	16
<b>3 Atoms and their interaction with electromagnetic fields: CTMC</b>	<b>19</b>
3.1 Initial states . . . . .	20
3.2 Dynamics and Final State Analysis . . . . .	22
<b>4 Numerical methods</b>	<b>25</b>
4.1 Three-point finite difference method . . . . .	25
4.2 Crank-Nicolson method . . . . .	26
4.3 Split-operator operator Fourier method . . . . .	26
4.4 Split-operator operator Fourier method in spherical coordinates . . . . .	27
4.5 Split-operator operator Fourier method in cylindrical coordinates . . . . .	28
4.6 Propagation of Classical Dynamics . . . . .	30
<b>5 Scope of the work</b>	<b>33</b>
<b>6 Conclusion and outlook</b>	<b>37</b>
Bibliography . . . . .	39
<b>7 Scientific Results</b>	<b>43</b>
List of Papers . . . . .	45
Paper I . . . . .	47
Paper II . . . . .	57
Paper III . . . . .	69
<b>Appendices</b>	<b>81</b>





# Chapter 1

## Introduction

A discrete world consisting of the smallest indivisible particles called atoms was first proposed by Democritus in the ancient Greece. After a long period, in the end of the 19th century, sir Joseph Thompson discovered the first subatomic particle, the electron, in a beam of cathode rays in vacuum tube [1]. By electron deflection in electric and magnetic fields he was able to measure the ratio of the charge to the mass of the electron. He found that electrons are order of thousand times lighter than hydrogen atoms [2]. Soon after, in 1911, Rutherford discovered a localised positive field in the middle of an atom by scattering of alpha particles on the golden foil [3]. These two experiments established an atom, neutral as a whole, consisting of a small dense positively charged nucleus with negatively charged electrons around.

The theoretical basis for quantum mechanics is commonly seen to have started with the explanation of the emission spectrum of a *black body* at fixed temperature,  $T$ <sup>1</sup>. According to the classical theory, we cannot describe the black body radiation energy density function  $\rho(T, \nu)d\nu$  in the short-wavelength limit, because it produces infinite radiation intensity. The German physicist Max Planck was able to fit experimental data of the black body radiation curve with a new distribution function. The function, now called the Planck curve, depended on a new constant  $h \sim 6.6310^{-34}$  Js [4], later called Planck's constant. Using this, Einstein was in 1905 able to explain the photoelectric effect [5]. He assumed that light is a stream of particles, light quanta, each with energy  $E = h\nu$ . The word *photon* for a quantum of light was for the 1<sup>st</sup> time used by Gilbert N. Lewis 21 years after Einstein's explanation.

In 1913 Niels Bohr explained the emission spectra of hydrogen given by a completely new model. [6]. He assumed that angular momentum  $l$ , in certain stable states are quantised in integer numbers of  $\hbar = h/2\pi$ , ie.  $l = n\hbar$ . When using classical mechanics and this assumption, the energy levels of discrete states appear as

$$E = -\frac{Ry}{n^2}, \quad (1.1)$$

where the Rydberg constant is  $Ry \sim 13.6$  eV. The notion of stable trajectories remained a contradiction to classical electromagnetic theory, where all accelerating particles radiates energy.

A wave-particle duality valid for any particle on the small scale were proposed by Louis de Broglie in 1924 in his dissertation, where he quantifies the (non-relativistic) particle wavelength as  $\lambda = h/p$ , where  $p$  is the particle momentum [7]. To defend the equation in his thesis,

---

<sup>1</sup>A black body is an idealized body defined by its capability to emit and absorb electromagnetic radiation at any wavelength

de Broglie suggested electron scattering and diffraction experiments as an experimental test. This experiment was carried out in 1927 by Davisson and Germer [8]. The same year, G. P. Thompson and A. Reid observed interference pattern of electrons, by passing a beam of electrons through a thin metal film [9]. Interference pattern from a single-electron double slit experiment was obtained by Merli, Missiroli and Pozzi as late as in 1976 [10].

A grand challenge of physics became the quest for an equation valid on the atomic and subatomic level and being an equivalent to Newton's equation on the macroscopic scale. The problem was solved by Erwin Schrödinger in 1926 as he has assigned to a particle a complex wave function,  $\psi(r,t)$  which satisfy a second-order time dependent or time independent linear partial differential equation [11]. The equations, today known as the Schrödinger Equation and the time-dependent Schrödinger Equation, became a cornerstone of modern physics. The time dependent equation is written on his gravestone in Alpbach, Austria. The interpretation of the wavefunction has been an ongoing branch of quantum physics and philosophy ever since its invention. The most accepted one originates from Max Born [12, 13]. His statistical interpretation defines  $|\psi(r,t)|^2 d^3r$  as the the probability that a particle is located around a region  $d^3r$  at a time  $t$ .

We can experience application of quantum physics, quantum technologies, everywhere around us today. Atomic clocks define a second very accurately in terms of two energy states in the caesium atom. Coherent light from lasers is possible due to the population inversion of quantum states by stimulated emission. Transistors, semi-conductors and diodes in electronic devices are designed with the knowledge of quantum energy states and quantum phenomena such as tunnelling and the quantum Hall effect [14]. Based on the quantum tunneling we can detect magnetic and electric field very accurately, up to  $10^{-18}$  scale in respective SI units. In fact, material science, chemistry, medicine and industry have all been developed based on the development of quantum physics. Nowadays, experiments shedding light on the fundamentals of quantum mechanics continue. For example, less than two decades ago, attosecond pulses opened the way for researchers to follow electronic motion inside atoms and molecules [15, 16]. As it has become possible to make one layer diffraction slits atomic size, we can catch high-resolution images of complex organic molecules [17, 18]. Research on control of coherent quantum state [19] is very promising for applications in spintronics and quantum information [20, 21]. These are only few examples from a jungle of ongoing current research. The present thesis, and the results, connects to all of the examples above. We study electron propagation inside a single atom and discuss conditions for quantum control and potential applications for imaging.

This thesis consists of a general introduction to methods and theories of which the scientific results in the form of three published papers and developed programs have been based. It follows this introduction as four chapters ending with conclusion and outlook. For generality we use SI units with a few exceptions in this first section of Chapter 2. In the remaining part of the thesis and in the scientific papers we apply more conveniently atomic units. The connection between the two sets of units is defined in appendix. A second appendix details the development of a scattering formula applied in paper II.

## Chapter 2

# Atoms and their interaction with electromagnetic fields: Semiclassical theory

At the most fundamental level, charged particles and their time dependent interaction with strong electromagnetic fields would be described by quantum field theory. We are not aware of any such schemes being formulated and it would indeed in the end require a prohibitive amount computational resources. A less unrealistic treatment would be to consider atoms as composed non-relativistic particles interacting with a quantized photon field. This is a standard approach for atoms interacting with few photon fields. However, strong fields imply extremely large photon numbers, which without simplifications would fill the memory of any computer several times. And on the other hand, from the perspective of the field, the physical properties are hardly altered by a tiny interaction with a single atom. This suggests a semiclassical approximation where the atom is treated in quantum mechanical terms and interacts with a classical time dependent electromagnetic field. This approach has a long standing history in collision physics [22]. For electromagnetic fields it was formally derived by Briggs and Rost as late as in 2001 [23]. Thus, the photon field is described by Maxwell's equations and the interaction with matter takes place through the interaction part of the Hamiltonian. In the following sub-chapters this approach is described in detail.

### 2.1 Classical electromagnetic field

As early as in 1865 Maxwell had managed to unified general laws of the electromagnetic radiation into four equations [24]. In atomic physics it is particularly useful to introduce Maxwell equations in terms of the two mathematical quantities, a scalar potential ( $\phi$ ) and a vector potential ( $\mathbf{A}$ ),

$$-\nabla^2 \phi + \left( \frac{1}{c^2} \frac{\partial^2 \phi}{\partial t^2} \right) = \frac{\rho}{\epsilon_0} \quad (2.1)$$

$$-\nabla^2 \mathbf{A} + \frac{1}{c^2} \frac{\partial^2 \mathbf{A}}{\partial t^2} = \mu_0 \mathbf{J}, \quad (2.2)$$

Here the speed of light is  $c = 1/\sqrt{(\epsilon_0 \mu_0)}$  is  $\sim 137$  a.u., the permeability of vacuum is  $\epsilon_0$  and the magnetic permittivity of vacuum is  $\mu_0$ . The equations here are presented in the Lorenz

gauge, where  $\nabla \cdot \mathbf{A} = -\partial\phi/(c\partial t)$ . The electric and magnetic fields can be expressed by the potentials as

$$\mathbf{B}(\mathbf{r}, t) = \nabla \times \mathbf{A}(\mathbf{r}, t) \quad (2.3)$$

$$\mathbf{E}(\mathbf{r}, t) = -\nabla\phi(\mathbf{r}, t) - \frac{1}{c} \frac{d\mathbf{A}(\mathbf{r}, t)}{dt} \quad (2.4)$$

The potential representation has four variables  $\phi$ ,  $A_x$ ,  $A_y$  and  $A_z$  in contrast to 6 given by the electric and magnetic fields. This opens for certain freedoms (gauge choices) in choosing the potentials to work with. In strong field physics, we can take  $\phi = 0$ , ie. no point charges, and  $\nabla \cdot \mathbf{A} = 0$ . The latter condition is called the "Coulomb gauge" but can be seen as a special case of the Lorenz gauge. The solution of Maxwell's equations in free space is then a set of plane waves of the form

$$\mathbf{A}(\mathbf{r}, t) = A_0 \hat{\epsilon} \cos(\mathbf{k} \cdot \mathbf{r} - \omega t) \quad (2.5)$$

where  $\omega$  is the frequency of the oscillation,  $\mathbf{k}$  is the wave vector with the magnitude  $k = \omega/c$ ,  $A_0$  is the wave amplitude directed along the polarization unitary vector  $\hat{\epsilon}$ . From Eq. (2.4) we obtain the electric field,

$$\mathbf{E}(\mathbf{r}, t) = E_0 \hat{\epsilon} \sin(\mathbf{k} \cdot \mathbf{r} - \omega t) \quad (2.6)$$

with  $E_0 = \omega A_0$ . The magnetic field becomes perpendicular to the electric field,

$$\mathbf{B} = (\mathbf{k} \times \hat{\epsilon}) A_0 \cos(\mathbf{k} \cdot \mathbf{r} - \omega t) \quad (2.7)$$

Comparing amplitudes of electric and magnetic field  $E_0/B_0 = \frac{\omega}{|\mathbf{k}|} = c$ , we observe that the magnetic field strength is  $1/c$  smaller than the electric field strength. Considering further, the wavelength of the external fields  $\lambda = 2\pi c/\omega$ , we realize that it is, for field frequencies normally well below unity, orders of magnitude larger than the size of atoms. This verifies the widely used dipole approximation where the spatial dependence of the vector field is ignored across the atom,

$$\mathbf{A}(\mathbf{r}, t) \sim A_0 \hat{\epsilon} \cos(\omega t). \quad (2.8)$$

This results in a corresponding simplified approximate electromagnetic field as well

$$\mathbf{E}(\mathbf{r}, t) \sim \omega E_0 \hat{\epsilon} \sin(\omega t) \quad (2.9)$$

and a vanishing magnetic field. Any constant phase shift may be added to this expression. This approximation is applied throughout the present work. Even if Rydberg atoms are large and extend up to hundreds of a.u., the angular frequencies are in the range from  $10^{-5} - 10^{-3}$  a.u., giving  $137/\omega$  is in the range  $10^3 - 10^6$ .

## 2.2 Schrödinger Equations of the Atom

In 1926 Schrödinger published wave-equations of a bound particle based on Hamiltonian  $\hat{H}$ , the operator of the system energy [11], acting on a new object, the wave-function. He introduced first the time-independent equation (TISE), which solutions are stationary states with discrete or a continuous set of energy values. Later the same year, a time dependent equation was put forward

(TDSE) to describe quantum dynamics. These equations substitute Newton's mechanics on the sub-micrometer scale. For his discovery of "new productive forms of atomic theory" he received the Nobel Prize in Physics 1933 together with Paul Adrien Maurice Dirac. The same year Heisenberg received the Nobel Prize for 1932 for having, one year before Schrödinger, developed a separate operator based approach to quantum mechanics. In one of the six famous papers of Schrödinger in 1926 he demonstrates that Heisenbergs and his own formalism leads to completely identical results. The time-independent Schrödinger equation is an eigenvalue equation

$$\hat{H}\Psi(\mathbf{r}) = E\Psi(\mathbf{r}) \quad (2.10)$$

where  $\hat{H} = \hat{p}^2/2 + V(\hat{r})$  is the quantized form of the classical Hamiltonian of the particle and  $E$  is the energy. The quantization rule is  $\hat{p}_i = -\frac{\partial}{\partial x_i}$  and  $\hat{x}_i = x_i$ , and leads to the following three-dimensional Hamiltonian operator for a single electron

$$\hat{H} = -\frac{1}{2}\nabla^2 + V(\mathbf{r}) \quad (2.11)$$

Here the first term represents the kinetic energy and the second term is the potential energy. There are a number of potential energy cases for which the TISE can be solved analytically, e.g.,  $V = 0$  (free particle),  $V = 1/2\omega^2\mathbf{r}^2$  (harmonic oscillator) and  $V = -1/\mathbf{r}$  (hydrogen atom). For arbitrary potentials, analytical solutions are not known. But the equation may in this case always be solved numerically. In case of atoms with many interacting electrons, there are no analytical solutions at all and even numerical solutions can become difficult to achieve.

The details of the solution for bound states of the hydrogen atom are now outlined as a short example of a solvable system. The Coulomb potential then suggest the use of spherical coordinates, where the position of an electron is given by the radius  $r$ , azimuthal angle  $\phi$  and zenith angle  $\theta$ . The scalar operator  $\nabla^2$  (2.11) takes the form

$$\nabla^2 = \frac{1}{r^2} \frac{\partial}{\partial r} (r^2 \frac{\partial}{\partial r}) + \frac{1}{r^2 \sin \theta} \frac{\partial}{\partial \theta} (\sin \theta \frac{\partial}{\partial \theta}) + \frac{1}{r^2 \sin^2 \theta} \frac{\partial^2}{\partial \phi^2} \quad (2.12)$$

which can be shortened as

$$\nabla^2 = \frac{1}{r^2} \frac{\partial}{\partial r} (r^2 \frac{\partial}{\partial r}) - \frac{\hat{L}^2}{r^2} \quad (2.13)$$

with  $\hat{\mathbf{L}}$  being the angular momentum operator. The TISE for a hydrogen like atom now takes the form

$$\left[ -\frac{1}{2} \left( \frac{\partial^2}{\partial r^2} + \frac{2}{r} \frac{\partial}{\partial r} - \frac{1}{r^2} \hat{L}^2 \right) - \frac{Z}{r} \right] \Psi(r, \theta, \phi) = E\Psi(r, \theta, \phi) \quad (2.14)$$

The solution  $\Psi(r, \theta, \phi)$  can be separated in a radial part  $R_{n,l}(r)$  and spherical harmonics eigenfunctions  $Y_l^{m_l}(\theta, \phi)$ . Three quantum numbers appear,  $n$  is principal quantum number,  $l$  is angular quantum number,  $m_l$  is the projection of angular quantum number on the arbitrary chosen  $z$ -axis,

$$\begin{aligned} n &\in 1, 2, \dots \\ l &\in 0, 1, \dots, n-1 \\ m_l &\in -l, \dots, l \end{aligned} \quad (2.15)$$

Each set  $(n, l, m)$  defines a possible eigenstate with energy 1.1.

$$E_n = -\frac{1}{2n^2} \quad (2.16)$$

The eigenstate takes the form

$$\Psi_{n,l,m_l}(\mathbf{r}, \theta, \phi) = R_{n,l}(r)Y_l^{m_l}(\theta, \phi) = R_{n,l}(r)Y_l^{m_l}(\theta)e^{im_l\phi} \quad (2.17)$$

The radial solution of the Schrödinger equation has a general form of a product of the normalized condition, power function, polynomial and exponential part,

$$R_{n,l}(r) = N_{n,l}r^l\tilde{P}_{n,l}(r)e^{(-Zr/n)} \quad (2.18)$$

where  $N_{n,l}$  is the normalization constant and  $P_{n,l}(r)$  is a polynomial in  $r$ . We note the exponential damping which sets the scale of the state  $n$ . The angular part has a general form

$$Y_l^{m_l} = A_{l,m_l}P_l^{m_l}(\cos(\theta))e^{im_l\phi} \quad (2.19)$$

where  $A_{l,m_l}$  is the norm of spherical harmonics functions,  $P_l^{m_l}$  are associated Legendre polynomials. To each state at the hydrogen energy level with number  $n$  are assigned  $n - 1$  states with different angular momentum  $l$ . This is due the fact, that angular momentum  $l_z$  is quantized. Similarly, for given values of  $n$  and  $l$ , there are  $(2l + 1)$  states with  $m_l = -l, 0, \dots, l$ , which are degenerated. The degree of degeneracy of the energy level  $E_n$  is therefore  $\sum_{l=0}^{n-1}(2l + 1) = n^2$ , and this degeneracy is a trademark of the Coulomb potential only.

A common numerical approach for obtaining approximate solutions to the eigenstates is to take advantage of the expansion of the wavefunction in a known analytical basis of  $N$  eigenstates  $[\phi_i(\mathbf{r})]$  which forms an orthonormal basis. Explicitly inserted in the TISE,

$$\sum_{i=0}^N \left[ -\frac{1}{2} \nabla^2 + V(\mathbf{r}) \right] c_i \phi_i(\mathbf{r}) = E \sum_{i=0}^N c_i \phi_i(\mathbf{r}) \quad (2.20)$$

To obtain the solution we multiply eq. (2.20) sequentially by all basis functions  $\phi_j$  from the left and obtain an eigenvalue problem for the vector of expansion coefficients,  $\mathbf{c} = (c_0, c_1 \dots c_N)$

$$\mathbf{H}\mathbf{c} = E\mathbf{c} \quad (2.21)$$

Now  $\mathbf{H}$  becomes a matrix with elements,

$$H_{i,j} = \int d^3r \phi_i^*(\mathbf{r}) \left[ -\frac{1}{2} \nabla^2 + V(\mathbf{r}) \right] \phi_j(\mathbf{r}) \quad (2.22)$$

The integrals needs to be calculated in advance, and this particular operation depends heavily on the choice of basis functions. The number of basis functions necessary for convergence is also strongly sensitive to the type of basis functions. A vast number of algorithms and packages are available for diagonalization.

The time-dependent Schrödinger equation, TDSE, has the form

$$i\frac{\partial \Psi(\mathbf{r}, t)}{\partial t} = \hat{H}\Psi(\mathbf{r}, t) \quad (2.23)$$

When the Hamiltonian is independent of time, the solution of the TDSE is separable and reduces to the TISE for a time independent wavefunction  $\psi(r)$ . The time dependent solution becomes

$$\psi(\mathbf{r}, t) = \psi(\mathbf{r})e^{-iEt} \quad (2.24)$$

where  $E$  is the separation constant which is associated with the energy. A time-dependent Hamiltonian often has a well known spectrum of states at the initial time,  $t = 0$ ,  $\psi_n(\mathbf{r}, t = 0)$ , where  $n$  can take a finite or infinite values. A common *ansatz* is then to express the time dependent wavefunction in terms of a linear time-dependent sum of the spectrum of states,

$$\psi(\mathbf{r}, t) = \sum_{n=0}^N c_n(t) \psi_n(\mathbf{r}) \quad (2.25)$$

If the system initially is in the first state we have  $c_n(t = 0) = \delta_{n,0}$ . Further more, the amplitudes can be interpreted as the probability of the system to be in the state  $n$  at given time  $t$ . More formally, the solution of the TDSE can be written as

$$\psi_n(\mathbf{r}, t) = \hat{U}(t_0, t) \psi_n(\mathbf{r}, t_0) \quad (2.26)$$

where  $\hat{U}$  is a unitary time-evolution operator and takes a form

$$\hat{U}(t_0, t) = e^{-i \int_{t_0}^t \hat{H}(t-t_0) dt} \quad (2.27)$$

We can derive the unitary operator from the TDSE

$$i \frac{\partial \hat{U}}{\partial t} = \hat{H} \hat{U} \quad (2.28)$$

The unitary operator is transitive

$$\hat{U}(t_1, t_2) \hat{U}(t_2, t_3) = \hat{U}(t_1, t_3) \quad (2.29)$$

$$\hat{U}(t_2, t_1) = \hat{U}^{-1}(t_1, t_2) = \hat{U}^\dagger(t_1, t_2) \quad (2.30)$$

This implies that the norm of the state  $\psi(r, t_1)$  is not changed during the time-propagation,

$$\frac{d}{dt} \int_{\mathbb{R}^3} \psi^*(\mathbf{r}, t_1) \psi(\mathbf{r}, t_1) dr = 0, \quad \forall t \quad (2.31)$$

If the Hamiltonian commute with itself at different times  $[\hat{H}(t_0), \hat{H}(t)] = 0$  and we consider a small timestep  $t - t_0 \ll 1$  an approximate expression of the time-evolution operator becomes,

$$\hat{U}(t_0, t) = e^{-i\hat{H}(t-t_0)} \quad (2.32)$$

This approximation is a useful starting point for numerical algorithms, as will be discussed in Chapter 4. In theory, space and basis are infinite, but in practice we need to work in the finite space and time. Thus, any numerical discretization involves at least some level of approximation (truncation error). In our case space grid is very large ( $10^5$  a.u.) with the smooth absorber on both edges, so that a wavefunction was kept mostly on the grid during the propagation. We assume the absorbed part of the wavefunction to be in continuum.

## 2.3 Interaction between atoms and electromagnetic fields

The interaction between the quantum mechanical atom and the predefined, time-dependent electromagnetic free ( $\phi = 0$ ) field is now described in the dipole approximation through the Hamiltonian

$$\hat{H}^{VG} = \frac{1}{2} [\hat{\mathbf{p}} - \mathbf{A}]^2 + V(\hat{r}) = \hat{H}_0 + \underbrace{\mathbf{A} \cdot \hat{\mathbf{p}} + \frac{\mathbf{A}^2}{2}}_{\hat{H}_i} \quad (2.33)$$

The first term  $\hat{H}_0$  describes the Hamiltonian of the atom while the second term describes the interaction of atom with the field. Within the dipole approximation, the last term with  $\mathbf{A}^2$  is just a time-dependent phase, which can be removed from the numerical scheme by multiplying with a global phase factor

$$\psi^{VG}(\mathbf{r}, t) \rightarrow \psi^{VG}(\mathbf{r}, t) e^{\left(-\frac{i}{2} \int_{t_0}^t \mathbf{A}^2(t') dt'\right)} \quad (2.34)$$

We arrive at the following expression for the TDSE

$$\left[ \frac{\hat{\mathbf{p}}^2}{2} + V(r) - \mathbf{A} \cdot \hat{\mathbf{p}} - i \frac{\partial}{\partial t} \right] \psi^{VG}(\mathbf{r}, t) = 0 \quad (2.35)$$

with the interaction term now reduced to  $\hat{H}_i = \mathbf{A} \cdot \hat{\mathbf{p}}$ . An alternative expression in terms of the electric field  $\mathbf{E}$  is

$$\left[ \frac{\hat{\mathbf{p}}^2}{2} + V(\hat{r}) - \mathbf{r} \cdot \mathbf{E} - i \frac{\partial}{\partial t} \right] \psi'^{LG}(\mathbf{r}, t) = 0 \quad (2.36)$$

where the term in the parenthesis represents the Hamiltonian in the length gauge. We can transform the wavefunction from the velocity gauge to length gauge via

$$\psi^{LG}(\mathbf{r}, t) = e^{-i\mathbf{r} \cdot \mathbf{A}(t)} \psi^{VG}(\mathbf{r}, t) \quad (2.37)$$

which can be shown by inserting the latter expression in Eq. (2.33). An alternative expression in terms of the electromagnetic field itself is the moving Kramers-Henneberger frame (KH). We can transform the Hamiltonian as  $\hat{H}^{KH} = \hat{T}^{-1} \hat{H} \hat{T}$  to a moving frame centered at  $\boldsymbol{\alpha}(t)$  by

$$\hat{T} = e^{-i\boldsymbol{\alpha}(t) \cdot \hat{\mathbf{p}}} \quad (2.38)$$

where the translation (or displacement) vector  $\boldsymbol{\alpha}(t) = -\int_{t_0}^t \mathbf{A}(t') dt'$ . Thus, any eigenstate of the Hamiltonian, where  $\boldsymbol{\alpha}(t) = 0$  transforms to frame with origin at  $\boldsymbol{\alpha}(t)$  as,

$$\Psi_n^{KH}(\mathbf{r} - \boldsymbol{\alpha}(t), t) = e^{i\boldsymbol{\alpha}(t) \cdot \hat{\mathbf{p}}} \Psi_n^{VG}(\mathbf{r}, t) \quad (2.39)$$

The time-dependent Schrödinger equation in the KH frame then becomes

$$\left[ \frac{\hat{\mathbf{p}}^2}{2} + V[\mathbf{r} - \boldsymbol{\alpha}(t)] - i \frac{\partial}{\partial t} \right] \psi^{KH}(\mathbf{r} - \boldsymbol{\alpha}(t), t) = 0 \quad (2.40)$$

The displacement vector  $\boldsymbol{\alpha}(t)$  describes the rest frame of a free classical particle in the oscillating field. In this frame the particle is exposed to the time-dependent nuclear potential  $V(\mathbf{r} - \boldsymbol{\alpha}(t))$  which can cause transitions among states described in a stationary frame.



In principle the number of alternative transformations of the Hamiltonian is infinite. The three representations here derived do however dominate applications for which the dipole approximations hold. None of them are superior to other in the general case. The VG, in combination with expansions in terms of spherical harmonics, has shown to be most effective for strong pulse physics [28]. In certain cases, in particular when intra shell dynamics in Rydberg atoms are considered, the length gauge has certain advantages. The LG additionally has the convenient property that the kinetic and canonical momentum are equal while in VG the canonical momentum is  $\mathbf{p} - \mathbf{A}(t) = \mathbf{p} - \dot{\alpha}(t)$ . Finally, in situations where the field is so strong that the entire wavefunction remains localized around the displacement parameter, the KH frame is advantageous.

We end this chapter with a short discussion of an applied single cycle pulse in the present work. It is inspired by an experiment published in 2014 by Li and Jones [26]. The electric  $z$ -polarized field  $\mathbf{E}(t) = E(t)\mathbf{e}_z$ , is given as,

$$E(t) = \begin{cases} -E_0 \sin(\omega t), & \text{if } -T < t < 0 \\ -E_0 \beta \sin(\beta \omega t), & \text{if } T/\beta > t > 0 \\ 0 & \text{otherwise} \end{cases} \quad (2.41)$$

where for the experimental pulse in [26]  $\beta = 1.5$  fits reasonable well the experimental features. The analytical form of the vector field is then

$$A(t) = \begin{cases} -\frac{E_0}{\omega} \cos(\omega t + 1), & \text{if } -T < t < 0 \\ -\frac{E_0}{\omega} \beta \cos(\beta \omega t + 1), & \text{if } T/\beta > t > 0 \\ 0 & \text{otherwise} \end{cases} \quad (2.42)$$

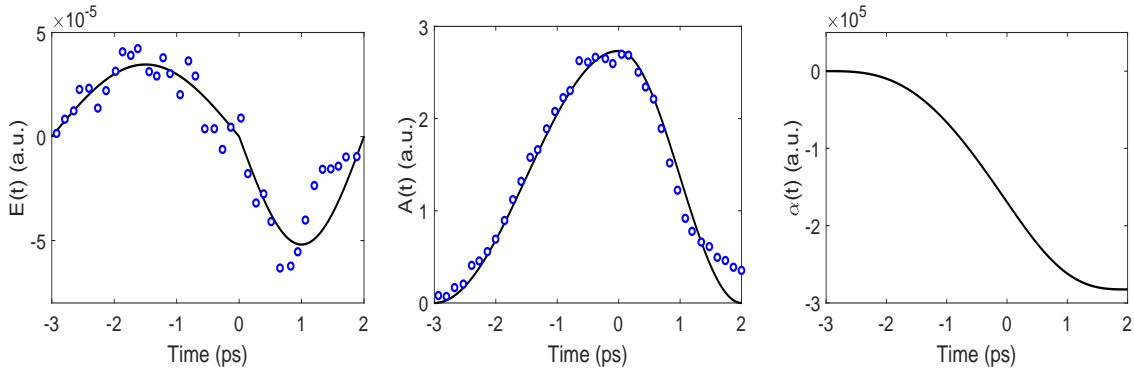


**Figure 2.1:** Time dependence of the the electric field strength  $E(t)$  (lef) along the  $z$ -direction and the vector potential  $A(t)$  (middle) for a single-cycle pulse. The black line represents the model pulse and the blue dots are experimental data [26]. The right panel shows the displacement  $\alpha(t)$  eq. (2.43).

Finally the displacement becomes

$$\alpha(t) = \begin{cases} -\frac{E_0}{\omega}(t+T) - \frac{E_0}{\omega^2} \sin(\omega t), & \text{if } -T < t < 0 \\ -\frac{E_0}{\omega}(t+T) - \frac{E_0}{\beta \omega^2} \sin(\beta \omega t), & \text{if } T/\beta > t > 0 \\ 0 & \text{otherwise} \end{cases}$$

The electric pulse is characterized by a positive first half cycle and a slightly shorter and more intense negative half cycle. When exposing this pulse shape to excited atoms it will, for sufficiently strong peak field parameter  $E_0$ , ionize a part or the entire atom. The electron is brought to the continuum and accelerated in along the negative  $z$ -direction. At some point the field turns and the positive acceleration brings the electron to a standstill or to a back-propagation towards the nucleus. Thus, the main part of the electron spectrum in this case is expected to scatter in the positive direction. Note the order of magnitude difference in pulse strength between the vector potential and the electric field. Correspondingly, the value of  $\alpha(T/\beta)$  becomes very large. This poses a particular challenge for numerical simulations, to be described in Chapter 4.

## Chapter 3

# Atoms and their interaction with electromagnetic fields: CTMC

Even though the behaviour of electrons in atoms is governed by quantum mechanics, it can be useful to have a classical model to help understanding of ongoing processes. However, quantum mechanics is probabilistic in the nature. Therefore, by classical physics we cannot describe pure quantum phenomena like for example tunnelling or interference. Nevertheless we may set up a completely classical model where the electrons are propagated according to Newton's laws and investigate to which extent it reproduces the quantum calculations. This requires, of course, that the atom interact with the electromagnetic field solely through the Lorentz force.

A classical method used here is called the classical trajectory monte carlo (CTMC). This method uses a large ensemble of identical particles, a microcanonical distribution, which identifies possible states of a studied system by allowed number of particles  $N$ , volume  $v$  and energy  $E_0$ . In fact, these three values  $N, v, E_0$  are initial conditions to the equations given by the classical mechanics. To simulate atomic states, the notion of electronic trajectories around nucleus with fixed energy  $E_0 = -0.5/n^2$  is deployed. First we define a set of all possible positions and momenta pictured as radial microcanonical distributions, all these possible states are developed in time by the deterministic Newton's differential equations, which gives us initial trajectories around the nucleus and set of final positions and momenta for analysis after interacting with the electromagnetic field.

Monte Carlo methods were invented by Stanislaw Ulam, Nicholas Metropolis and von Neumann in the 1940's [29, 30]. Abrines and Percival described the CTMC method in the original article [31] with initial states based on microcanonical ensembles. The method was demonstrated in collisions between the ground state hydrogen and proton and the ionization and charge-transfer cross sections have been computed. As the method resulted in cross sections and electron spectra in relatively good agreement with experiments [31, 32], it became popular and further developed and extended. Reinhold and Falcón [33] simplified the microcanonical distribution to the form as described in this chapter.

Adding the quantum phases of the electron along a classical electron trajectory makes possible to even reconstruct the interference pattern of photoelectron emission spectra [35, 36] or diffraction patterns [37]. This approach is based on Feynman path integrals [38] and defines so called quantum-trajectory methods. The classical action,

$$S(r_1, t_1; r_0, t_0) = \int_{t_0}^{t_1} L(\mathbf{x}(t), \mathbf{v}(t), t) dt, \quad (3.1)$$

where  $L(\mathbf{x}(t), \mathbf{v}(t), t)$  is the Lagrangian of an electron, is recorded and used for weighting of the final states.

In general this method requires much larger sets of initial states and have not been explored in the present work. In the next sections we will describe the Reihold-Falcón method step-by-step in the context of how it has been applied in this work. The section ends with a review of related, and more advanced, applications.

### 3.1 Initial states

Initial atomic states for electron in a static nucleus potential are represented by the microcanonical distribution in an available specific volume  $\mathbf{v}(\mathbf{r})$ . Possible spatial coordinates are determined by the conservation law for energy and the assumption, that kinetic energy  $E_k = p^2/2\mu$  cannot be negative,

$$E_k = E_0 - V(\mathbf{r}) \geq 0 \quad (3.2)$$

Here  $\mu \approx 1$  a.u. is the reduced mass of the two-body system,  $\mathbf{p}$  is the magnitude of momentum and  $V(\mathbf{r})$  is the Coulomb potential. Further more,  $E_0$  is the initial energy determined by the Bohr condition 1.1. Therefore the maximal value for the position of an electron  $r_{max}$  is given by the condition

$$E_0 - V(\mathbf{r}) = 0 \quad (3.3)$$

Assuming that the above equation has only one root confines the size of the allowed radii interval to  $0 < r < r_{max}$ . The distribution of initial states are selected from the microcanonical distribution

$$\rho(\mathbf{r}, \mathbf{p}, E) = D d^3r d^3p \delta(E_0 - E) \quad (3.4)$$

where the system energy  $E = E_k + V(\mathbf{r})$ ,  $D$  is a constant depending only on the available volume  $\mathbf{v}(\mathbf{r})$ . This function has  $6N$  dimensional support and the delta function peaks when  $E = E_0$ . Therefore we obtain restrictions on the available volume enclosed by the energy hyperspace  $E_0$ . The transformation to spherical coordinates reads

$$d^3r d^3p \rightarrow r^2 dr d(\cos(\theta_r)) d\phi_r p^2 dp d\cos(\theta_p) d\phi_p \quad (3.5)$$

While momentum  $p$  and radius  $r$  are non-uniformly distributed, angles  $\theta_r$ ,  $\theta_p$  are spread over half-sphere  $\theta \in [0, \pi]$ . The azimuthal angles  $\phi_r$ ,  $\phi_p$  are uniformly distributed in whole sphere  $\phi \in [0, 2\pi]$ . What remains is the distribution of  $(r, p)$  described by the integral,

$$\delta(E - E_0) p^2 dp r^2 dr \quad (3.6)$$

By using the substitution  $p^2 dp = p \mu dE$ , since  $E = p^2/(2\mu) + V(r)$  we require,

$$\int_0^E p \mu \delta(E - E_0) dE = \mu p(E_0, r) \quad (3.7)$$

where  $E_0 \in (0, E)$  and  $p(E_0) = \sqrt{p(E_0)2\mu(E - V(r))}$ . Finally, we rewrite  $\omega(r)$  in terms of only  $r$ -coordinate and initial condition  $E_0$ ,

$$\omega(r, E_0) = \int_0^{r_{max}} \mu p(E_0, r') r'^2 dr' = \int_0^{r_{max}} \rho(E_0, r') dr' \quad (3.8)$$

Fixing the momentum as  $p(E_0, r)$ , secure radii within the interval  $\langle 0, r_{max} \rangle$ . Therefore  $\omega(r, E_0)$  is uniformly distributed on the interval  $\langle 0, \omega_{r_{max}} \rangle$ . A random selection then allows for the computation of spatial coordinates

$$\begin{aligned} x &= r(\omega) \sqrt{1 - t_r} \cos(\phi_r) \\ y &= r(\omega) \sqrt{1 - t_r} \sin(\phi_r) \\ z &= r(\omega) t_r \end{aligned} \quad (3.9)$$

and momentum coordinates as

$$\begin{aligned} p_x &= p(r(\omega)) \sqrt{1 - t_p} \cos(\phi_p) \\ p_y &= p(r(\omega)) \sqrt{1 - t_p} \sin(\phi_p) \\ p_z &= p(r(\omega)) t_p. \end{aligned} \quad (3.10)$$

Thus we have reduced the  $6N - 6$  dimensional phase-space to the space defined only by  $\omega(r)$  and random angle  $\phi(r)$  on r-sphere and p-sphere respectively. The orbital momentum is a pseudovector defined by  $\mathbf{l} = \mathbf{r} \times \mathbf{p} = -\mathbf{r} \times -\mathbf{p}$ , which is symmetric to the inverse operation. The components are

$$\begin{aligned} l_x &= y \cdot p_z - z \cdot p_y \\ l_y &= z \cdot p_x - x \cdot p_z \\ l_z &= x \cdot p_y - y \cdot p_x \end{aligned} \quad (3.11)$$

The magnitude of the angular momentum is  $l^2 = l_x^2 + l_y^2 + l_z^2$ . In our calculations, the microcanonical distribution of position is confined by setting the angular momentum in z.direction from  $l_z - 0.5$  to  $l_z + 0.5$ , which reflects a quantum uncertainty in  $l_z$  vs.  $l$ .

As an example, we compare in Fig. (3.1) the radial distribution of initial states for a 1s and a 9d state of hydrogen. We observe that the classical distributions vanish at the classical turning point  $2n^2$  as expected, while the quantum mechanical densities does not. Apart from that, the two distributions are on an order of magnitude view in agreement. It is in general seen to be quite different from the quantum mechanical probability distribution. Nevertheless we have a distribution of stable initial states of the same order of magnitude as the quantum distribution and from that starting point the outcome of classical calculations may be invoked and compared to quantum calculations.

In the first scientific work of this thesis we consider a one-dimensional (1D) model problem. This require a slight modification of the 3D procedure above. Consider now a single spatial variable ( $z$ ) and the momentum ( $p$ ). The microcanonical distribution becomes,

$$D dz dp \delta(E(z, p) - E_0) \quad (3.12)$$

Compared to the 3D-case, the terms  $r^2 dr$  and  $p^2 dp$  become simply  $dz$  and  $dp$  and therefore 1D microcanonical distribution  $w$  is computed from the form

$$w(z) = \int_0^z \frac{\mu}{p(z')} dz' = \int_0^z \frac{\mu}{\sqrt{2\mu(E_0 - V(z'))}} dz' \quad (3.13)$$

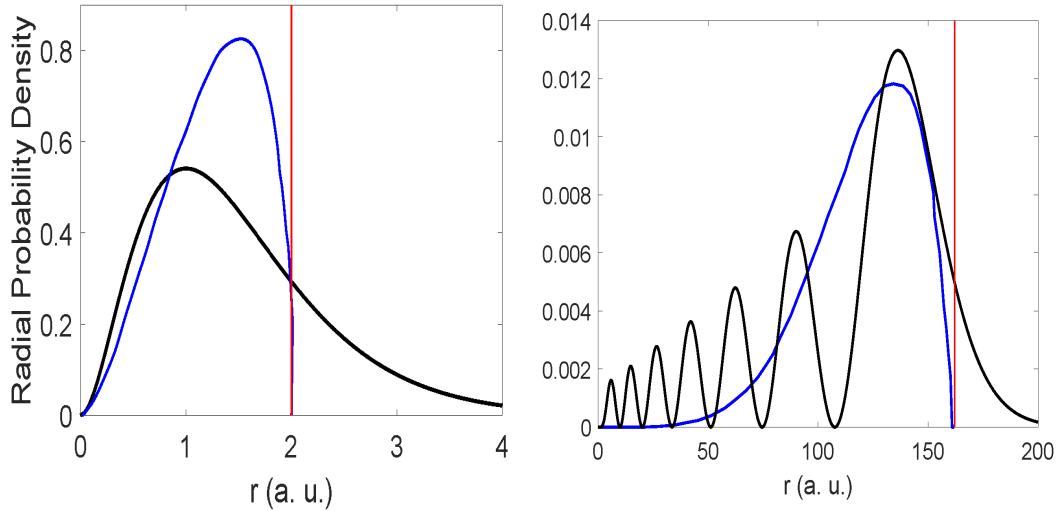


**Figure 3.1:** Comparison of the 3D-CTMC microcanonical distribution and quantum (black solid line in a.u.) probability density  $|\Psi(r)|^2$  for initial states 1s (left) and 9d (right). The vertical red asymptote shows the classical turning point  $2n^2$ .

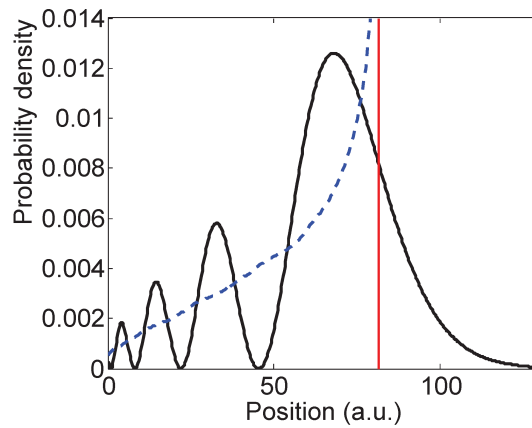


**Figure 3.2:** 1D-CTMC electron microcanonical distribution for initial states 9d in the positive-half of x-coordinate showing as dotted blue line. The solid black line shows quantum mechanical electron probability density  $|\Psi_r|^2$  spreads over positive-half x-coordinate in set-up potential described in [34]. Red vertical asymptote shows classical turning point.

In Fig. (3.2) the classical 1D distribution is compared with a quantum distribution of the 9th excited states. Due to the 1D space the classical distribution diverges at the turning point. Apart from that and again as in 3D, it compares relatively well with the quantum state.

## 3.2 Dynamics and Final State Analysis

With a set of initial conditions at hand we can propagate each set of electron coordinates under influence of the Coulomb force from the nucleus and the Lorentz force from the electromagnetic

field, in this case,

$$\begin{aligned}\frac{d\mathbf{r}}{dt} &= \frac{\mathbf{p}}{\mu} \\ \frac{d\mathbf{p}}{dt} &= -\frac{1}{r^2}\mathbf{e}_r + \mathbf{E}\end{aligned}\quad (3.14)$$

We observe that these equations takes the form of a coupled first order differential equations, which can be expressed in vector form

$$\frac{d}{dt}\mathbf{a} = \mathbf{b}(t, \mathbf{a}) \quad (3.15)$$

The 6 (3D) or 2 (1D) equations are solved numerically for arbitrary number of initial states using numerical methods described in the next chapter. In the end of the propagation we obtain a series of positions and momenta at every time-step of the propagation.

For illustration we select two single initial states of 9d and plot the trajectory of electron under the driving field. In the Fig. 3.3 the field is 1 kV/cm and the electron is seen to remain around the nucleus for all times, only being slightly perturbed by the electromagnetic field. In Fig. 3.4 the pulse strenght is much stronger, 360 kV/cm, and the electron is seen to be ionized after just a few trajectories around the nucleus. When ionized it propagates along the negative z-direction before it turns and is accelerated in the positive direction in accordance with the given pulse shape, cf. Eq. (2.41)

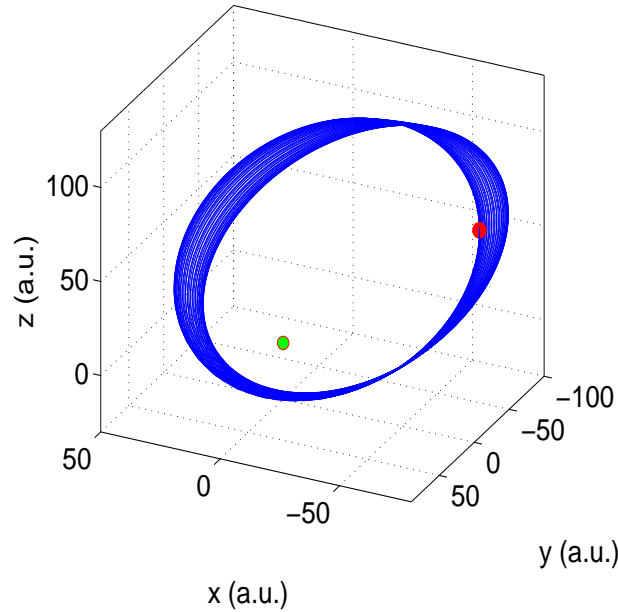


**Figure 3.3:** The calculated CTMC trajectory (left) as it developed in time for the initial state 9d under a single cycle THz field with strength  $E_0 = 1$  kV/cm. The nucleus is shown as the green augmented point at  $[0,0]$  and the starting point at  $t_0$  as the red point.

The disitribution of final state position for a large number of initial states in terms of the final  $(z, r)$  coordinates are should in Fig. (3.4). The blue dots correspond to initial states which remains bounded after the pulse, the black dots are ionized ones with final energy  $E \geq 0$ . Note the tendency of ionized electrons to end up with positive z-values. The electrons with largest z-values comes from ionization in the second half cycle. The lowest z-values of ionized electrons originate from situations where the electron is ionized in the first half cycle.

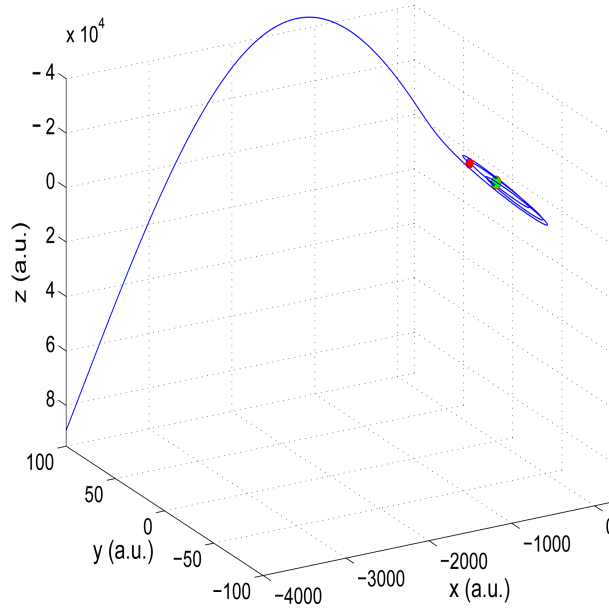


**Figure 3.4:** The calculated CTMC trajectory (left) as it develops in time for the initial state 9d under single cycle THz field with strength  $E_0 = 360$  kV/cm. The nucleus is shown as the green augmented point at  $[0,0]$  and the starting point at  $t_0$  as the red point.

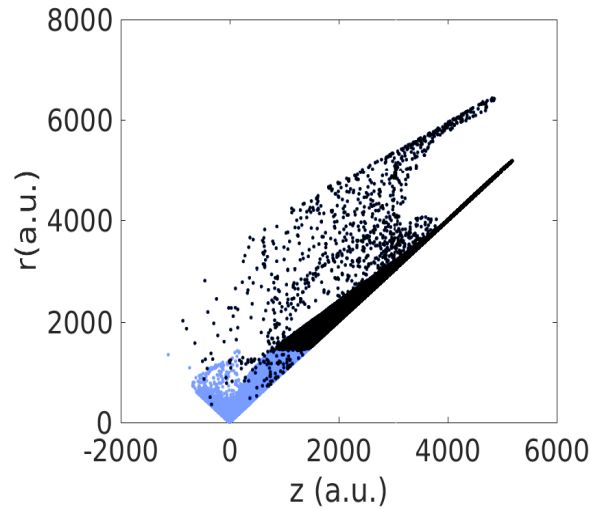


**Figure 3.5:** Map in  $(r, z)$  of final states for initial  $n=5000$  states and 50% of ionization probability. Black dots show ionized states.



# Chapter 4

## Numerical methods

In this chapter we will review numerical methods for time propagation which has been applied at various stages during the course of this work. It includes numerical schemes for 1D and 3D quantum and classical dynamics. The first three sections describe algorithms to propagate the TDSE only. The final section describes methods to solve coupled first order differential equations on the form of Eq. (3.15). As described in Chapter 1, an approximate solution of the TDSE at small time-step  $\Delta t$  after the time  $t_0$  can be approximated as

$$\psi(\mathbf{r}, t = t_0 + \Delta t) \simeq \psi(\mathbf{r}, t_0) e^{-i\hat{H}\Delta t} \quad (4.1)$$

Here the wave function (vector)  $\psi(\mathbf{r}, t_0)$  describes the state at  $t = t_0$ . When this state is known, the challenge is to apply the best possible approximation for the exponential operator in front. What is “best” may depend on the structure of the Hamiltonian, the initial state and the problem parameters (integration time, field strength etc.).

### 4.1 Three-point finite difference method

The discretization of the space-time allow us to compute the wavefunction on a grid. A family of methods called the finite-difference method (FDM) take advantage of this procedure. A derivative at one point is approximated by the differentiate operator computed from the neighbourhood grid-points. The time is discretized in the interval  $\langle t_0, \dots, t_{end} \rangle$  and we approximate the first-order derivative in time as the differentiation

$$\frac{\partial \psi(\mathbf{x}, t)}{\partial t} = \lim_{\Delta t \rightarrow 0} \frac{\psi(t + \Delta t, \mathbf{x}) - \psi(t, \mathbf{x})}{\Delta t} \quad (4.2)$$

We then obtain the solution in the next time-step  $\psi(t + \Delta t, \mathbf{x})$  from the previous step  $\psi(t, \mathbf{x})$ . First we expand a function as the Taylor series

$$\psi(t + \Delta t, \mathbf{x}) = \psi(t, \mathbf{x}) + \Delta t \left( \frac{\partial \psi(t, \mathbf{x})}{\partial t} \right) + \mathcal{O}(\Delta t) \quad (4.3)$$

The forward scheme in combination with the backward scheme

$$\psi(t - \Delta t, \mathbf{x}) = \psi(t, \mathbf{x}) - \Delta t \left( \frac{\partial \psi(t, \mathbf{x})}{\partial t} \right) + \mathcal{O}(\Delta t) \quad (4.4)$$

results in the more accurate central difference method based on one forward and one backward step, also called the two-step Euler method

$$\frac{\partial \psi(t, \mathbf{x})}{\partial t} = \frac{\psi(t + \Delta t, \mathbf{x}) - \psi(t - \Delta t, \mathbf{x})}{2\Delta t} + \mathcal{O}(\Delta t^2) \quad (4.5)$$

Adding the two equations together results in the three-point method as

$$\psi(t + \Delta t, \mathbf{x}) = \psi(t - \Delta t, \mathbf{x}) - 2i\hat{H}\Delta t\psi(t, \mathbf{x}) \quad (4.6)$$

This 1D-scheme can be extended for y and z coordinates and a similar procedure can be applied to discretize the space variable. This approximation is stable and of second order accuracy in  $\Delta t$ . However, it requires generally very small time steps to remain stable [40]. In addition it is extremely well conditioned for parallelization.

## 4.2 Crank-Nicolson method

A stabilized FDM is the implicit Crank-Nicolson method (CN) [41], which combines Euler's forward time-step with the backward time-step method. The CN time-evolution operator is derived from the 1st order expansion of the exponential series of the evolutionary operator

$$\hat{U}(t_{k+1}, t_k) \simeq \hat{I} - i\Delta t \hat{H} \quad (4.7)$$

for small  $\Delta t$ . The inverse operator correspondingly becomes,

$$\hat{U}^{-1}(t_{k+1}, t_k) \simeq \hat{I} + i\Delta t \hat{H} \quad (4.8)$$

Then, the forward time step is given explicitly as

$$\psi(t_{k+1/2}, \mathbf{x}) = [\hat{I} - i\frac{\Delta t}{2}\hat{H}(t_{k+1/2})]\psi(t_k, \mathbf{x}) \quad (4.9)$$

Since we want to reverse the time-evolution operator, the full step

$$\psi(t_{k+1}, \mathbf{x}) = \hat{U}(t_{k+1}, t_{k+1/2})\hat{U}(t_{k+1/2}, t_k)\psi(t_k, \mathbf{x}) \quad (4.10)$$

can be rewritten,

$$\hat{U}^{-1}(t_{k+1}, t_{k+1/2})\psi(t_{k+1}, \mathbf{x}) = \hat{U}(t_{k+1/2}, t_k)\psi(t_k, \mathbf{x}) \quad (4.11)$$

Using the first order approximation for the time development operators we obtain the numerical scheme called the Crank-Nicolson method or sometimes the Cayley-propagator,

$$\left[1 + i\frac{\Delta t}{2}\hat{H}(t_{k+1/2})\right]\psi(t_{k+1}, \mathbf{x}) = \left[1 - i\frac{\Delta t}{2}\hat{H}(t_{k+1/2})\right]\psi(t_k, \mathbf{x}) \quad (4.12)$$

Representing  $\psi$  on as a vector with reference to a basis we obtain  $\hat{H}$  as a matrix. The first step on the right side becomes a matrix-vector multiplication and the final step requires a matrix inversion. The implicit CN method is unconditionally stable and accurate up to  $\mathcal{O}(\Delta t^3)$ . However, the matrix inversion is generally time consuming unless the matrix is sparse.

## 4.3 Split-operator operator Fourier method

While the previous methods are well suited for 1D problems, they fast become intractable to 3D models. The reason is the replacement by a second derivative with the full Laplacian operator. An alternative is then to take advantage of basis expansions in terms of spherical harmonics and combine that with a representation of the radial expansion coefficients in the momentum space and the Fast Fourier Transform (FFT) algorithm. In 1D the expansion in spherical harmonics

can be omitted and we discretize space in  $x \in \langle x_0..x_N \rangle$  uniformly with  $N = 2^n$  points. In the momentum space we correspondingly obtain,  $p \in \langle k_0..k_N \rangle$ . The discrete points in  $p$ -space are related to the  $x$ -discretization as

$$k_n = \frac{2\pi}{n\Delta x}, n = -N/2, -N/2 + 1, \dots, N/2 \quad (4.13)$$

The wave function in the momentum space can now be computed as the FFT of the wavefunction in coordinate space and vica versa,

$$\tilde{\psi}(k_n) = \hat{F}\psi(x) = \Delta x \frac{1}{\sqrt{2\pi}} \sum_{m=0}^N e^{-ik_n x_m} \psi(x_m) \quad (4.14)$$

Here  $F$  denotes the Fourier transformation. The inverse Fourier transformation gives back the wave function in the coordinate space,

$$\psi(x_m) = \hat{F}^{-1}\tilde{\psi}(k_n) = \Delta p \frac{1}{\sqrt{2\pi}} \sum_{n=0}^N e^{ik_n x_m} \tilde{\psi}(k_n) \quad (4.15)$$

Note that the Fourier transformation is unitary, ie.  $\psi(\mathbf{x})$ , since Fourier transformation is the unitary transformation  $\hat{F} \times \hat{F}^\dagger = 1$ . The time evolution operator contains kinetic and potential energy operators is now split into two terms

$$\hat{U}(t + \Delta t, t) \simeq \exp(-i\hat{T}\Delta t) \exp(-i\hat{V}\Delta t) \quad (4.16)$$

which introduce a splitting error of second order,  $\mathcal{O}(\Delta t^2)$ . A more accurate expression is a separation of one of the operator, here kinetic operator, in two half steps

$$\begin{aligned} \hat{U}(t + \Delta t/2, t) &\simeq \exp(-i\hat{T}\Delta t/2) \exp(-i\hat{V}\Delta t/2) \\ \hat{U}(t + \Delta t, t + \Delta t/2) &\simeq \exp(-i\hat{V}\Delta t/2) \exp(-i\hat{T}\Delta t/2) \end{aligned}$$

The product of these two expressions gives for a full step

$$\hat{U}(t + \Delta t, t) \simeq \exp(-i\hat{T}\Delta t/2) \exp(-i\hat{V}\Delta t) \exp(-i\hat{T}\Delta t/2) \quad (4.17)$$

which has an error of order  $\mathcal{O}(\Delta t^3)$ . The trick is now to let each exponential operator work separately and perform FFT of the wavefunction before each operation with the kinetic term.

$$\psi(t + \Delta t, \mathbf{x}) = \hat{F}^{-1} \left[ e^{-i\hat{T}\Delta t/2} \hat{F} \left[ e^{-i\hat{V}(t)\Delta t} \hat{F}^{-1} \left[ e^{-i\hat{T}\Delta t/2} \hat{F} \psi(t, \mathbf{x}) \right] \right] \right] \quad (4.18)$$

The main advantage of the split-operator technique is that, in momentum space, the kinetic part of the evolution operator is diagonal. Thus, having performed the FFT the operator is directly computed as  $\exp(-i\hat{T}\Delta t/2) \tilde{\psi}(k_n)$ . The method of computing FFT is well known and grows quasilinearly  $\mathcal{O}(N \log N)$ . In 1D, the propagation of the potential operator is diagonal in position space so the operation is linear in  $N$ . In 3D, this step often imply a matrix - vector multiplication,  $\mathcal{O}(N^2)$ , and thus becomes the most time-consuming.

## 4.4 Split-operator operator Fourier method in spherical coordinates

A split-step method in spherical coordinates for central symmetric problems was developed by Herrmann and Fleck [42] and extended to general 3D problems in [43]. The idea is to expand the

wavefunction in radial grid functions augmented by spherical harmonics and take the advantage of the spherical Hamiltonian for the reduced wavefunction

$$\hat{H} = \left[ \frac{1}{2} \frac{\partial^2}{\partial r^2} + \frac{\hat{L}^2}{2r^2} + \underbrace{V(r) + E(t) \cdot \mathbf{r}}_{\tilde{V}(r, \Omega, t)} \right] \quad (4.19)$$

where  $\hat{L}$  is the angular momentum operator,  $V(r)$  is a spherical symmetric potential and  $E(t)$  is a time-dependent external field.

The grid expansion of the reduced function then reads, with  $m_l$  conserved for z-polarised pulses,

$$\psi(r, \Omega, t) = \sum_{l=0}^{l_{max}} f_l^{m_l}(r, t) Y_l^{m_l}(\Omega) \quad (4.20)$$

The split step scheme takes the form

$$\psi(r, \Omega, t_{n+1}) = \hat{F}^{-1} \left[ e^{-i \frac{\partial^2}{\partial r^2} \frac{\Delta t}{4}} \hat{F} e^{-i \tilde{V}(r, \Omega, t) \Delta t} e^{-i \frac{\partial^2}{\partial r^2} \frac{\Delta t}{4}} \hat{F}^{-1} \left[ e^{i \frac{\partial^2}{\partial r^2} \frac{\Delta t}{4}} \hat{F} \psi(r, \Omega, t_n) \right] \right] \quad (4.21)$$

The FFT step now acts only on the basis in momentum space as in 1D. After transforming back to r-space the second operator applies,

$$e^{\frac{-i \hat{L}^2}{2r^2} \Delta t} \sum_{l=0}^{l_{max}} f_l^{m_l}(r_i) Y_l^{m_l}(\Omega_j) \longrightarrow \sum_{l=0}^{l_{max}} f_l^{m_l}(r_i) e^{\frac{-i \Delta t l(l+1)}{2r^2}} Y_l^{m_l}(\Omega_j) \quad (4.22)$$

and from this expression the full wavefunction  $\psi(r_i, \Omega_j, t_k)$  is constructed on a grid. Then, any spatial dependent potential may be multiplied directly,

$$e^{-i \tilde{V}(r_i, \Omega_j, t) \Delta t} \psi(r_i, \Omega_j, t) \longrightarrow \psi(r_i, \Omega_j, t + \Delta t) \quad (4.23)$$

From this new wavefunction we can obtain the iterated radial basis functions by projection,

$$f_l(r_i, t + \Delta t) = \int d\Omega Y_l^{*m_l}(\Omega) \psi(r_i, \Omega, t + \Delta t) \quad (4.24)$$

The projection is accurately performed with Gauss-Legendre sum of  $l_{max}$  points. Now, the final FFT transformation and kinetic evolution operator is carried out on these iterated basis functions and one step has been completed.

## 4.5 Split-operator operator Fourier method in cylindrical coordinates

The set of cylinder coordinates is far from an obvious choice for Coulomb problems alone, since this set of coordinates does not offer separability and analytical basis states. However, for cases where a linear z-polarised field drives the dynamics essentially along this axis, this set of coordinates can be effective. As another advantage, it offers the possibility to switch between length and velocity gauge with minimum amount of programming work. A complication is the need to transform initial and final states to and from cylindrical coordinates before and after computations. The method to be presented was formulated by Chelkowski et. al [44]. We here

follow their description and additionally show how it can be formulated in both gauges. The implementation of this work was performed towards the end of the PhD project, so it has not yet been directly applied in calculations leading to new scientific results. However, the present section ends with first 3D results of the 1D calculations published in paper III.

In cylindrical coordinates  $(z, \rho, \phi)$  the Coulombic potential for hydrogen is given as

$$V(\rho, z) = -\frac{1}{\sqrt{\rho^2 + z^2}} \quad (4.25)$$

The Laplacian operator contains the partial derivation of both,  $\rho$  and  $z$  coordinates and the TDSE takes the form

$$\left[ -\frac{1}{2} \frac{\partial^2}{\partial z^2} + D_\rho + V(\rho, z) + zE(t) - i \frac{\partial}{\partial t} \right] \psi(z, \rho, t) = 0 \quad (4.26)$$

where the interaction term is written in the length gauge and the term with  $D_\rho$  is the part of the kinetic operator in the  $\rho$  coordinate,

$$D_\rho = -\frac{1}{2} \frac{\partial^2}{\partial \rho^2} - \frac{1}{2\rho} \frac{\partial}{\partial \rho} \quad (4.27)$$

The starting point is an expansion in basis functions related to the  $D_\rho$  operator,

$$v_n(\rho) = \frac{2^{1/2}}{L J_1(x_n)} J_0(x_n \rho / L) \quad (4.28)$$

where  $J_0$  and  $J_1$  are Bessel functions,  $x_n$  are zero points of  $J_0$  and  $L$  is the size of the box in the  $\rho$ -direction. The basis has the property,

$$D_\rho v_\rho = (x_n/L)^2 v_n(\rho) \quad (4.29)$$

and form an orthonormal set of states. Performing the expansion

$$\psi(z, \rho, t) = \sum_{n=0}^N f_n(z, t) v_n(\rho) \quad (4.30)$$

and projecting out on each basis state result in a coupled set of differential equations (in time and  $z$ ),

$$i \frac{\partial f_n(z, t)}{\partial t} = \left[ -\frac{1}{2} \frac{\partial^2}{\partial z^2} + V(z) + E(t)z \right] f_n(z, t) \quad (4.31)$$

where  $\mathbf{V}(z)$  is a square non-singular matrix with elements

$$V_{n,m}(z) = (x_n/L)^2 \delta_{n,m} + \int_0^L v_n V_c(\rho, z) v_m \rho d\rho \quad (4.32)$$

which has to be precalculated and stored. Note that this is a time independent operator so the calculation is only performed once. The split step procedure takes the form, with  $D_z = \partial^2/\partial z^2$ ,

$$\psi(z, \rho, t + \Delta t) = \hat{F}^{-1} e^{-iD_z \Delta t/4} \hat{F} \left[ e^{-iE(t)z \Delta t/2} e^{-iV(z) \Delta t/2} \hat{F}^{-1} \left[ e^{-iD_z \Delta t/4} \hat{F} \phi(z, \rho, t) \right] \right] \quad (4.33)$$

The coupling between different  $f_n$  functions takes place in the second operator. Note that it only requires a matrix-vector operation of an  $(N, N)$  sized matrix and a vector of length  $N$ . This is a

large advantage as compared to the spherical scheme. In velocity gauge we simply put the field interaction into momentum space and obtain, with  $p_z = -iS\partial/\partial z$ ,

$$\psi(z, \rho, t + \Delta t) = \hat{F}^{-1} e^{-iD_z \Delta t/4} e^{-iA(t)p_z \Delta t/2} \hat{F} \left[ e^{-iV(z)\Delta t/2} \hat{F}^{-1} \left[ e^{-iA(t)p_z \Delta t/2} e^{-iD_z \Delta t/4} \hat{F} \phi(z, \rho, t) \right] \right] \quad (4.34)$$

We have applied this method to reconsider the possibility to translate wavefunctions in single cycle pulses, cf. Paper III. In the figure below we reproduce initial and final states for the two cases of Fig. 4 in that paper. Indeed the wavefunction is seen to be translated without distortion for initial 10s, while the 1s state is "destroyed". It is also noteworthy to observe how similar in shape the distorted final 1s state in 3D compares with the 1D result.

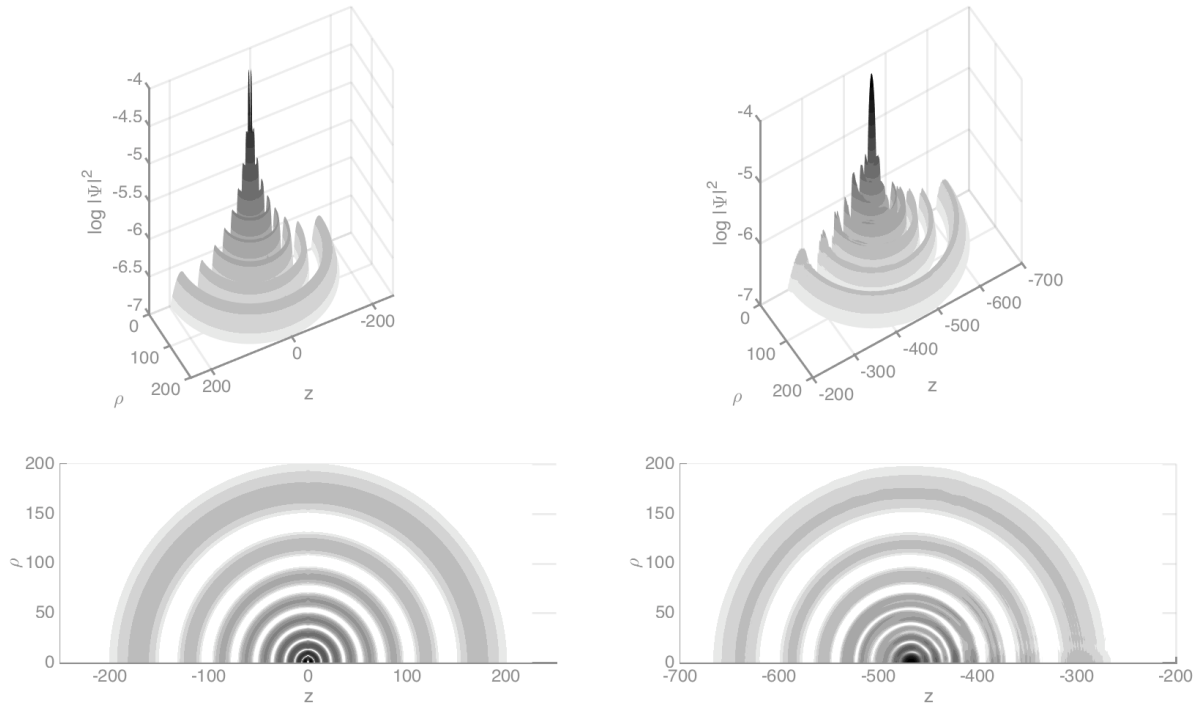


**Figure 4.1:** Probability density of the initial state (left) and the state after time propagation (right), plotted on logarithmic scale. The full scale is 3 decades, grey color scale with five shades per decade. The upper version are 3D surface plots in the  $\rho$ - $z$  plane, the lower is a plane projection. The pulse is coming from the right in the upper part. (This picture was provided by prof. L. Kocbach, IFT, UiB).

## 4.6 Propagation of Classical Dynamics

In propagating the classical dynamics we have applied both high order and low order numerical schemes. The lowest order schemes can be directly implemented with small time steps. The first order derivative for the position updates to

$$r(t_{i+1}) - r(t_i) = \int_{t_i}^{t_{i+1}} \mathbf{v}(t') dt' \approx v(t_i) \Delta t \quad (4.35)$$

The Euler's method is computed with linearly distributed time steps over all intervals and estimated error is roughly the size of the time step interval  $\Delta t$ . We can include the second order

derivatives in Taylor's expansion of a searched function, which gives a smaller error of the order  $\Delta t^2$ , if  $\Delta t \ll 1$ . The velocity may be updated at intermediate half time steps,

$$v(t_{i+1/2}) = v(t_{i-1/2}) + \frac{F(t_i)}{\mu} \Delta t \quad (4.36)$$

This substitution leads to the three-step Euler method also called the midpoint method. The midpoint method gives better approximation of solution with the complexity  $\mathcal{O}(\Delta t^3)$ . Another method for integrating differential equations is Verlet's algorithm developed by Loup Verlet in the 1960s [45]. We start with the Newton's equation of motion for electron

$$\frac{d^2 \mathbf{r}}{dt^2} = \frac{\mathbf{F}}{\mu} \quad (4.37)$$

which we can replace by the three-point formula 4.36 of second order derivative

$$\left. \frac{d^2 \mathbf{r}}{dt^2} \right|_{t=t_i} = \frac{1}{\Delta t^2} (r_{k+1} - 2r_k + r_{k-1}) \quad (4.38)$$

Putting above equations together we get

$$r_{k+1} = 2r_k - r_{k-1} + \Delta t^2 F_k \quad (4.39)$$

In practice we know initial position  $r_0$  and velocity  $v_0$ , so the first step is to find  $r_1$  to start the recursion.

$$r_1 \simeq r_0 + \Delta t v_0 + \frac{\Delta t^2}{2} F_0 \quad (4.40)$$

where the force is calculated as  $\mathbf{F} = -\nabla V(\mathbf{r}) - E(\mathbf{r})$ . Since Verlet's integration technique use several past steps to estimate a current value, it is a sort of the multi-step method. Verlet's algorithm, as well as Newton's equations, is numerically stable and reversible in time.

Runge-Kutta's solvers (RK) use only one previous step to calculate the current value of a searched function. Furthermore the time interval is non-uniformly divided into smaller parts, according to the order of RK, to minimize the approximation error. As the time step are divided by halving the original time interval, a slope of a searched function are divided into nodes with different weights in each node to better approximate it. Coefficients for nodes are documented in a relevant literature [46]. Let us assign time-step as  $h = \Delta t$ , RK of the 4-th order (RK4) estimates solution in radial coordinate as

$$v(h+1) = r(h) + \frac{h}{6} (k_1, 2k_2, 2k_3, k_4) \quad (4.41)$$

with slopes in each node  $k_1 - k_4$  given as

$$\begin{aligned} k_1 &= v(r(h), h) \\ k_2 &= v(r(h) + \frac{h}{2} k_1, h + h/2) \\ k_3 &= v(r(h) + \frac{h}{2} k_2, h + h/2) \\ k_4 &= v(r(h) + h k_3, h) \end{aligned} \quad (4.42)$$

The low order methods was applied for test calculations of 1D CTMC. The simple programming makes it possible to take advantage of the spike in the potential at  $r = 0$ , cf. paper I. In 3D we

have applied the Runge-Kutta-Fehlberg of 4/order 5 embedded pair method (RK45) [46]. The error estimation is most often estimated by running the ODE solver of higher order in parallel with the lower order of RK. For RK45, the solution of the 4th-order is compared with the 5th order solution. By subtracting these two solutions at each time step, one can get a local truncation error estimation  $e(i)$ . Advanced implicit methods as RK45 check the step size based on the truncation error during the propagation in order to get converged results.



# Chapter 5

## Scope of the work

Electromagnetic pulses can be produced with a broad range of frequencies, intensities and pulse lengths. The strongest pulses produced so far have intensities many orders of magnitude above the intensity defined by the field strength of the ground state hydrogen atom <sup>1</sup>,  $\sim 10^{21}$  W/cm<sup>2</sup> in Rutherford Appleton Laboratory [47]

. The shortest pulse lengths are attosecond pulses, high frequency pulses of duration 43 attoseconds [48]. The "standard" laser pulses of strong field physics are 400-1600 nm wavelengths reaching peak intensities around  $10^{14}$  W/cm<sup>2</sup> and having a pulse length of the order 10 fs. Such pulses contains a number, typical 2-10 optical cycles. This implies that for linear polarized fields the atom is exposed to a time dependent oscillating field with a corresponding lowering of the potential barrier, cf. Fig. 5.1.

Several competing processes can lead to ionization. First of all the electron may instantaneously or sequentially absorb a number of photons which cause multiphoton ionization. With a central pulse frequency  $\omega_0$ , a binding energy  $\varepsilon_0$  the electron will appear in the continuum with the energy  $\varepsilon = N\omega_0 - \varepsilon_0$ , illustrated as process III in Fig. 5.1. Another process is tunneling ionization. Here the electron tunnel through the barrier and propagate in the continuum as illustrated by process II. As the field changes direction the electron may be accelerated back towards the nucleus, collide with the remaining part of the wavefunction and ionize. Alternatively it may be recaptured by the nucleus and release a high frequency photon containing the energy gained in the continuum. This is the origin of High Harmonic Generation. Finally it may happen that the electron after tunneling populate a combination of states, which ionize directly without recombination. For tunnelling ionization to be effective the frequency needs to be small, in contrast to multiphoton ionization which is most effective for high frequency photons. The process was first analyzed by Keldysh in 1965 [49]. He introduced a parameter  $\gamma_k$  which classify the dominant ionization mechanism

$$\gamma_k = \sqrt{\frac{I_p}{2U_p}} = \sqrt{\frac{2I_p\omega^2}{E_0^2}}, \quad (5.1)$$

where  $I_p$  is the atom ionization energy,  $U_p = E_0^2/(4\omega^2)$  is the ponderomotive energy of the electromagnetic field with amplitude  $E_0$  and frequency  $\omega$ . It is the energy gained by an free electron in a harmonically oscillating field. As we consider the field strength of  $10^{-4} - 10^{-5}$  a.u. and  $\omega = 2.3510^{-5}$  a.u., in our case  $\gamma_k \ll 1$ . Tunneling ionization generally dominates over multiphoton ionization when  $\gamma \ll 1$ . A final process, marked as II in Fig. 5.1 is "over the

---

<sup>1</sup>E =  $5.1 \times 10^9$  V/cm at  $r = a_0$ .

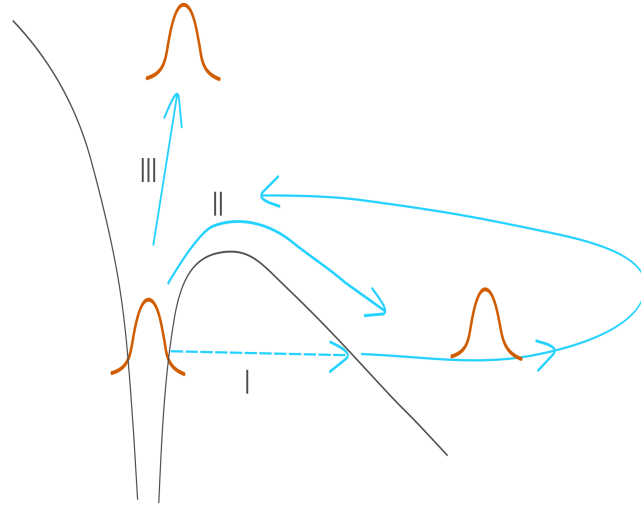


**Figure 5.1:** Processes in strong field ionization. I. Tunneling ionization with possible driving of electron back to the nucleus. II. Over the barrier ionization and III. Multiphoton ionization

barrier” ionization. It follows as a natural extension of tunneling, which is ‘under the barrier’ ionization, for sufficiently strong fields. At that point, the barrier has been lowered below the energy level of the particle in question and it may be directly accelerated along the negative field direction. For a slowly increasing field strength, the ionization process may well first start out as process I and terminate as process II.

Ionization by strong single cycle pulses needs some modifications of the standard process map above. Indeed, all three processes may take place. However, the single cycle nature of the mechanism may prohibit the recollision process. First of all, an initially free electron at the rest will first be accelerated opposite the field direction and then deaccelerated and brought to the rest a final distance given by the displacement parameter  $\alpha(T)$ , cf. Chapter 2. The reason is caused by the fact that laser pulses carries zero DC component,  $\int E(t)dt = 0$ , when integration is taken over the entire pulse. Unlike multicycle pulses single cycle pulses imply a nonzero displacement,  $\int A(t)dt \neq 0$ . This imply that the electron tends to be translated by the pulse. Consider for example the pulse shape 2.41. If the electron is ionized in the first half cycle the field will accelerate the particle in the negative  $z$ -direction until the electric field has turned and accelerate the particle back towards the nucleus and a recollision modified ionization process may occur. On the other side, the first cycle may simply be too weak to cause any significant ionization. The particle remains bound and dressed by the field until the strongest field strengths occur. The electron may here be released and directly accelerated towards positive  $z$ -direction. If both processes occur simultaneously, the two processes interfere and the final result needs a careful quantum mechanical treatment.

In the following we will discuss scaling phenomena in the ionization process.

A scaling law is here defined in the following way: Consider a process  $P = P(x, y)$  which depends on two parameters  $x, y$ . The process displays a surface in terms of  $x$  and  $y$ , but may also be represented as a number of curves for certain values of  $y = y_n$ .  $P(x) = P(x; y_n)$ . The scaling hypothesis predicts that all curves of this family will collapse onto a single curve provided we consider a scaled  $P$  as a function of a scaled  $x$ . This means a  $P$  divided by some functional relation of  $x, y_n$  and a scaled  $x$  as function of  $y_n$ . In the present work we consider only scaling of the independent variable  $x$ , where  $x$  is pulse strength or momentum.

In 2014 Li and Jones reported single cycle ionization by excited Na(*n*,*d*) atoms in THz fields up to 400 kV/cm pulse strengths [26]. They found a surprising  $n^{-3}$  scaling law for the total ionization probability and reproduced the scaling behaviour by CTMC calculations. Thus, plotting the ionization probability against a scaled pulse strength it appears as a universal curve. The surprise comes from the fact that CTMC calculations starting from a bound-state distribution necessary takes place through over-the-barrier processes which would be expected to scale as  $n^{-4}$ . In Paper 1 we set out to try to model the process quantum mechanically. A 1D model was chosen to cope with the extremely long integration times of a THz pulse. The results of this model gave an approximate  $n^{-3}$  power law dependence. Considering the range pulse strength region where the ionization probability switches from zero to unity and comparing this with the height of the potential barrier we concluded that the dominant mechanism could be ascribed to tunneling. However, the conclusion limited itself to 1D calculations, where the ionization probability as the function of pulse strength itself did not match the experiment very well: Our computed ionization probabilities were rising much more rapidly than the experiments.

This motivated studies of the very same process in 3D. We performed length-gauge calculations based on the split step method described in Chapter 2. Here we could compare our results with calculations performed, mainly at shorter pulse lengths [51, 52]. This group also obtained an almost magical agreement between CTMC and TDSE calculations. Our TDSE calculations agreed very well with their for initial  $n = 15, d$  states of hydrogen. We then extended their calculations towards the experimental pulse lengths and computed ionization probabilities both with the CTMC and the TDSE methods.

Our results can be summarized as follow:

- The quantum mechanical ionization probabilities fall on a universal curve for a mixed scaling parameter containing elements of  $n^3$  and  $n^4$ .

$$E_0^{sf}(n) = \alpha n^{-4} + (1 - \alpha)n^{-3} \quad (5.2)$$

In addition the much steeper response to the pulse strength than observed in experiments remains. Applying this scaling function to the emitted electron momenta of ionized electrons we find that all initial states gives characteristic scaled electron momenta.

- The CTMC calculations does not follow the same scaling law, and in the long pulse limit there are significant differences between the final state momentum distributions between the two methods.
- Coulomb phases are important to compute the differential cross section, in particular the low energy tail. Electrons which appear to be propagating in the positive *z*-direction are affected by the Coulomb phases and appear on the negative side, cf. Fig 7 of Paper II. A detailed derivation of the differential cross section based on the output of the applied grid method is given in Appendix 2 [7.3].

Several factors may explain the differences between experiment and theory: Our representation of the experimental pulse shapes, and the experimental pulse shape in itself, may not be accurately enough. There may be other experimental factors as well as limits and errors occurring in the numerical results. Therefore we have reported all details of our approach with the hope that future approaches and new experiments can create a complete understanding of this issue.

The final paper III of this work was initiated by the research process of testing the spherical code. By accident we discovered that a strong, short single cycle pulse could remove the entire wavefunction from the atom. It turned out that this discovery had been done about 13 years ago by Dimitrovsky and coworkers, cf. [50]. We were however able to extend their analysis and point out a few new results:

- The wavefunction is translated completely along the displacement vector.
- Excited atoms are translated almost without dispersion, implying that the removal of the nucleus can offer direct imaging of doubly excited states and dynamical features.

A natural extension of this work would be to confirm the 1D results here obtained with full 3D calculations. In the final stage of the PhD work we developed a split-step method in cylindrical coordinates for this purpose. Test calculations with the same pulses as in paper III agree completely with the main conclusions from 1D, cf. the previous chapter.

# Chapter 6

## Conclusion and outlook

In the present thesis we have studied aspects of one-electron dynamics in atoms exposed to a single cycle electromagnetic pulse. The work has implied theoretical analysis, programming, parallel computing on supercomputers and analysis. The focus have been to initially excited atoms and we have considered pulse lengths from significantly longer than the corresponding classical orbital time of the initial state in question to significantly shorter. The focus has been to explore the ionization dynamics in detail, the characteristics of the wavefunction after the pulse including the angular distribution of the emitted electrons. The results are in partial agreement with experiments and independent theoretical work. The agreement amounts to identical quantum mechanical computed results for ionization. Our CTMC results however, differ from the computed results of [51] and [52]. Neither did we obtain the same scaling law as obtained in the experimental work [26]. One origin of the disagreement may be a different selection procedure for initial states. Regarding experiments we find relatively similar response to the electric pulse with increasing strength. However, the response in our calculations are stronger, or more sensitive to increasing strength. A possible origin of this discrepancy may lie in the experimental knowledge of the pulse. Another origin may be that we use hydrogen d-states, while in experiment was measured with alkali Rydberg-atoms. Only new experiments in combination with independent calculations can settle this issue.

Following the introduction in Chapter 1, Chapter 2 describes the main features of non-relativistic quantum mechanics applied in this thesis. Chapter 3 correspondingly describes the CTMC method we applied. In Chapter 4 we have described numerical methods, which have been tested and applied at various stages in this work. Chapter 5 describes the scope of the scientific work and can be viewed as an introduction to the scientific results in the form of three published papers 7.

In highlighting the results, we mention that a 1D model grasps the main feature of the ionization dynamics. An extension of the work to 3D involved both a new implementation of the spherical split-step method, a new implementation of the split-step method based on cylindrical coordinates and use of a often applied CTMC method. Scaling laws for both quantum and CTMC calculations of ionization probability and momenta have been found in the long pulse limit. Angular distribution with quantum phases shows possible backward scattering in contrast to the scattering predicted directly from classical calculations. Regarding short intense pulses we showed that the dynamics of a wavefunction is fully described with the translation vector in Kramer-Henneberger frame: This imply that an intense field may “grab” the entire wavefunction and transfer it far away from its nucleus. We noted that this may be the origin of a potential new imaging technique.

In closing, we mention several routes of extensions of this work. First of all, the response of nano-structures to single cycle pulses is both interesting from a fundamental point and may lead to new technology. Fundamentally, the ionization dynamics of metallic states contains new aspects. From an applied point of view, scaling laws may be applied to characterize nano-tip fabrications [53]. For atoms, it would be interesting to consider scattering from a series of  $l$  states and to investigate the sensitivity to quantum defects in alkali atoms. Exploring which pulse shapes which could actually reproduce the experiments in detail would be interesting as well. Finally, a more in-depth study of wavefunction translation would also be very interesting. One may speculate that doubly excited atoms or dynamical processes inside single electron atoms may be explored by wave function translatative pulses in combination with recording the translated electron spectrum of the atom without nucleus.

# Bibliography

- [1] J. J. Thomson, Philos. Mag. **44**, 293 (1897). 9
- [2] J. J. Thomson Philos. Mag. **40**, 512 (1895). 9
- [3] E. Rutherford, Philos. Mag. **21**, 669 (1911). 9
- [4] M. Planck, Ann. Phys. **309**, 553 (1901). 9
- [5] A. Einstein, Ann. Phys. **17**, 132 (1905). 9
- [6] N. Bohr, Philos. Mag. **26**(6), 1-25 (1913). 9
- [7] L - V. de Broglie, *Recherches sur la Theorie des Quanta*, Ann. de Phys. 10<sup>e</sup> serie, t.III (1925). Translated by A.F. Kracklauer, AFK (2004). 9
- [8] C. Davisson and L. H. Germer, Phys. Rev. **30**, 705 (1927). 10
- [9] G. P. Thompson, A. Reid, Nature **119**, 890 (1927). 10
- [10] P.G. Merli, G.F. Missiroli, G. Pozzi, Am. J. Phys. **44**, 306 (1976). 10
- [11] E. Schrödinger, Ann. Physik, **79**, 745 (1926). 10, 12
- [12] M. Born, Die Naturwissenschaften **15**, 238 (1927). 10
- [13] M. Born, Nature **119**, 354 (1927). 10
- [14] K. von Klitzing, G. Ebert, N. Kleinmichel, H. Obloh, G. Dorda, and G. Weimann, Proc. ICPS **17**, Edited by J. D. Chadi and W. A. Harrison, (Springer, NY, 1985). 10
- [15] K. Varju, Y. Mairesse, B. Carre, M. Gaarde, P. Johnsson, S. Kazamias, P. Salieres, J. Mod. Opt. **52**, 379-394 (2005). 10
- [16] J. Mauritsson, M. Gaarde, K. J. Schafer, Phys. Rev. A **72**, 013401 (2005). 10
- [17] Ch. Brand et al., Nature Nanotechnology **10**, 845 (2015). 10
- [18] J. P. Cotter et al., Science Advances **3**, 12017 (2017). 10
- [19] I. Lekavicius, D. A. Golter, Thein Oo, Hailin Wang, Phys. Rev. Lett. **119**, 63601 (2017). 10
- [20] J. J. Donatelli, J. A. Sethian, P. H. Zwart, PNAS **114**, 7222 (2017). 10
- [21] M. V. Dutt, L. Childress, L. Jiang, E. Togan, J. Maze, F. Jelezko, A. S. Zibrov, P. R. Hemmer, M. D. Lukin, Science **316**, 1312 (2007). 10

## Bibliography

- [22] J.M. Hansteen, O.P. Mosebekk, Nuclear Physics A **201**(3), 541-560 (1973). 11
- [23] J. S. Briggs, J. M. Rost, EPJ D **10**, 311-318 (2000). 11
- [24] D. Griffiths, *Introduction to Electrodynamics* (Prentice Hall, 1999), ISBN 9780138053260. 11
- [25] D. J. Griffiths *Introduction to Quantum Mechanics (2nd ed.)*, 247, (Prentice Hall,2004), ISBN 0-13-111892-7.
- [26] S. Li, R. R. Jones, Phys. Rev. Lett. **112**, 143006 (2014). 17, 35, 37
- [27] T. Birkeland, M. Førre, J. P. Hansen and S Selstø, J. Phys. B: At. Mol. Opt. Phys. **37**, 4205-4219 (2004).
- [28] G. Lagmago Kamta, A. D. Bandrauk, Phys. Rev. A **71**, 053407 (2005). 17
- [29] N. Metropolis, S. Ulam. J. of the Am. stat. assoc. **44**(247), 335-341 (1949). 19
- [30] J. von Neumann, *Monte Carlo Method* **12**, 36-38, Ed. by A.S. Householder, G.E. Forsythe, and H.H. Germond,(Washington, D.C.: U.S. Government Printing Office, 1951). 19
- [31] R. A. Abrines, I. C. Percival, Phys. Lett. **13**(3), 216-217 (1964).  
R. A. Abrines, I. C. Percival. Proc. Phys. Soc. **88**(4), 861-873 (1966). 19
- [32] I. C. Percival, D. Richards, Adv. At. Mol. Phys. **11** (1975). 19
- [33] C. O. Reinhold and C. A. Falcón. Phys. Rev. A, **33**(6), 3859-3866 (1986). 19
- [34] H. Agueny, M. Chovancová, J. P. Hansen, L. Kocbach, J. Phys. B At. Mol. Opt. Phys. **49**, 245002 (2016). 22
- [35] X. Y. Lai, C. Qing-Yu and M. S. Zhan, New J. Phys. **11**, 113035 (2009). 19
- [36] Z. Ruan, R. G. Zeng, Y. Ming, M. Zhang, B. Da, S. F. Maod, Z. J. Ding\*a, Phys. Chem. Chem. Phys. **17**, 17628-17637 (2015). 19
- [37] E. J. Kirkland. *Advanced Computing in Electron Microscopy*, (Plenum, New York, 1998). 19
- [38] R. P. Feynman, Rev. Mod. Phys. **20**, 367 (1948). 19
- [39] Min Li, Ji-Wei Geng, H. Liu, Y. Deng, Chengyin Wu, Liang-You Peng, Qihuang Gong, and Yunquan Liu, Phys. Rev. Lett. **112**, 113002 (2014).
- [40] C. Leforestier et al., J. Comput. Phys. **94**, 59 (1991). 26
- [41] J. Cranck and J. Nicholson, Mathematical Proceedings of Cambridge Philosophical Society **43**, 50-67 (1947). 26
- [42] Mark R. Hermann and J. A. Fleck, Jr., Phys. Rev. A **38**, 6000 (1988). 27
- [43] J. P. Hansen, T. Sørøvik, and L. B. Madsen Phys. Rev. A **68**, 031401(R) (2003). 27
- [44] S. Chelkowski, T. Zuo, A. Bandrauk, Phys.RevA **46**(9) (2002). 28



- [45] L. Verlet, Phys. Rev **159**, 98 (1967). 31
- [46] T. Sauer, *Numerical analysis, 2nd edition*, (Pearson Education Limited, 2013). 31, 32
- [47] C. Hernandez-Gomez et al, J. Phys.: Conf. Ser. **244**, 032006 (2010). 33
- [48] Gaumnitz T, Jain A, Pertot Y, Huppert M, Jordan I, Ardana-Lamas F, Wörner HJ. Optics Express **25**(22), 27506-27518 (2017). 33
- [49] V. Keldysh, Sov. Phys. JETP **20**, 1307 (1965). 33
- [50] D. Dimitrovski, E. A. Solov'ev and J S Briggs, Phys. Rev. Lett. **93**, 083003 (2004). 36
- [51] B. C. Yang and F. Robicheaux, Phys. Rev. A **90**,063413 (2014). 35, 37
- [52] B. C. Yang and F. Robicheaux, Phys. Rev. A **91**, 043407 (2015). 35, 37
- [53] L. Wimmer, G. Herink, D. R. Solli, S. V. Yalunin, K. E. Erchternkamp and C. Ropers, Nat. Phys. **10**, 432-436 (2014). 38
- [54] J. P. Hansen, J. Lu, L. B. Madsen, and H. M. Nilsen, Phys. Rev. A **64**, 033418 (2001). 87



## **Chapter 7**

### **Scientific Results**



## List of Papers

---

- I) H Agueny, M Chovancova, J P Hansen and L Kocbach. **Scaling properties of field ionization of Rydberg atoms in single-cycle THz pulses: 1D considerations.** J. Phys. B: At. Mol. Opt. Phys. 49 (2016), 245002 (7pp).
  
- II) M. Chovancova,<sup>1</sup> H. Agueny,<sup>1</sup> J. J. Rørstad,<sup>2</sup> and J. P. Hansen. **Classical and quantum mechanical scaling of ionization from excited hydrogen atoms in single-cycle THz pulses.** Phys. Rev, A 96 (2017), 023423 (10pp).
  
- III) M Chovancova, H Agueny, M Førre, L Kocbach and J P Hansen. **Spatial transport of electron quantum states with strong attosecond pulses.** J. Opt. 19 (2017), 114008 (6pp).

The scientific work displayed in this thesis has been group teamwork all the way. While problem formulation mainly was provided by my supervisor I took part in discussions, programming, analysis and writing



## **PAPER I**





# Scaling properties of field ionization of Rydberg atoms in single-cycle THz pulses: 1D considerations

H Agueny, M Chovancova, J P Hansen and L Kocbach

Department of Physics and Technology, Allegt. 55, University of Bergen, NO-5007 Bergen, Norway

E-mail: [jan.hansen@uib.no](mailto:jan.hansen@uib.no)

Received 27 September 2016, revised 4 November 2016

Accepted for publication 9 November 2016

Published 25 November 2016



## Abstract

In recent experiments of single-cycle field ionization of excited  $\text{Na}(nd)$  atoms with principal quantum number  $n \in [6, 15]$  (Li and Jones 2014 *Phys. Rev. Lett.* **112** 143006) it was shown that the maximum field intensity necessary to ionize 10% of the atoms decreases with increasing  $n$  according to an  $n^{-3}$  power law dependence. This scaling property at the same ionization probability was confirmed in classical trajectory Monte Carlo calculations. In this work we note that the scaling relation in the experiment is much more general, it is in fact valid for all ionization probabilities. When applied to the emitted electron energies it places a very wide distribution of electron momenta from different initial states onto a narrow range. These aspects are investigated in a one-dimensional model with a 3D hydrogen-like spectrum. Calculations confirm the general  $n^{-3}$  scaling relation for the ionization probability and that this particular scaling of the kinetic emission spectrum puts the ejected electron momenta on a narrow common scale. The ionization mechanism itself is identified as quantum mechanical tunneling and the nature of the tunneling process is the direct origin of the scaling law.

Keywords: scaling law, Rydberg atoms in THz pulses, electron emission process

(Some figures may appear in colour only in the online journal)

## 1. Introduction

Ionization of bound electrons by strong laser pulses occurs most frequently as multiphoton ionization or tunneling. In the recent development of single cycle THz pulses, a new mechanism, *displacement ionization* has been introduced [1]: in this case the electron is ionized at a specified time and pulse strength and is displaced in one direction opposite to the field. It follows that during the pulse, the ionized electron never recombines with the parent nucleus. If the particular ionization mechanism follows the classical over the barrier process, the field strength required to allow the electron to pass the barrier is related to the principal initial quantum number as  $n^{-4}$ . In this case the ionization probabilities from various initial excited states as a function of peak electric field will scale with the same power law. However, experiments performed with different characteristics (intensity, frequency, pulse length) have previously displayed a variety of different

power law scaling dependencies, from  $n^{-2}$  [3] to  $n^{-5}$  [4], valid for a finite range of initial states with principal number  $n$ .

Recently Li and Jones [2] reported experiments of field ionization in the intermediate  $n \in (6, 15)$ -regime where excited  $nd$  states of sodium have been exposed to a strong single-cycle pulse of duration 3–4 ps as compared to a  $\sim 0.5$  ps period of the classical  $n = 15$  state. Here it was found that the field intensity at 10% ionization probability exhibits a  $n^{-3}$  dependence with increasing initial  $n$ -level of the target atoms. The scaling law was confirmed in classical trajectory Monte Carlo calculations (CTMC). It was concluded that the ‘adiabatic over-the-barrier ionization is suppressed due to the extended times required for high- $n$  electrons to leave the binding potential’ is responsible for a novel  $n^{-3}$  scaling. Further more, the experiments displayed that the released electron momenta increase strongly with decreasing initial  $n$  level, a seemingly counterintuitive phenomenon of what is expected in the multi-photon regime: the experiment showed

that the kinetic energy range of the emission spectra from the  $n = 6, 7$  levels are an order of magnitude larger in energy than the spectrum of the  $n = 15$  state.

The ionization mechanism was considered from a theoretical point by Yang and Robicheaux in [1, 5] based on 3D CTMC calculations and time dependent quantum treatments of the problem. The latter is particular challenging when considering differential cross section in electron momentum or emission angle, since the electron displacement during the pulse can extend up to  $10^5$  a.u. in combination with a pulse duration of the magnitude of the order  $10^5$  a.u. as well. Thus, numerical grid sizes in space and time are both an order of  $10^2$  larger than what is needed in the strong field regime of ionization of ground state atoms. Their analysis, based on calculations with pulse duration below and up towards the orbital period  $T_n = 2\pi n^3$  is here summarized in the following main points: The  $n^{-3}$  scaling at 10% ionization probability is only valid only up to a threshold initial state,  $n \sim 20$ -level for a pulse duration of  $\sim 0.1$  ps. The threshold increases with increasing pulse length. Beyond the threshold a new  $n^2$  scaling sets in, which implies that increasingly stronger fields are necessary to ionize Rydberg atoms with increasing initial principal quantum number. The final ionized electron momenta are almost always directed along the positive direction of the electric field (the direction of the electric field in the first half cycle). Finally, for field durations  $T_{\text{field}} \sim T_n$  an oscillatory structure in the ionization probability appears as the field intensity increases towards 100% ionization probability. However, most of these calculations are performed for considerable shorter pulses than the experimental ones. And the obtained agreement between classical and quantal calculations in these works suggest that the considered ionization process is classical in nature.

The purpose of the present paper is to investigate closer, based on simulations, the nature of  $n^{-3}$ -scaling found in the experiment [2] and the ionization mechanism itself. For this purpose we will apply pulses of magnitude and duration very similar to the experiment and consider a quantum mechanical approach only. Due to the computational challenge in this parameter domain we restrict ourselves to a one-dimensional model (1D) approach. While the ability to generalize results of 1D models to 3D can always be questioned, we here note that 1D and full calculations of ionization of Rydberg states of nanotips gives almost identical results [6]. We first introduce the model and then discuss the electron dynamics in two regimes defined by the pulse shape and peak field. We will show that the observed scaling at 10% ionization probability is generally valid for any field strength which allows us to plot the ionization probabilities onto a universal curve. Further more we will identify the ionization mechanism itself in the 1D model as quantum tunneling.

Finally, we show that the ionization mechanism implies that ejected electron momenta originating from a fixed  $n$ -level increase proportional to the peak field strength at the onset of ionization. As a consequence, the large range of the observed ejected electron momenta in [2] is caused by the same mechanism responsible for the scaling law: when the momenta of the ejected electrons are modified by  $(n_{\text{max}}/n)^3$ ,

the kinetic emission spectra all appear in the same order of magnitude. In the next section the theoretical model is introduced followed by a section describing the results. Concluding remarks and outlook are given in the final section. Atomic units are applied unless otherwise explicitly mentioned.

## 2. Theoretical model

We consider a 1D model of a hydrogen-like atom, as is often done when computational complications seem to obscure the anticipated single mechanisms. In the present connection we can mention a recent paper [7] with an enhanced 1D Coulomb-based model. However, the 1D Coulomb problem is a non-trivial matter due to the stronger singularity in the single dimension (e.g. [8]). Therefore a so-called soft core model is necessary, i.e. where the  $|z|^{-1}$  is replaced by  $\sqrt{z^2 + a^2}^{-1}$ . In our study we have added more terms and adjusted the parameters of the potential to obtain somewhat realistic energies close to  $n^{-2}$  hydrogen pattern, as discussed below, where  $n$  is simply the number of the level and the levels are of even and odd parity, starting with even parity for  $n = 1$ .

An important feature of the Coulomb problem is the Stark effect, i.e. the splitting of the degeneracy of the hydrogen-like levels in three dimensions. Unfortunately, this effect can not be modeled in one dimension, since the degeneracy of levels is not present. It has in fact been shown [9] that for well behaved 1D problems there is no degeneracy possible.

One interesting observation we made in the early stages of this work is that it might be possible to develop 1D models by modifying the soft core Coulomb potential, which could come close to a near-degeneracy of the pairs of even and odd parity levels and thus model an analogue of the Stark effect in one dimension. For this we arrange the soft-core Coulomb levels in a pattern (1s, 2p, 2s, 3p, 3s, ...) in a very close analogy to the real 3D hydrogen-like pattern. With so defined 'radial'  $n$  the even parity ' $ns$ ' levels follow quite closely the  $n^{-2}$  hydrogen pattern, while the odd parity ' $np$ ' states with the same value of  $n$ , are somewhat displaced from the  $n^{-2}$  rule towards lower energies. This has also been shown for a closely related truncated Coulomb potential already in 1969 [8], where even explicit formulas for the energies have been derived.

We have then considered to construct a modified potential emulating the 'centrifugal barrier' and thus obtaining a spectrum with the pairs of the same  $n$  and opposite parity becoming nearly degenerate. One way would be to slightly decrease the binding, which would push the 'p'-states up and add a very narrow extra attractive potential which would not influence much the odd parity states but pull the even parity 's' states somewhat down. It turned in principle possible but this feature becomes too complicated. The fact is that in the 1D model finally adopted here with  $E_n \propto n^{-2}$ , where  $n$  is simply the number of the state, the precise analogue of the Stark mechanisms is not present. However, as the

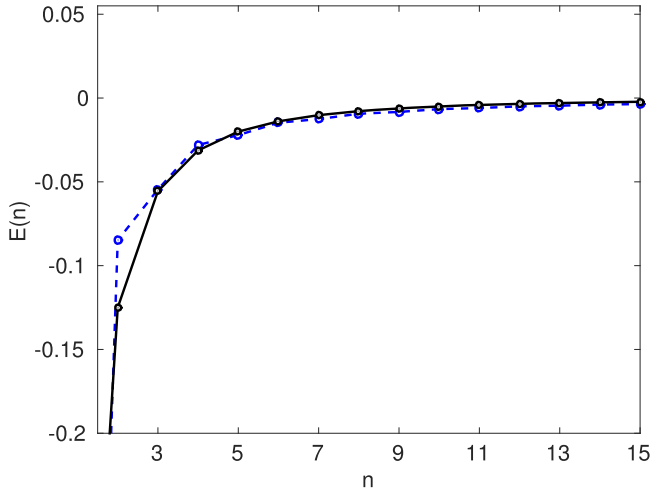


**Figure 1.** Energy levels of the present 1D (blue dashed line) potential compared with the  $n^{-2}$  energy levels of the hydrogen atom (black line).

results will show, the studied scaling can be understood without the Stark lifting of the initial degeneracy.

Within the semiclassical (strong field) approximation we solve the time-dependent Schrödinger equation

$$\left[ -\frac{1}{2} \frac{\partial^2}{\partial x^2} + V_b(x) - E(t)x - i \frac{\partial}{\partial t} \right] \psi(x, t) = 0 \quad (1)$$

for a 1D ‘hydrogen-like’ atom in a time dependent electric field  $E(t)$ . To obtain a hydrogen-like energy spectrum the binding potential  $V_b(x)$  have to have a finite negative cutoff value at  $x = 0$  and a faster increase towards zero than hydrogen-like 1D Coulomb potentials of the form  $V(x) \sim -1/\sqrt{x^2 + b}$ . In our approach we then let  $b \rightarrow b(x) = a_0 + b_0|x|^{c_0}$  with constant  $(a_0, b_0, c_0) = (0.1, 7.0, 1.75)$ .

Our restriction to the 1D model is due to the very long wavelength ( $\sim 0.3$  mm) and long total simulation time ( $\sim 5$  ps). It requires very large grids to perform the numerical calculations which follows the wavefunction of the electron without absorbing cutoff. We numerically solve equation (1) using a Fourier split-operator method [10]. Converged results are achieved at time steps  $\Delta t \sim 0.05$  a.u., whereas the spatial discretization  $\Delta x \sim 0.25$  a.u. allows a maximum momentum spectrum  $\Delta p \sim \pi/\Delta x \sim 12.5$  a.u. The number of grid points in the simulations then reach up to  $2^{21}$ . Calculations have been performed in length gauge and in velocity gauge and found to be identical.

We illustrate in figure 1 energy levels obtained by diagonalizing the Hamiltonian using the above binding potential. The diagonalization has been performed based on infinite well basis functions. The obtained energies are plotted together with the exact energies of the hydrogen-like atom levels. A reasonable agreement is obtained for the spectrum with state numbers  $n > 4$ . The spatial extension of the states as compared to the radial hydrogenic distributions are in general quite different. The classical turning point for the hydrogen atom, and for a given energy level  $n$  is  $\propto 2n^2$ . Consequently, the product  $E_n \cdot r_n = -1$  ( $\forall n$ ). In table 1 we

**Table 1.** State numbers, energies, turning points and product of energy and turning point in a 1D model.

$n$	$E_n$	$x_{\text{turn}}$	$E_n \cdot x_{\text{turn}}$
1	-0.7268328	0.43131	-0.31349
2	-0.0731053	5.82841	-0.42609
3	-0.0465510	9.63146	-0.44835
4	-0.0230487	20.99522	-0.48391
5	-0.0180695	27.47359	-0.49644
6	-0.0117304	44.23278	-0.51887
7	-0.0099257	53.15432	-0.52760
8	-0.0072559	74.97640	-0.54402
9	-0.0063881	86.20811	-0.55071
12	-0.0036767	157.67497	-0.57973
15	-0.0026322	226.89197	-0.59723

observe that this product is smaller in the 1D model. However, for increasing  $n$  the discrepancy with the hydrogenic result decreases.

In the experiment [2], a single cycle THz pulse was applied which has a positive first half cycle followed by a  $\sim 1.5$  higher negative peak intensity in the second half cycle. Here we approximate this pulse by joining two sine functions,

$$E(t) = \begin{cases} -E_0 \sin(\omega t), & \text{if } -T < t < 0 \\ -E_0 \beta \sin(\beta \omega t), & \text{if } T/\beta > t > 0 \\ 0 & \text{otherwise} \end{cases} \quad (2)$$

with the value of the dimensional constant  $\beta \sim 1.5$ . Here,  $-T$  is the initial time of the pulse and  $T/\beta$  is the final time. A value of  $\beta = 1.5$  is chosen to obtain a pulse which is in reasonable agreement with the experimental one. In figure 2 we compare this choice with the experimental pulse shape (upper panel) at unit intensity and the corresponding vector potential (middle panel)  $A(t) = -\int_{-T}^t E(t') dt'$ . The results do not depend critically on  $\beta$ . The advantage in using this particular electric field is related to its simple and analytic form, in addition, it has a well defined exact integration range, as compared for example to the field parametrization in [5]. In the lower panel of figure 2, (thick lines) we show the displacement,  $\alpha(t) = \int_{-T}^t A(t') dt'$ ,

$$\alpha(t) = \begin{cases} \frac{E_0}{\omega} (t + T) - \frac{E_0}{\omega^2} \sin(\omega t), & \text{if } -T < t < 0 \\ -\frac{E_0}{\omega} (t + T) - \frac{E_0}{\beta \omega^2} \sin(\beta \omega t), & \text{if } T/\beta > t > 0 \end{cases} \quad (3)$$

which shows the position of a classical electron with time, starting from zero in absence of the binding potential. The non-zero displacement character of the field becomes clear: the effect of a full field cycle is to move an initially free particle to the left (in the negative  $x$ -direction). For the experimental region of parameters  $(E_0, \omega)$  this displacement may become of the order  $10^5$  and above.

It has already been pointed out that the experimental pulse leads to electron emission in one direction (final momenta  $> 0$ ) only: at the onset of ionization from a given initial state, ionization takes place only near the maximum

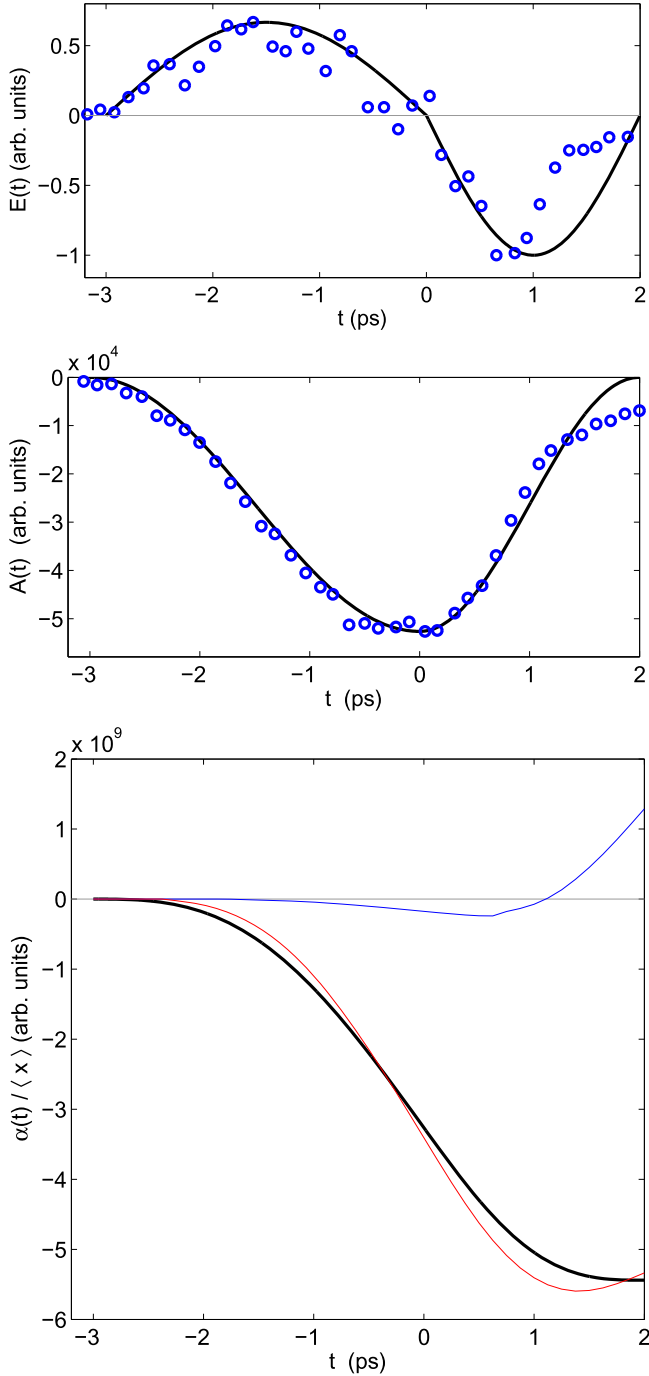


**Figure 2.** The two upper panels show a comparison between the time-variation of the electric field (experimental points are scaled to a maximum peak field  $E_0\beta = 1$ ) and the vector potential (see equation (2)) with experimental pulse data of [2]. The thick black line, in the lower panel, shows the corresponding displacement, see equation (3). The thin blue and red lines show the expectation value of the position of a quantum calculation by solving the TDSE for  $n = 15$  level scaled to unit electric field strength, for  $E_0 = 0.31 \times 10^{-5}$  and  $0.62 \times 10^{-5}$  a.u. respectively. In all plots the field frequency  $\omega = \pi/3$  THz.

(negative) field value. This corresponds to the second half cycle of the pulse when the field is negative. As a consequence the electron is accelerated in the positive direction (opposite of the field). At higher intensities, outside the range

of the experiment [2], or with higher initial  $n$  states, ionization occur in the first cycle of the field, which causes an initial acceleration of the electron in the negative direction. As the field turns, a deceleration will eventually lead to a final positive momentum equal to  $\int_{-T}^{t_{\text{ion}}} E(t') dt'$ , where  $t_{\text{ion}}$  is the time of ionization. For  $t_{\text{ion}} > -T$ , this momentum will always be positive implying that electrons are emitted in the positive direction only. This implies that the higher initial  $n$ , the lower characteristic momenta of the ionized electrons. The process may however be disturbed by electron-core scattering as the electron will pass the origin well after the THz pulse has vanished. The situation is completely identical for inverted pulses with  $\beta < 1$ , but with opposite ionization mechanism in terms of increasing field strength. For certain values of  $\beta \sim 1$ , we may even have partly ionization in both peak regions which create interesting well separated electron wave packets that can interfere and give rise to a strong modulation in the kinetic emission spectrum.

To illustrate the ionization mechanisms in the two regions, we show in the lower panel of figure 2 (thin blue line) the time-evolution of the expectation value of the position  $\langle x \rangle$  stemming from quantum calculation with initial  $n = 15$  level. Indeed, the expectation value shows a situation where ionization takes place exclusively in the second half cycle: the wavepacket has approximately zero expectation value until the electron is ionized along positive  $x$ -axis at the final stage of the pulse and the expectation value is seen to increase. This calculation is performed at a peak field strength around  $0.31 \times 10^{-5}$  a.u.. Doubling the pulse strength gives unit ionization probability in the first part of the pulse. The expectation value is then seen to develop towards negative values almost as a free particle. Eventually, in the final part of the pulse, the sign of the electron momentum can be seen to have change and the electron propagates to the right (towards the positive  $x$ -axis). A similar asymmetry in the backward/forward direction has previously been noted in a range of calculations with strong field pulses of 800 nm [11–14]. The discussion has elaborated on the sensitivity of the scattering asymmetry to the carrier envelope phase of the field. Recently, the role of spatial field dependence has been addressed as well [15]. A single cycle THz pulse here appears to be an ideal system to re-address this discussion, since the ionization dynamics is less complex and the pulse is well defined.

### 3. Results

In the present section, we address the scaling behavior of the ionization probability. In addition, we also address the possible scaling behavior of the the energy distribution of the ejected electrons. In the experiment [2], it was made a point that the field intensity necessary for  $\sim 10\%$  ionization probability falls on a straight line in a log plot and by that establishing a  $n^{-3}$  power law dependence. We first show in the top panel of figure 3. that this power law is quite generally valid for the hole region of the experiment. This can be seen



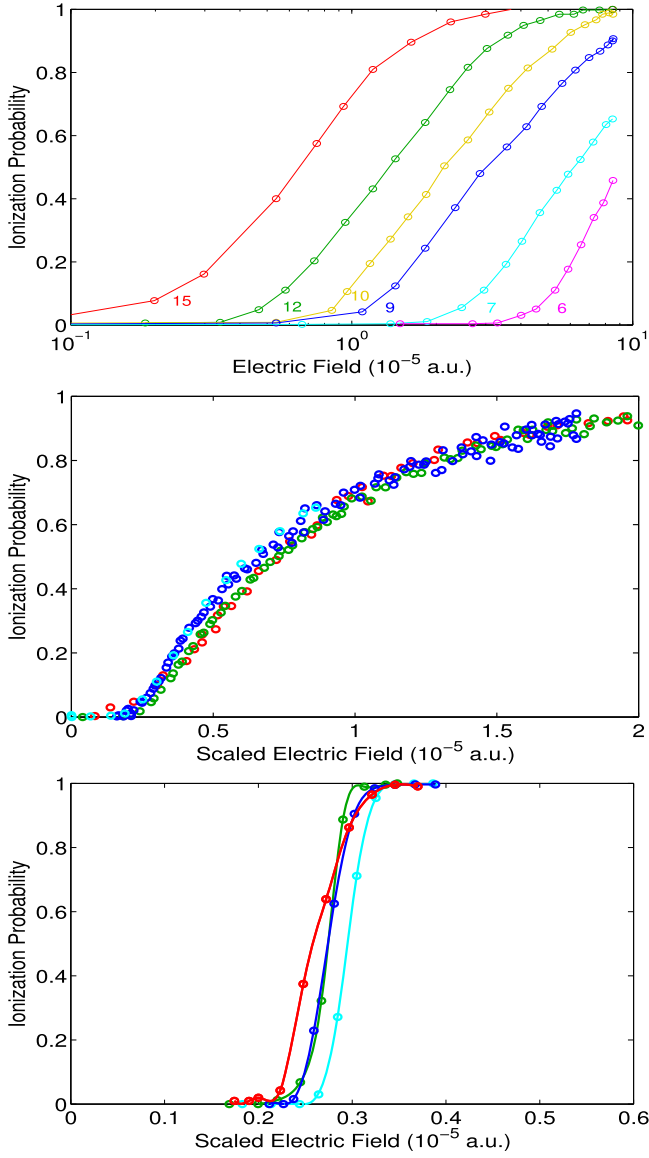


**Figure 3.** The top panel shows approximately digitized measured ionization probabilities from [2] plotted as function of peak electric field strengths on a semilogarithmic scale. Color coding:  $n = 6$  (magenta),  $n = 7$  (cyan),  $n = 9$  (blue),  $n = 10$  (yellow),  $n = 12$  (green),  $n = 15$  (red). The medium panel shows the same experimental points on a linear intensity axis scaled by  $[n/(n_{\max} = 15)]^3 E_0/\beta$ . The bottom panel shows the same scaled ionization probabilities from the TDSE for  $n = 7$ ,  $n = 9$ ,  $n = 12$  and  $n = 15$ .

from figure 3 which is based on approximately digitized data from [2]. In the upper panel, the ionization probabilities are plotted on a semilogarithmic scale. We observe that they form almost parallel which suggests that a universal curve can be constructed using multiplicative scaling of field strengths. When scaling the field strengths by  $(n/15)^3$  and plotting the initial state ionization probabilities in the middle panel of figure 3 we observe that indeed the data define such curve follow also a linear scale. The ionization is then seen to start out at a scaled electric field around  $0.25 \times 10^{-5}$  a.u. and rising towards unit probability around  $2 \times 10^{-5}$  a.u.

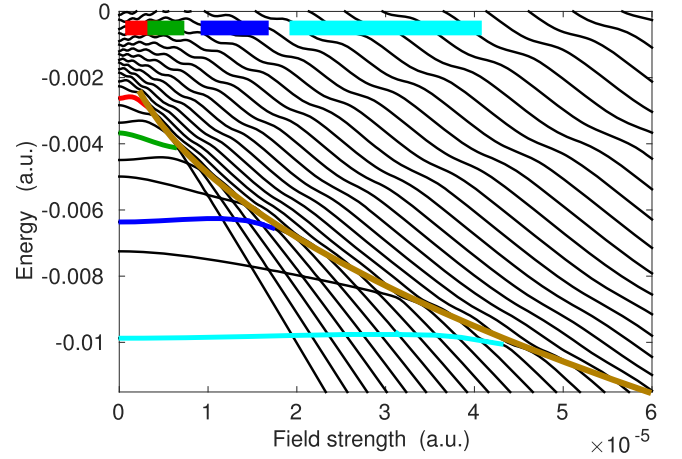


**Figure 4.** Adiabatic energy curves from  $n = 7$  and upwards following a diagonalization of the Hamiltonian for a range of electric field strengths. The  $n = 15$  (red),  $n = 12$  (green),  $n = 9$  (blue) and the  $n = 7$  (cyan) curves are highlighted. The field intensity range where the ionization from each of these states switches from 0 to 1 are shown as thick lines in the top of the figure. The thick brown line shows the value of the top of the barrier,  $T(E) = \max[V(x) + Ex]$ .

The calculated scaled ionization probabilities based on quantum mechanical calculations are shown in the lower panel of figure 3, and it is seen to obey the  $n^{-3}$  scaling relation as well. The onset of 1D ionization agrees with 3D experiments, while the response to the field after this point appears much stronger in 1D as compared to 3D. This discrepancy may have its origin in the reduced dimensionality. However, as the scaling behavior is identical, we believe that the 1D ionization mechanism is relevant for the real 3D processes as well.

The origin of the  $n^{-3}$  dependence has in [2] been explained as ‘a suppression of adiabatic ionization for weakly bound states’ implying a modified over the barrier process which can be reproduced by classical CTMC calculations. Here we will illustrate that this scaling behavior, at least within our 1D model, can alternatively be straightforwardly understood as quantum mechanical tunneling: In figure 4 we consider the 1D adiabatic energy curves obtained from the diagonalization of the Hamiltonian for increasing field strength. Adiabatic energy curves from  $n = 7$  and upwards are shown. We observe that the bound states in question all display an initial near linear response to the field, setting up almost parallel adiabatic energy levels towards the dense mesh of states belonging to the continuum. Even and odd states display have a small parity dependence in the initial slope. In the figure the  $n = 15, 12, 9, 7$  levels are highlighted as red, green, blue and cyan curves, respectively. At high enough field strength the bound states cross with an increasing number of states originating from the continuum. The thick lines indicate the electric field strength ranges where the corresponding ionization probability displayed in figure 3 switches from zero to unity. This range coincides with the region where crossings with states from the continuum appear. The thick brown line shows the value of the top of the barrier,  $T(E) = \max[V(x) + Ex]$ . As this field strength is approached, the ionization probability for any

initial  $n$  state has reached unity. Thus, the ionization process is identified as barrier tunneling.

The obtained  $n^{-3}$  scaling of the ionization probability is indicated in a large number of theoretical treatments of tunneling in the literature: for 1D field, the emission ionization probability raises from zero to unity, and a roughly triangular barrier has to be passed. In this case, a strong field tunneling formula has been derived recently which for a triangular barrier gives an exact  $n^{-3}$  scaling [16]. For a weak field tunneling from atoms, both in 1D and 3D, one can also obtain a perfect  $n^{-3}$  scaling when considering tunneling from the asymptotic form of the wavefunction,  $\Psi_n(r) \sim \exp(-r/n)$  [17–19]. However, the derivation of a general tunneling formula in the dynamical case is a rather complex exercise which we consider beyond the scope of the present work.

In the experiment it was observed that the emitted electrons from the most deeply bound Rydberg states leave the atom with the highest kinetic energies. This feature was in fact described as ‘counter intuitive’ [2]. We here show that the phenomenon is a direct consequence of the tunneling process. Let us take the midpoint of the thick lines as the estimate of the critical field strength required to release the electron into the continuum from a zero field state  $n$ , and denote this field strength as  $E_c^n$ . With reference to figure 2, this happens in the experiment near the final negative extremum of the electric field. Neglecting the initial momentum of the electron, and its interaction with the binding potential after release, the final momentum is determined by integrating the electric field from the time of release  $T_c^n$  to the end of the pulse at  $T/\beta$ ,

$$p_f^n = \frac{E_0}{\omega} [1 + \cos(\beta\omega T_c^n)]. \quad (4)$$

The release time then follows from equation (2),

$$T_c^n = \frac{1}{\beta\omega} \sin^{-1} \left( -\frac{E_c^n}{\beta E_0} \right). \quad (5)$$

By setting this equation into equation (4), the final momentum can be considered in two pulse strength regions. In the first case, the critical field strength  $E_c^n$  is equal or only slightly less than the pulse strength  $\beta E_0 \simeq E_c^n$ . In the second case, it is significantly smaller, i.e.  $E_c^n \ll \beta E_0$ . In latter case, a Taylor expansion applies to both equations (4) and (5), leading to

$$p_f^n \propto \begin{cases} \frac{E_0}{\omega}, & \text{when } \beta E_0 \simeq E_c^n \\ \frac{(E_c^n)^2}{2\omega E_0}, & \text{when } \beta E_0 \gg E_c^n. \end{cases} \quad (6)$$

Thus, at experimental conditions of figure 3, the ejected momenta from a fixed state,  $n$ , will be proportional to pulse strength,  $E_0$ . At higher pulse strengths, the increase of electron momenta will stop, while at extreme field strengths, it will decrease with increasing field. The latter is a direct consequence of the zero dc-component of the field,  $0 = \int_{-T}^{T/\beta} E(t) dt$ .

Now, we consider the final electron momenta originating from different  $n$ -levels. In the first case in equation (6) above, the requirement to obtain  $\beta E_0 \simeq E_c^n$  implies that  $E_0$  must

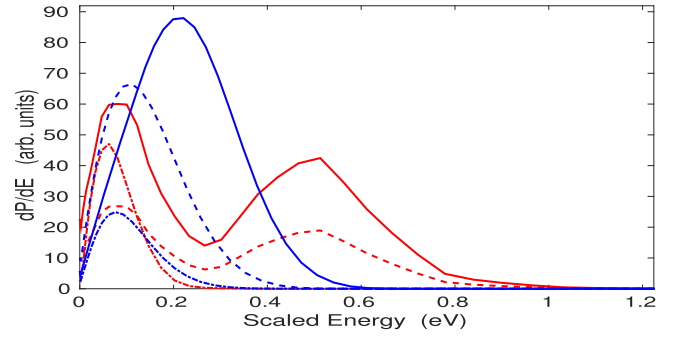


**Figure 5.** One dimensional differential kinetic emission energy,  $dP/dE$  for the initial  $n = 15$  (red) and  $n = 9$  (blue) levels, and three field strengths corresponding to ionization probabilities of 11% (dashed-dotted line), 50% (dashed line) and 90% (full line) for  $n = 9$  (18%, 40% and 90% for  $n = 15$ ). The momenta of the  $n = 9$  level has been multiplied by  $(9/15)^3$ .

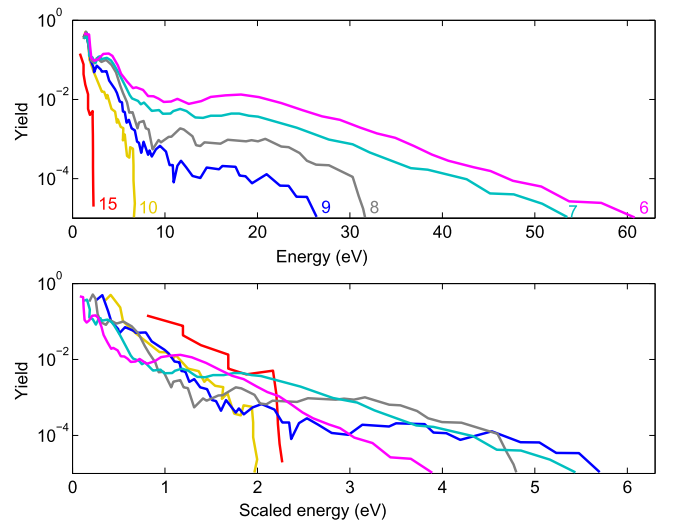


**Figure 6.** The top panel shows approximately digitized measured spectrum of ejected electron energies from [2] for the initial  $nd$  states given. The lower panel shows the same spectrum after scaling the electron momenta of each  $n$ -level according to  $\left(\frac{n}{n_{\max}}\right)^3$ .

scale in the way as  $E_c^n$ . Thus, increasingly more tightly bound electrons from lower  $n$  levels will be emitted with a characteristic momentum range of the order  $(n_{\max}/n)^3$  where again,  $n_{\max}$  is the highest initial principal quantum number obeying the scaling law.

We now investigate these two predictions within our 1D model: as an example, we display in figure 5 the kinetic energy distribution for  $n = 9$  and  $n = 15$ , and three pulse strengths corresponding to ionization probabilities (10%–20%, 40%–50% and  $\sim 90\%$ ) from each  $n$ -level. Following the preceding argument, we scale the momenta for the  $n = 9$  initial state by a factor  $(9/15)^3$ . We then observe that both the above predictions are valid: The scaling puts the initial  $n = 9$  momenta on the same range as the  $n = 15$  ones. Further, within each initial  $n$ -level, there is a tendency to a shift in the spectrum to higher characteristic momenta as the pulse strength increases, as expected from equation (6).

For completeness, we represent in figure 6 the measured ejected electron momenta for fixed pulse strength of [2]. Here we have again digitized approximately the data of figure of [2] and scaled them by the above suggested factor. In the upper panel, the published data are depicted on a linear energy scale. The lower panel shows the results when each  $n$ -level momentum is scaled according to the above-mentioned procedure. Clearly, the scaling procedure brings the data into a rather narrow range but does not put all scaled distributions onto any single universal curve. From the analysis above, at least two complicating factors interfere with the simple feature which would lead to a universal curve. Those are the effect of the binding potential on the free electron and the fact that the release time itself has a finite range.

Finally we address one more prediction of [1], namely the transition from a  $n^{-3}$  scaling law at intermediate  $n$ -levels to a  $n^{+2}$  scaling at high  $n$ -levels. Here we put forward a simple and different explanation, based on the displacement parameter  $\alpha$  of equation (3): increasing  $n$  implies an increasing earlier electron release to the continuum from which the trajectory is approximately following  $\alpha(t)$ . At the end of the pulse, the electron position in our case is given by  $\alpha(T/\beta)$ , and to end up as a free electron this position must be outside that of the original orbital radius, i.e.  $\alpha(T/\beta) > n^2$ . Thus, any fixed ionization probability for high initial  $n$ -levels scales accordingly. Setting in for  $\alpha$ , we obtain the highest  $n$ -level obeying the  $n^{-3}$  scaling from,

$$\frac{E_0}{\omega} T \left( 1 + \frac{1}{\beta} \right) \leq n_c^2 \quad (7)$$

which defines the critical  $n$ -value,  $n_c$ . Equality in the equation above for our parametrization gives  $n_c = \sqrt{\frac{5E_0}{3\pi}} T$  since  $\omega = \pi/T$ . This formula agrees well with the numerical results obtained in [1].

#### 4. Concluding remarks

In this work we have demonstrated that the ionization probability of Rydberg atoms in single cycle THz pulses with principal initial quantum number  $n \in [6, 15]$  scales well according to an  $n^{-3}$  power law for all ionization probabilities: when multiplying the electric pulse strength with the factor  $(n/n_{\max})^3$ , all the measured ionization probabilities fall onto a universal curve. A simple 1D model largely confirms the phenomenon, and the origin of the scaling law is understood as quantum tunneling. The same scaling model leads to an explanation of why the most tightly bound electrons are

emitted with the highest momenta: when applying the scaling relation to the final state momenta all distributions appear on a common narrow energy range.

The response of the electron to the field in full 3D space is clearly more complex. However, the present model suggests an alternative ionization mechanism as compared to the one put forward by Li and Jones [2]. It will be equally important to perform a similar analysis of full quantum 3D calculations at ‘experimental pulse conditions’. To the extent that the ionization mechanism goes via tunneling in 3D as well, the scaling behavior of CTMC calculations and quantal calculations is expected to be generally different,  $n^{-4}$  versus  $n^{-3}$  respectively.

#### Acknowledgements

The research has been supported in part by the Nordic top level research initiative (Nanocontrol Network) and with computational resources at UiB provided by NOTUR.

#### References

- [1] Yang B C and Robicheaux F 2014 *Phys. Rev. A* **90** 063413
- [2] Li S and Jones R R 2014 *Phys. Rev. Lett.* **112** 143006
- [3] Jones R R, You D and Bucksbaum P H 1993 *Phys. Rev. Lett.* **70** 1236
- [4] Pillet P, Smith W W, Kachru R, Tran N H and Gallagher T F 1983 *Phys. Rev. Lett.* **50** 1042
- [5] Yang B C and Robicheaux F 2015 *Phys. Rev. A* **91** 043407
- [6] Rasanen E 2016 (Private communications)
- [7] Gaillac R, Vacher M, Maquet A, Taïeb R and Caillat J 2016 *Phys. Rev. A* **93** 013410
- [8] Haines L K and Roberts D H 1969 *Am. J. Phys.* **37** 1145
- [9] Loudon R 1959 *Am. J. Phys.* **27** 649
- [10] Bandrauk A D and Shen H 1991 *Chem. Phys. Lett.* **176** 428–32
- [11] Cormier E and Lambropoulos P 1996 *J. Phys. B: At. Mol. Opt. Phys.* **29** 1667
- [12] Chelkowski S and Bandrauk A D 2002 *Phys. Rev. A* **65** 061802(R)
- [13] Hansen J P, Lu J, Madsen L B and Nilsen H M 2001 *Phys. Rev. A* **64** 033418
- [14] Martiny C P J and Madsen L B 2007 *Phys. Rev. A* **76** 043416
- [15] Ciappina M F, Pérez-Hernández J A, Shaaran T, Roso L and Lewenstein M 2013 *Phys. Rev. A* **87** 063833
- [16] Forbes R G 2008 *J. Appl. Phys.* **103** 114911
- [17] Yamabe T, Tachibana A and Silverstone H J 1977 *J. Phys. B: At. Mol. Phys.* **10** 2083
- [18] Yamabe T, Tachibana A and Silverstone H J 1977 *Phys. Rev. A* **16** 877
- [19] Tolstikhin O I, Morishita T and Madsen L B 2011 *Phys. Rev. A* **84** 053423





## **PAPER II**



# Classical and quantum-mechanical scaling of ionization from excited hydrogen atoms in single-cycle THz pulses

M. Chovancova,<sup>1</sup> H. Agueny,<sup>1</sup> J. J. Rørstad,<sup>2</sup> and J. P. Hansen<sup>1</sup>

<sup>1</sup>*Department of Physics and Technology, Allegt. 55, University of Bergen, N-5007 Bergen, Norway*

<sup>2</sup>*Department of Physics and Astronomy, Aarhus University, 8000 Aarhus C, Denmark*

(Received 19 April 2017; revised manuscript received 12 July 2017; published 25 August 2017)

Excited atoms, or nanotip surfaces, exposed to strong single-cycle terahertz radiation emit electrons with energies strongly dependent on the characteristics of the initial state. Here we consider scaling properties of the ionization probability and electron momenta of  $H(nd)$  atoms exposed to a single-cycle pulse of duration 0.5–5 ps, with  $n = 9, 12, 15$ . Results from three-dimensional quantum and classical calculations are in good agreement for long pulse lengths, independent of pulse strength. However, differences appear when the two approaches are compared at the most detailed level of density distributions. For the longest pulse lengths a mixed power law,  $n$ -scaling relation,  $\alpha n^{-4} + (1 - \alpha)n^{-3}$  is shown to hold. Our quantum calculations show that the scaling relation puts its imprint on the momentum distribution of the ionized electrons as well: By multiplying the emitted electron momenta of varying initial  $n$  level with the appropriate scaling factor the spectra fall onto a common momentum range. Furthermore, the characteristic momenta of emitted electrons from a fixed  $n$  level are proportional to the pulse strength of the driving field.

DOI: [10.1103/PhysRevA.96.023423](https://doi.org/10.1103/PhysRevA.96.023423)

## I. INTRODUCTION

Terahertz (THz) radiation technologies are at present advancing with promising perspectives in a wide range of scientific fields, from fundamental science to real-world applications [1]. Owing to the properties of THz radiation based on low photon energies, the emerging technology has been suggested as a useful source for medical imaging and security [2,3]. In recent years, investigation of single- and half-cycle THz pulses for driving nonlinear phenomena has become possible [4,5], which has exposed new phenomena. For instance, recently, it has been demonstrated experimentally that a strong single-cycle THz pulse applied to excited atoms [6] has led to electron emission with higher energies from tightly bound Rydberg states and with increasing pulse strength. Furthermore, a novel  $n^{-3}$  (where  $n$  is the quantum number) scaling has been found for the field strength required to attain 10% ionization probability, which later was shown to be valid for arbitrary ionization probability [7]. A similar phenomenon has been discovered for nanosized solid tips exposed to THz pulses: Increasingly narrow tips result in a spectrum of increasingly fast electrons [8]. Studies of the response of solid-state systems to THz radiation is in its infancy. In this context it is relevant to understand the detailed nature of the single atom response to THz radiation in order to separate potential collective phenomena from single atom effects.

On the theoretical side, for single-atom interactions, an empirical scaling relation for 10% ionization probability was put forward by Yang and Robichaux [9], which was shown to be valid for a wide pulse strength and duration range. It gives  $n^{-4}$  scaling for pulse durations larger than the classical orbit period of the Rydberg atom ( $T_n$ ) and a  $n^2$  scaling behavior for short pulses. In that work the quantum calculations are restricted to the initial  $n = 15$ ,  $l = 2$  states only while classical trajectory Monte Carlo (CTMC) calculations are the basis of the majority of their work. The dynamics of electron ionization from  $n = 15$  levels was further considered in great detail based on time-dependent Schrödinger equation (TDSE) and

CTMC calculations in parallel [10]. Here they found excellent agreement between the two approaches and showed that electron emission is strongly favoured along an axis pointing in the opposite direction of the electric polarization vector in the second half-cycle of the pulse. None of these calculations were compared directly with the experimental results of Ref. [6].

In this work we therefore analyze the degree of scaling of the ionization of hydrogen for arbitrary ionization probability from the initial  $n = 9, 12, 15$   $d$  states based on a full three-dimensional (3D) solution of the TDSE and CTMC method. We compare the results for pulses with various strengths and durations. In particular, we compare our results directly with the calculations in [10] and to the experiment in [6]. Furthermore, we explore the characteristics of the emitted electrons for different field ionization. We arrive at three main conclusions and results: First, the 3D quantum calculations, which are in agreement with Ref. [10], support a different scaling than the experimental results of Ref. [6]. Second, even though our CTMC and TDSE results in general agree well at the total probability level, clear discrepancies appear when the two methods are compared at the differential level. In Ref. [10] almost perfect agreement was reported for kinetic emission in the forward or backward direction. Third, we show that application of scaling to the momenta of the emitted electrons puts the spectra on almost the same momentum range. In the next section we describe the applied numerical procedures. Then we present and discuss the main results. Finally, concluding remarks are provided in the last section. Atomic units are used throughout unless otherwise stated.

## II. THEORETICAL MODEL

### A. TDSE

Within the semiclassical (strong-field) approximation we solve the TDSE,

$$\left[ H_e(\vec{r}, t) - i \frac{\partial}{\partial t} \right] \psi(\vec{r}, t) = 0, \quad (1)$$

where the electronic Hamiltonian contains the field-free Hamiltonian and the time-dependent interaction part given in the length gauge with electric field along the  $z$  direction,  $\vec{E}(t) = E(t)\vec{e}_z$ . To validate the results we first compare with the results in [10] where an exponential expression was used for the electric field,

$$E(t) = -\frac{E_0 C_0 t}{t_w} \exp \left[ -\left( \frac{t}{t_w} \right)^2 - 0.1 \left( \frac{t}{t_w} \right)^4 \right]. \quad (2)$$

Here  $E_0$  is the maximum pulse strength, and  $C_0, t_w$  are constants given in [10]. The remaining calculations are performed with a much simpler expression for the electric field,

$$E(t) = \begin{cases} -E_0 \sin(\omega t) & \text{if } -T < t < 0 \\ -E_0 \beta \sin(\beta \omega t) & \text{if } T/\beta > t > 0 \\ 0 & \text{otherwise,} \end{cases} \quad (3)$$

with  $\beta \sim 1.5$ . This equation grasps the main feature of a single-cycle THz pulse related to the experiments [6,8]; a first positive half-cycle of duration  $T$  and a shorter negative and more intense half-cycle of duration  $T/\beta$ . The pulse strength refers to the maximum value of the electric field, i.e.,  $E_0(n) = E_0 \beta$ , where  $n$  refers to the initial principal quantum number. There are two additional technical advantages of the field expressed by Eq. (3) as well: It can be integrated giving simple analytical expressions for the vector field  $A = -\int E(t')dt'$  and the free-field displacement  $\alpha = -\int A(t')dt'$ . Secondly, the pulse has a well defined start ( $-T$ ) and end time ( $T/\beta$ ). We obtain very similar results for the fields of Eqs. (3) and (2) for  $\beta = 1$ , but with a factor of 2 shorter simulation time.

Two major numerical challenges with strong THz pulses are related to the long integration times in addition to the required sizes of the numerical grids. Even if techniques have been developed to calculate differential quantities in special situations [11], the full wave function in general needs to be kept on the grid to allow for extraction of all measurable quantities accurately. In the present case at the strongest pulse strength, for example, the wave function initially propagates along the negative  $z$  axis and opposite in the final half-cycle. If the grid size is too small, a part of the wave function is absorbed in the first half-cycle and by that the dynamics in the second phase of the field becomes restricted.

The TDSE is integrated using the split-step Fleck-Hermann method [12]. The initial (hydrogen) Rydberg states considered throughout the investigation are analytically known. When put on the grid they are completely stable in absence of electric fields. Here, we need only to consider states with the  $m = 0$  component of the magnetic quantum number due to the field polarization. The time-dependent wave function is then expanded in spherical harmonics in the  $\theta$  and  $r$  coordinates as

$$\Psi(r_i, \theta_j, t) = \sum_{l=0}^{L_{\max}} f_l(r_i, t) Y_{l,0}(\hat{r}_j), \quad (4)$$

where  $\hat{r}_j = \theta_j$ . For general polarizations the sum runs over  $m$ -quantum numbers as well and the present formalism is perfectly valid in that case [13]. Then  $\hat{r}$  describes the two spherical angles,  $d\hat{r}$  describes integration over both and we

keep this more general notation in the following. We track the wave function up to radii up to  $r_{\max}$  from where an absorbing mask prohibits reflections. Numerical parameters applied ( $r_{\max}, \Delta r, L_{\max}, \Delta t$ ) are given in the figure captions. Once the time-dependent wave function is determined, on a sufficiently large grid containing the entire density, the wave function in momentum space is calculated using the same basis of spherical harmonics as in Eq. (4). We define the Fourier transform

$$\langle p | \Psi \rangle = \tilde{\Psi}(\vec{p}, t) = \int d^3r e^{-i\vec{p}\cdot\vec{r}} \Psi(\vec{r}, t) \quad (5)$$

and the plane wave expansion

$$e^{i\vec{p}\cdot\vec{r}} = 4\pi \sum_{L,M=0}^{\infty} i^L j_L(pr) Y_{L,M}^*(\hat{r}) Y_{L,M}(\hat{p}). \quad (6)$$

Here  $\hat{r}, \hat{p}$  denotes the spherical angles and  $j_L(x)$  is defined by the spherical Bessel function,  $J_n(x)$ ,  $j_L(x) = \frac{1}{\sqrt{x}} J_{L+0.5}(x)$ . Inserting this expansion into the Fourier transform we find that the radial expansion of Eq. (4) can be expressed in momentum space as

$$\tilde{\Psi}(\vec{p}, t) = \sum_{l=0}^{L_{\max}} \tilde{f}_l(p, t) Y_{l,0}(\hat{p}). \quad (7)$$

After the pulse, the continuum part of  $\tilde{\Psi}$  spans the basis describing ionization,  $\tilde{\Psi}^c(\vec{r}, t) = \tilde{\Psi} - \tilde{\Psi}^{\text{bound}}$ ,

$$\tilde{\Psi}^c(\vec{p}, t) = \sum_{l=0}^{L_{\max}} \tilde{f}_l^c(p, t_f) Y_{l,0}(\hat{p}). \quad (8)$$

The momentum functions  $\tilde{f}_l^c$  become the Fourier transform of the continuum part of the radial functions. These are obtained by projecting and subtracting all populated hydrogenic bound states at  $t_f$ . The differential scattering cross section for emission of an electron with momentum  $|p_n|$ , integrated over angles, can now be calculated from  $\tilde{\Psi}^c$ ,

$$\frac{d\sigma}{dp_n} = \int d\hat{p} p^2 |\langle p | \Psi(\vec{r}, t_f) \rangle|^2 = \sum_{l=0}^{L_{\max}} |p_n \tilde{f}_l^c(p_n, t_f)|^2. \quad (9)$$

The angular resolved cross section requires additional multiplication of phases connected to the long-range property of the Coulomb potential. To achieve the correct expression it is convenient to start from a conventional basis state expansion of the time-dependent wave function,

$$\Psi(\vec{r}, t_f) = \sum_m a_m(t_f) \Phi_m(\vec{r}) + \sum_n b_n(t_f) \Phi_n^c(\vec{r}). \quad (10)$$

Here, the sum over  $m(n)$  runs over all bound (discretized continuum) states inside a sphere with radius  $r_{\max}$ . The basis functions are the product of radial and angular states,  $\Phi_k(\vec{r}) = \phi_k(r) Y_{l,0}(\hat{r})$ , and the grid is assumed to span the entire wave function after the pulse,  $1 = \sum_m |a_m(t_f)|^2 + \sum_n |b_n(t_f)|^2$ . The connection between the set  $\Psi_n$  and the correct outgoing scattering states of the Coulomb problem is obtained when expressing the latter in terms of the discretized basis defined

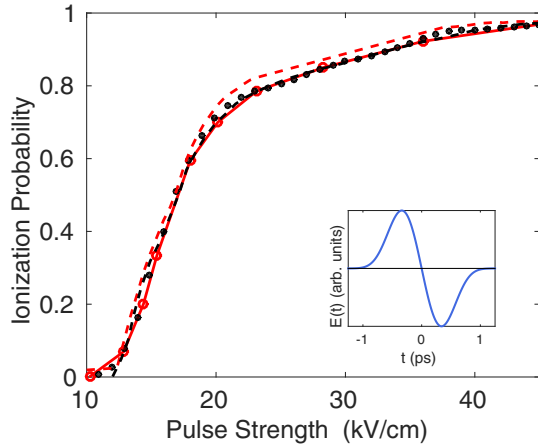


FIG. 1. Ionization probabilities as a function of pulse strength for the symmetric pulse, Eq. (2), sketched in the inset and applied in [10]. The black dashed line is the TDSE results and the dots are the CTMC results from [10]. The red (dark-gray) bulleted curve displays the present TDSE results and the red (dark-gray) dashed line the CTMC results. Parameters for the TDSE computations:  $r_{\max} = 4000$ ,  $\Delta r = 0.2441$ ,  $L_{\max} = 128$ ,  $\Delta t = 0.05$  and pulse parameters:  $t_w = 2.067\,069 \times 10^4$ ,  $C_0 = 2.385\,525\,5$ .

above,

$$\Psi_C(\vec{r}) = \frac{1}{p} \sum_{l=0}^{\infty} \sum_n i^l e^{i\delta_l} \phi_{n,l}^c(r; p_n) Y_{l,0}^*(\hat{p}) Y_{l,0}(\hat{r}), \quad (11)$$

where the Coulomb phase shift is  $\delta_l = \arg[\Gamma(l+1+i/p)]$  [14]. The projection of the numerical basis of Eq. (10) then becomes

$$\langle \Psi_C | \Psi \rangle = \frac{1}{p} \sum_{l=0}^{L_{\max}} \sum_n (-i)^l e^{-i\delta_l} b_n(t_f) Y_{l,0}(\hat{p}). \quad (12)$$

The differential angular cross section for emission of an electron with any energy in the direction  $d\hat{p}$  then becomes

$$\begin{aligned} \frac{d\sigma}{d\hat{p}} &= \int dp p^2 |\langle \Psi_C | \Psi \rangle|^2 \\ &= \sum_n \left| \sum_{l=0}^{L_{\max}} (-i)^l e^{-i\delta_l} b_n(t_f) Y_{l,0}(\hat{p}) \right|^2. \end{aligned} \quad (13)$$

Note that amplitudes of the numerical simulation have to be augmented by the Coulombic phase factors before integration. The same procedure must be carried through for the grid expansion of Eq. (4). Starting again with the projection on the Coulomb functions,

$$\langle \Psi_C | \Psi \rangle = \int d^3r \langle \tilde{\Psi}_C | \vec{r} \rangle \langle \vec{r} | \Psi \rangle = \sum_{l=0}^{L_{\max}} (-i)^l e^{-i\delta_l} \tilde{f}_l^C(p) Y_{l,0}(\hat{p}). \quad (14)$$

By comparing this expression with Eq. (8) we identify  $\tilde{f}_l^C(p) = \tilde{f}_l^C(p)$  and we note that Coulomb phase shifts need to be augmented precisely as in the case of eigenstate expansions, Eqs. (13) and (12). The differential cross sections for emission of an electron with momentum  $p_n$  along the direction  $d\hat{p}$  then

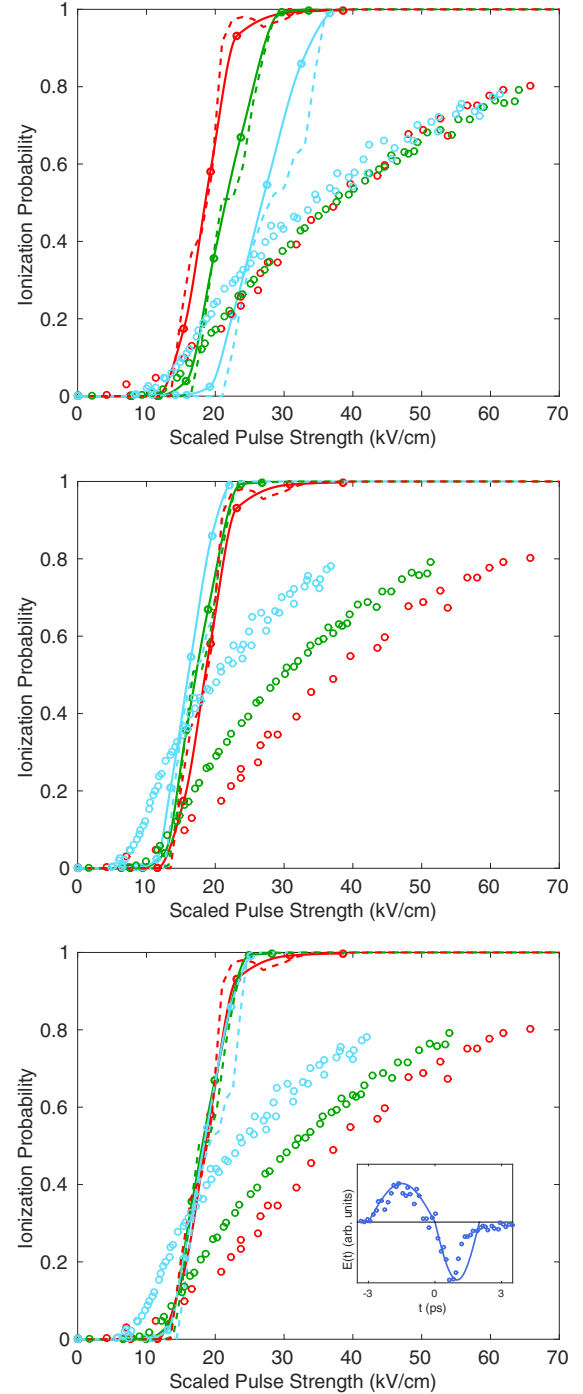


FIG. 2. Ionization probabilities as a function of scaled pulse strength for a pulse shape comparable to the experiment of [6] (cf. inset in the lower panel). Pulse parameters from Eq. (3) are  $T = 124\,020$  a.u. ( $\omega = 2.533\,13 \times 10^{-5}$  a.u.),  $\beta = 1.5$ . Probabilities are shown as a function of scaled pulse strength. The upper (middle) panel shows the experimental and computational results based on a  $n^{-3}$  ( $n^{-4}$ ) scaling. The lower panel shows the results for the mixed scaling Eq. (20), with  $\alpha = 0.2$ . Color coding is according to the initial  $n$  state with  $n = 15$  as red (dark-gray) lines,  $n = 12$  as green (gray) lines, and  $n = 9$  as blue (light-gray) lines. Full curves are TDSE results, broken curves are CTMC results, and bullets are experimental data from [6] with the same color coding. Parameters of the TDSE computations:  $r_{\max} = 4000$ ,  $\Delta r = 0.2441$ ,  $L_{\max} = 128$ ,  $\Delta t = 0.05$ .

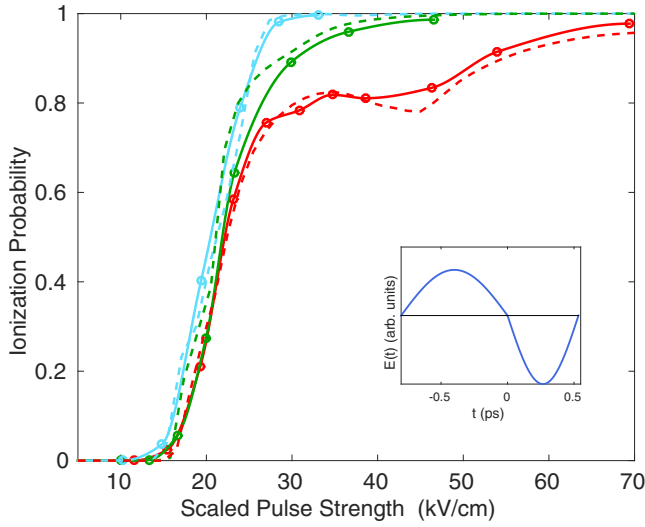


FIG. 3. Ionization probabilities as a function of scaled pulse strength for a pulse shape of Eq. (3), comparable in length to the pulse in Fig. 1. Results are plotted in terms of the mixed scaling Eq. (20), with  $\alpha = 0.2$ . Pulse parameters are  $T = 33073.0$  a.u. ( $\omega = 9.49896 \times 10^{-5}$  a.u.),  $\beta = 1.5$ . Color coding is according to the initial  $n$  state with  $n = 15$  as red (dark-gray) lines,  $n = 12$  as green (gray) lines, and  $n = 9$  as blue (light-gray) lines and full curves are TDSE results. Parameters of the TDSE computations:  $r_{\max} = 4000$ ,  $\Delta r = 0.2441$ ,  $L_{\max} = 128$ ,  $\Delta t = 0.05$ .

becomes

$$\frac{d\sigma}{dp_n d\hat{p}} = p_n^2 |\langle \Psi_C | \Psi \rangle|^2 = \left| \sum_{l=0}^{L_{\max}} (-i)^l e^{-i\delta_l} p_n \tilde{f}_l^c(p_n, t_f) Y_{l,0}(\hat{p}) \right|^2. \quad (15)$$

Thus, the differential cross sections can be computed directly based on the available radial (momentum) basis  $\tilde{f}_l^c(r)$  [ $\tilde{f}_l^c(p)$ ] without explicit knowledge of the continuum basis function  $\phi_n$  of Eq. (12). For ionization from the  $n = 15$  initial state the final lowest electron momenta are relatively small, in fact of similar magnitude as the strength of the potential energy. Therefore the quantum angular scattering can be affected by the Coulomb phase shifts as well. The differential cross section for electron emission in the forward direction is obtained by integrating over angles corresponding to a positive [ $\theta \in (0, \pi/2)$ ] or negative [ $\theta \in (\pi/2, \pi)$ ]  $p_z$  momentum component,

$$\begin{aligned} \frac{dP^{\text{forward}}}{dp_n} &= \int_0^{\pi/2} \int_0^{2\pi} d\hat{p} \frac{d\sigma}{dp_n d\hat{p}}, \\ \frac{dP^{\text{backward}}}{dp_n} &= \int_{\pi/2}^{\pi} \int_0^{2\pi} d\hat{p} \frac{d\sigma}{dp_n d\hat{p}}. \end{aligned} \quad (16)$$

These quantities will be discussed at the end of the next section and compared with (phase-free) classical scattering.

### B. CTMC

In the CTMC method, Newton's equations are propagated for a large number of the initial conditions describing some main characteristics of an initial quantum probability density.

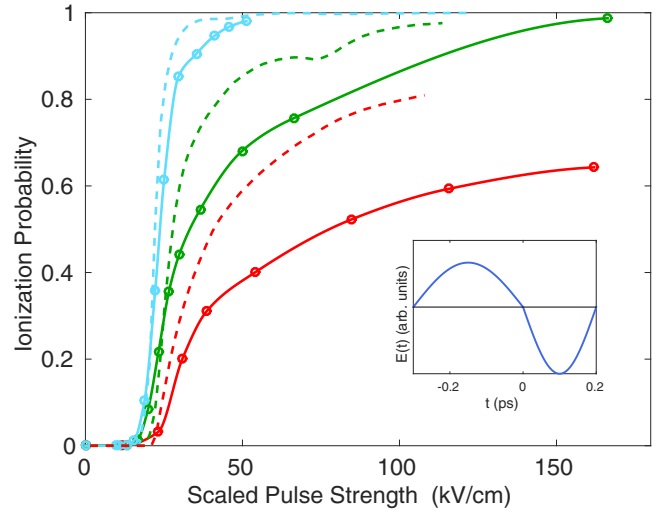


FIG. 4. Ionization probabilities as a function of scaled pulse strength, Eq. (20), for a pulse shape of Eq. (3), with duration only 10% of the pulse in Fig. 2,  $T = 12402.0$  a.u. ( $\omega = 2.53313 \times 10^{-4}$  a.u.),  $\beta = 1.5$ . Color coding is according to the initial  $n$  state with  $n = 15$  as red (dark-gray) lines,  $n = 12$  as green (gray) lines, and  $n = 9$  as blue (light-gray) lines and full curves are TDSE results. Parameters of the TDSE computations:  $r_{\max} = 4000$ ,  $\Delta r = 0.2441$ ,  $L_{\max} = 128$ ,  $\Delta t = 0.05$ .

This approach has been applied for decades within heavy particle collisions [15,16] before it was adopted in the study of atoms interacting with strong laser fields [17,18]. A variety of possibilities exist to select the initial distributions [19]. When ionization via tunneling is important an initial distribution of the initial electron position and momenta after tunneling is useful [20]. After propagating the electron positions and momenta according to a given time-dependent interaction, quantum phases may even be added in the final statistics [21].

The basic (standard) CTMC method which we will apply here is based on the selection of initial states which have a fixed energy identical to the initial quantum state in question. The simplest assumption that otherwise the probability density is a constant  $D$  is then in  $N$ -dimensional space,

$$D d^N r d^N p \delta[E(\vec{r}, \vec{p}) - E_0]. \quad (17)$$

This is referred to as the microcanonical distribution [22], which is based on the formal similarity with the concept of the microcanonical ensemble in statistical physics. There is no proof that this method should model well the quantum probability densities and the field-induced dynamics other than the results. And indeed, fine details related to differential quantities often display discrepancies with full quantum treatments [17,23].

In this approach the energy delta function limits the  $2N$ -dimensional space to  $2N - 1$  dimensions, with the necessity to find the  $2N - 1$  uniformly distributed variables. In 3D ( $N = 3$ ) space with two sets of spherical coordinates, the four angles are treated in the standard way of covering uniformly the two spheres in  $r$  and  $p$ . The remaining radial  $r$  and  $p$  must be described by only one uniformly distributed variable usually denoted  $w$ . This is obtained by transforming  $p^2 dp r^2 dr \rightarrow dE dw$  and  $p dp \rightarrow \mu dE$  so that the energy delta function can

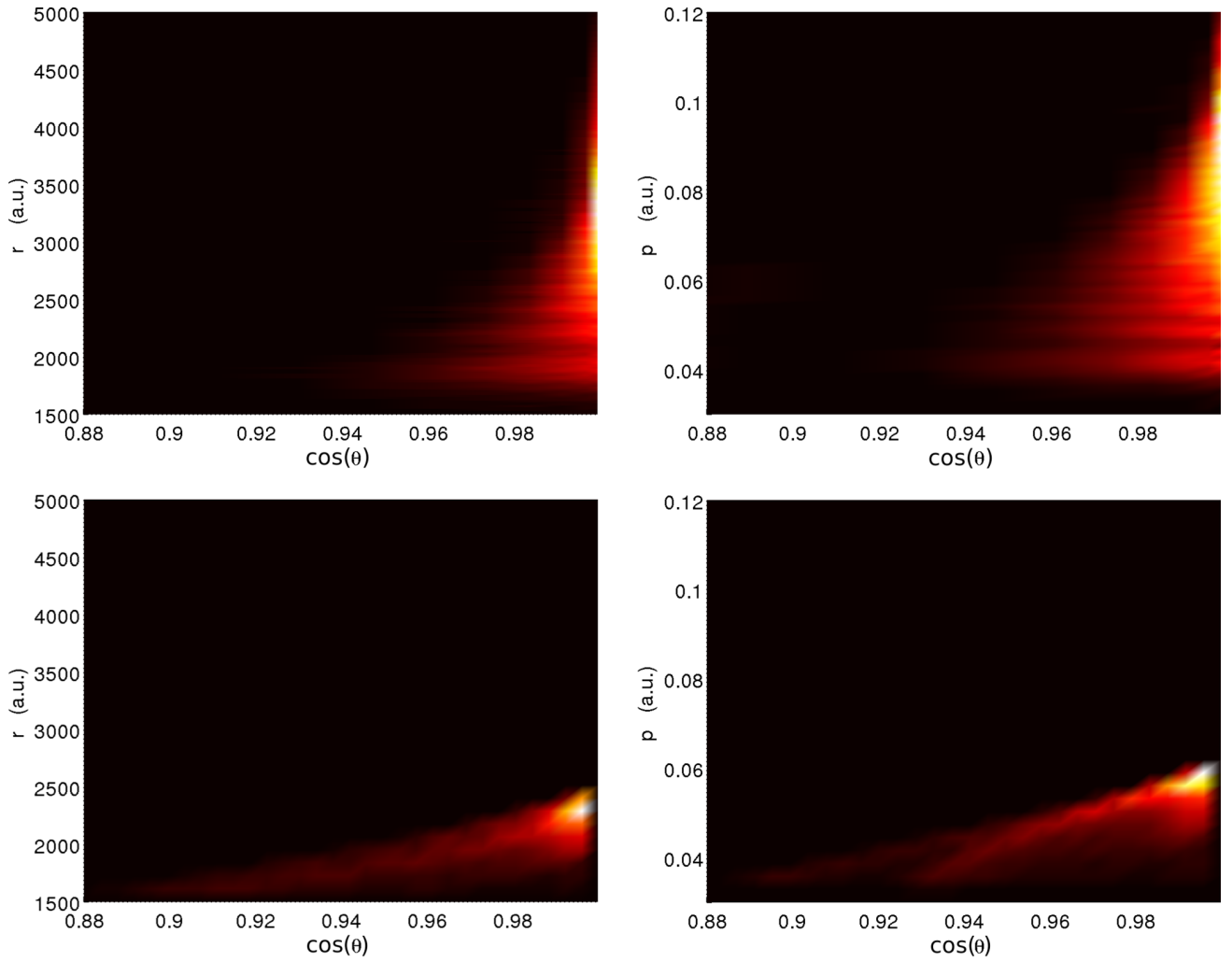


FIG. 5. Probability density distributions at the end of the pulse of the continuum part of the quantum wave function in position space,  $|\Psi^c[r, \cos(\theta), t_f]|^2$  (upper left) and momentum space  $|\Psi^c[p, \cos(\theta_p), t_f]|^2$  (upper right) for an initial  $15d$  state with a pulse strength corresponding to 20% ionization probability ( $E_0 = 18$  kV/cm) in Fig. 3. The lower panels show the corresponding densities from CTMC calculations. Pulse parameters from Eq. (3) are as in Fig. 2:  $T = 124\,020$  a.u. ( $\omega = 2.533\,13 \times 10^{-5}$  a.u.),  $\beta = 1.5$ . Parameters of the TDSE computations:  $r_{\max} = 16\,000$ ,  $\Delta r = 0.2441$ ,  $L_{\max} = 128$ ,  $\Delta t = 0.05$ .

be integrated over  $dE$ . The variable  $w$  can then be found from these requirements.

$$w(r) = \mu \int_0^r p(r')^2 dr' = \mu \int_0^r \sqrt{2\mu[E_0 - V(r')]} r'^2 dr'. \quad (18)$$

In this equation  $E_0$  is the fixed initial energy and  $\mu$  is the reduced mass. For more details, see Ref. [22].

In addition, to mimicking the initial  $Y_{l=2,m=0}$  character of the quantum initial state, we select only classical initial conditions with angular momentum  $l$ ,  $1.5 < l < 2.5$ , and  $|l_z| < 0.5$ . No sensitivity on the results to other limits for  $l \sim 2$ ,  $l_z \sim 0$  is found. Newton's equations are then propagated with up to 500 000 initial states using the adaptive integration method of Shampine and Gordon [24] and carefully checked by the ODE45 routine in MATLAB. In both cases an absolute (relative) error tolerance below  $10^{-7}$  ( $10^{-9}$ ) has been applied.

### III. RESULTS AND DISCUSSION

In the remainder of this paper, scaling laws will be discussed in connection with the ionization probabilities and their momentum distributions from TDSE and CTMC calculations. The angular distributions, which show distinct differences, will be additionally discussed at the end.

We start out by comparing the results of our methods with the results of Ref. [10]. Here, we restrict ourselves to the ionization probabilities as a function of the peak field for the hydrogen  $15d$  state, but test calculations with the initial  $15s$  show the same degree of agreement. The quantum probabilities are computed by subtracting from unity all bound-state probabilities pertaining to a sphere of a given radius (see Fig. 1 caption). The classical probabilities are obtained by the fraction of final states with positive energy after the pulse and the results from both approaches are plotted in Fig. 1. In the same figure the quantum and classical probabilities of [10] are shown. Results are shown for a



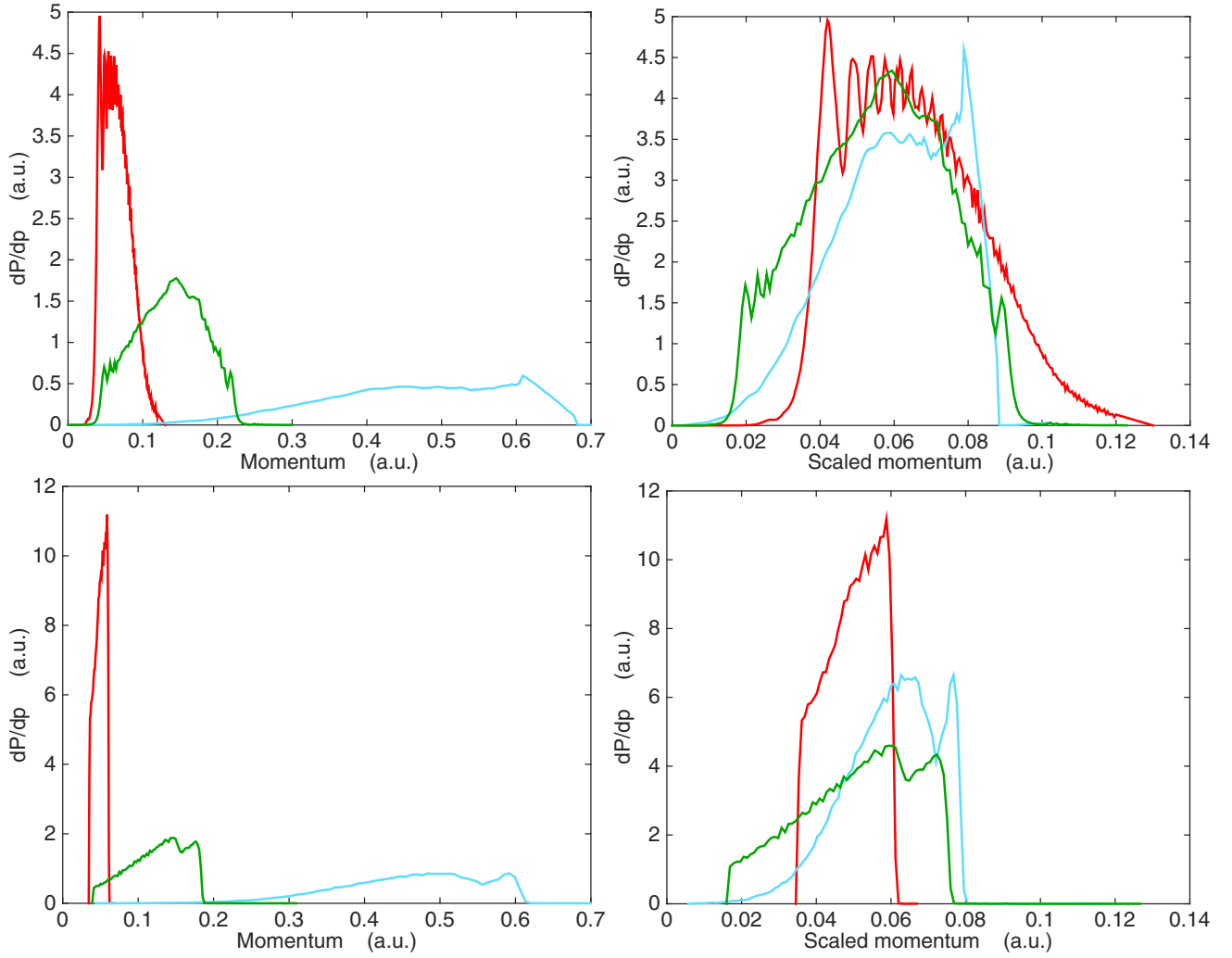


FIG. 6. Momentum distributions of the ionized electron based on the TDSE approach (upper) Eq. (9) and CTMC (lower), for initial states  $nd$  with  $n = 15$  as red curves (dark-gray),  $n = 12$  as green curves (gray), and  $n = 9$  as blue (light-gray) curves and for pulse strengths leading to 20% ionization probability from each initial  $n$  state ( $E_0 = 18$  kV/cm for initial  $n = 15$ ,  $E_0 = 36$  kV/cm for initial  $n = 12$ ,  $E_0 = 104$  kV/cm for initial  $n = 9$ ). The right column shows the same distributions except that the  $n = 12$  and  $n = 9$  momentum distributions have been scaled according to the mixed scaling relation, Eq. (20), with  $\alpha = 0.2$ . Pulse parameters from Eq. (3) are as in Fig. 2:  $T = 124\,020$  a.u. ( $\omega = 2.533\,13 \times 10^{-5}$  a.u.),  $\beta = 1.5$ . Parameters of the TDSE computations:  $r_{\max} = 16\,000$  ( $r_{\max} = 32\,000$  for  $n = 9$ ),  $\Delta r = 0.2441$ ,  $L_{\max} = 128$ ,  $\Delta t = 0.05$ . The CTMC results are based on 500 000 initial states.

symmetric pulse with a duration of  $\sim 2$  ps, and its form is illustrated in the inset of the Fig. 1. One can see that the present computed TDSEs are in excellent agreement with those reported in Ref. [10]. Our classical calculations (red dashed lines) very slightly overestimate the ones obtained in [10], possibly a result of different strategies to sample the initial conditions.

In [9] an empirical scaling law was shown to be valid for total ionization (at 10% ionization probability) for a large parameter range of initial states, pulse lengths, and strengths. This was based predominantly on classical calculations but included also results from a few quantum calculations. This scaling law implies a  $n^2$  scaling behavior for pulse durations shorter than the classical orbit period of the Rydberg atom ( $T_n \sim n^3$ ). At long pulse lengths, their scaling law reproduces the results of the classical over the barrier model, i.e., a  $n^{-4}$

scaling. In the transition region between these two extrema any kind of power/nonpower laws may occur, including the measured and reported  $n^{-3}$  scaling in [6].

Instead of testing scaling law in [9] for computations with different initial levels and probabilities, we here aim to investigate the possible degree of scaling at all ionization probabilities for selected single-cycle pulses. We will consider pulse lengths comparable to the  $n = 15$  orbit time of  $\sim 0.5$  fs, and upward to  $\sim 5$  fs, the experimental pulse length in [6]. In Fig. 2 we compare our calculated results with the experimental results directly and for various forms of scaling. In the upper panel the experimental ionization probabilities of the initial  $n = 9, 12, 15$  states are shown on a common scaled axis defined by  $(n/15)^3$  [7]. We observe that this scaling is excellent for the experimental results but rather poor for the calculations. On the other hand, TDSE and CTMC probabilities are in



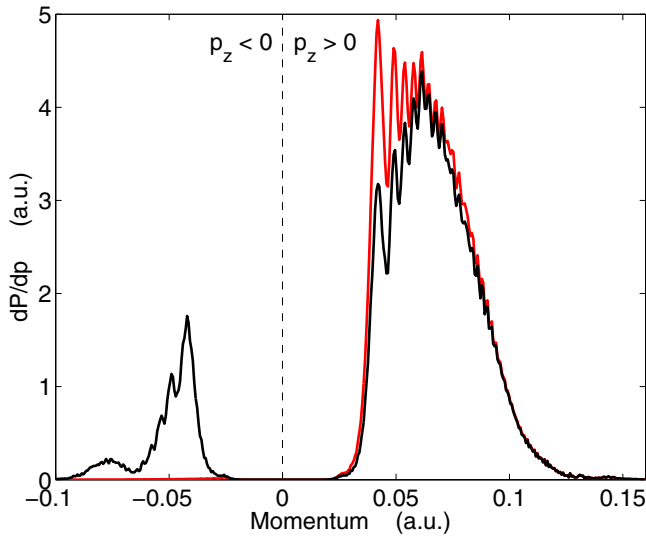


FIG. 7. Forward and backward quantum differential momentum emission probability (black curve) for the initial state  $n = 15d$ ,  $E_0 = 18$  kV/cm, Eq. (16), and compared to the momentum distribution of Eq. (9), the red (dark-gray) curve shown in Fig. 6. Parameters of the TDSE computations:  $r_{\max} = 16000$ ,  $\Delta r = 0.2441$ ,  $L_{\max} = 128$ ,  $\Delta t = 0.05$ .

good agreement. The situation switches by applying over the barrier scaling,  $(n/15)^4$  in the middle panel of Fig. 2. Now the calculations shows a higher degree of scaling while the scaling of the experimental results are poor.

A dynamical classical mechanism behind the observed  $n^{-3}$  scaling was put forward in Ref. [6]. Interestingly, a one-dimensional quantum tunneling mechanism provides the same power-law dependence independent of field strength [25]. In 3D, the weak-field adiabatic tunneling theory provides a leading exponential term which partly scales as  $n^{-3}$  as well [26]. Thus, tunneling offers a quantum-mechanical mechanism leading to the observed scaling. The strong external field does, however, open for over the barrier ionization as well. When the two processes takes place at the same time a combination of  $n^{-3}$  and  $n^{-4}$  scaling may show up in the results. A mixed power-law scaling factor would then emerge on the form

$$E_0^{sf}(n) = \alpha n^{-4} + (1 - \alpha)n^{-3}, \quad (19)$$

where the parameter  $0 \geq \alpha \leq 1$ . Given an ionization probability for a reference  $n$  level, say  $n = 15$ , the scaled pulse strength of ionization from other  $n$  levels at a given real pulse strength  $E_0(n)$  becomes

$$E_0^{\text{scaled}}(n) = \frac{E_0^{sf}(n)}{E_0^{sf}(n = 15)} E_0(n). \quad (20)$$

If the present scaling is universally valid the ionization probability for varying initial  $n$  levels falls on the same curve for a fixed value of the parameter  $\alpha$ . In the lower panel of Fig. 2 it is interesting to observe that the computed quantum ionization probabilities exhibit this property for  $\alpha = 0.2$ . Even the CTMC calculations display the same scaling property for ionization probabilities below 50%. However, putting the experimental results through this scaling procedure only

slightly improves the situation from the middle panel of Fig. 2. A potential origin of the discrepancy might be related to the fact that the experiment is performed with Na atoms and the calculations are with H atom(s). However, the quantum defects of the initial  $nd$  states in Na are very small and a complete change of scaling is hardly expected between the two atomic systems [9]. Given the agreement with independent calculations we can only conclude that we here document an unresolved discrepancy between theory and experiment which calls for an iteration or independent work on the experimental and possibly also on the computational side.

In Fig. 3 we show our results for a shorter pulse length than the one in Fig. 2, and comparable to the one in Fig. 1. In relation to Fig. 2 the time-dependent field now has a stronger (negative) pulse strength in the second half-cycle as compared to the first. We again note a sharp rise in the ionization probability at the same pulse strength range as in Figs. 1 and 2 and that the scaling procedure as outlined above works very well up to an ionization probability around 70%. At that point the  $n = 15$  ionization probability flattens out and oscillates, a mechanism discussed in [6]. It occurs when the pulse length becomes comparable to the classical orbit time,  $T_n \propto n^3$ . The results of a much shorter pulse duration ( $\sim 0.5$  ps) are shown in Fig. 4. At this point the scaling procedure is only valid at smallest ionization probabilities. At ionization probabilities exceeding 10% the results of classical and quantum calculations disagree. This indicates that the empirical scaling relation put forward in [9] is limited to small ionization probabilities only.

In the remaining part of this section we will study the momentum distributions in more detail. It generally requires much more computationally expensive calculations as the entire wave function needs to be kept on the grid until the electric field vanishes. The momentum and angular distributions indeed provide a deeper understanding of the ionization dynamics. In this context, it was found in the recent experiment [6], by measuring the electron energy distributions for different  $n$  states, that lower initial  $n$  gives generally higher energies of the emitted electrons. We address here two main questions: First, to which degree does the mixed scaling law of Eq. (19) imprint itself on the spectrum of emitted electrons? Second, to which extent do the CTMC and TDSE calculations agree when the differential distribution is studied in detail?

The starting point amounts to examining the ionization dynamics in the two-dimensional position and momentum spaces at the end of the laser pulse. Figure 5 shows the spatial distribution of the continuum part of the electron-probability density (left panels) and the corresponding momentum distribution (right panels) for the initial  $15d$  state at 20% ionization probability (see caption for further details). The distributions are quantum (upper panels) and classical (lower panels) and they are seen to display great differences. The spreading, the mean position, and momentum of the outgoing distribution differ. With a less detailed focus there are also common features: It is seen that the electron density which is nonzero along a limited range of  $(r, \cos \theta)$  values corresponds to ionized electrons propagating along the positive  $z$  axis and are centered at positive  $z$  values immediately after the pulse. This is consistent with the ionization dynamics taking part predominantly in the final half-cycle of the pulse. In the quantum results, we also observe the emergence of oscillatory

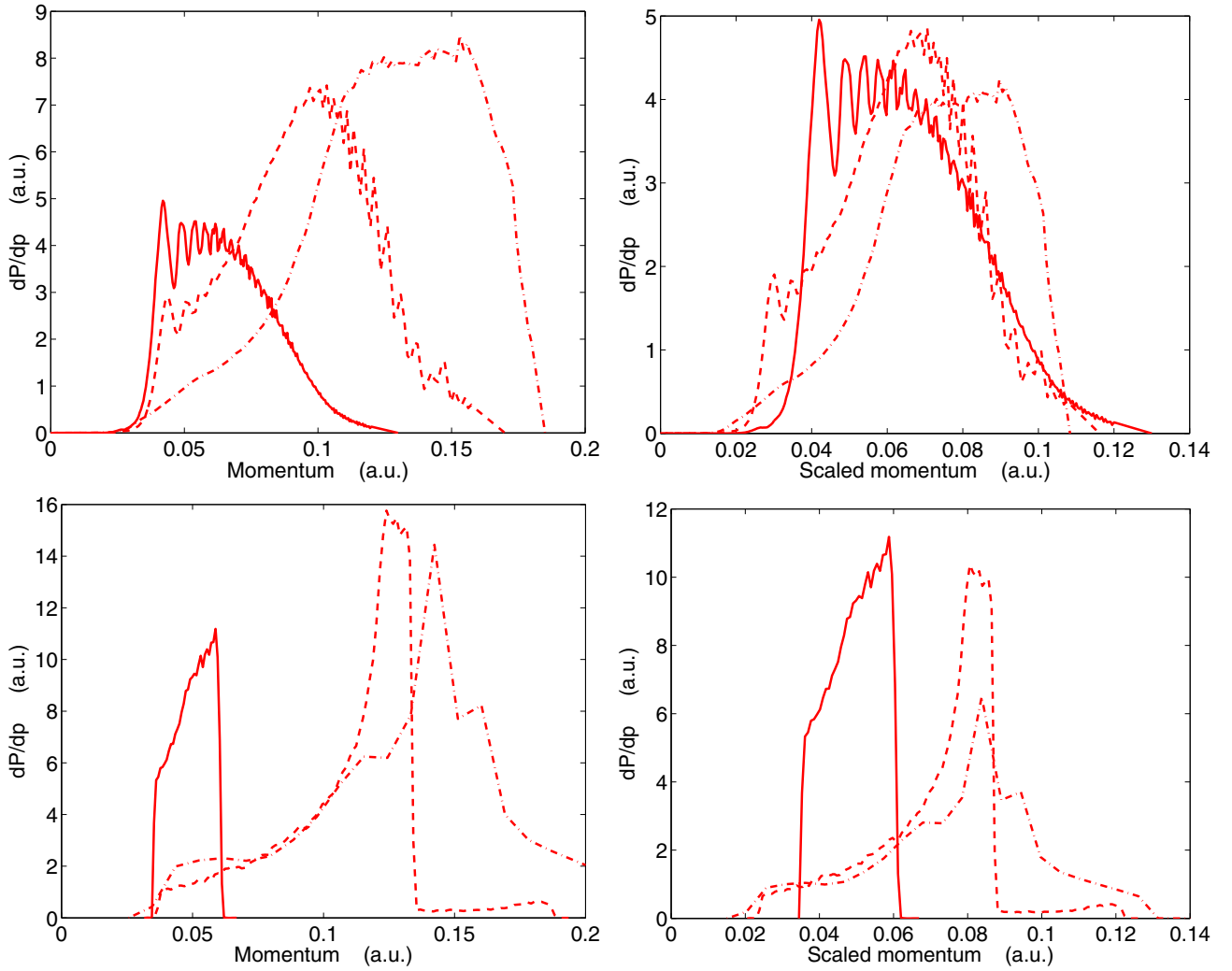


FIG. 8. Upper panels: Momentum distributions from the initial  $n = 15d$  state for three different pulse strengths  $E_0 = 15.8$  kV/cm (full line),  $E_0 = 18.5$  kV/cm (dashed line), and  $E_0 = 21.6$  kV/cm (dashed-dotted line). Pulse parameters from Eq. (3) are as in Fig. 2:  $T = 124\,020$  a.u. ( $\omega = 2.533\,13 \times 10^{-5}$  a.u.),  $\beta = 1.5$ . The pulse strengths give ionization probabilities of 20%, 50%, and 73% for the TDSE calculations. The upper right panel shows the distribution with a linearly scaled momenta [cf. Eq. (22)] and normalized to an ionization probability of 20%. Lower panels: Corresponding spectra based on CTMC calculations with 500 000 initial states. Parameters of the TDSE computations:  $r_{\max} = 16\,000$ ,  $\Delta r = 0.2441$ ,  $L_{\max} = 128$ ,  $\Delta t = 0.05$ .

wavelike structures which do not appear in classical results. A related phenomenon has been discussed previously in Refs. [27] in a multicycle extreme-ultraviolet pulse, and in studies of strong-field few-cycle ionization of the ground state about 20 years ago [17,28].

We turn now to discuss the scaling properties in connection with the momentum distributions of the ionized electrons. In Fig. 6 we have integrated the distributions over all angles and obtained the differential momentum distribution,  $dP/dp$ . In the left panel of Fig. 6 we show the unscaled quantum (upper panels) and classical (lower panels) distributions for three initial  $n = 9, 12, 15$  states all at  $\sim 20\%$  ionization probability. The general features of quantum distributions are reflected in the classical distributions. These are mainly manifested by a wider distribution describing higher electron momenta for decreasing  $n$ . By applying the mixed scaling relation, Eq. (19), to the final state momenta, one can now see that

the quantum distributions of all three initial states fall into a common range. To some extent the classical distributions also exhibit this property, but here the scaled range is “less common,” as shown in the right column of Fig. 6. This result is consistent with the release of the electron at a narrow range of critical pulse strengths, from which it essentially propagates with little influence of the binding potential, as discussed in [7,9].

The instantaneous CTMC distribution of Fig. 6 does not change at all by letting the particles propagate an additionally long time in the presence of the Coulomb potential only. For the quantum distribution it is not so: The low-energy part of the continuum waves, in particular, may be altered by the Coulomb potential. Thus Coulomb phases need to be added when computing the final differential forward or backward emission probability [cf. Eq. (15)]. This is displayed in Fig. 7 for the initial  $n = 15d$  results in Figs. 5 and 6. We observe

that indeed the Coulomb potential plays a role and causes the low-energy part of the emitted spectrum to be rescattered in the opposite direction from what is seen in Fig. 5. Thus, the forward-backward scattering asymmetry turns out to be different for TDSE and CTMC calculations as well, notably in disagreement with the results in [10] with other pulse shapes, strengths, and durations.

For completeness, we address in Fig. 8 the nature of the momentum distributions for an initial fixed  $n$  level and for different ionization probabilities. The left panel of Fig. 8 shows results at three comparable ionization probabilities for the initial  $n = 15d$ . Both the quantum distribution (upper panels) and the classical one (lower panels) show increasing momenta with increasing pulse strength. But again, the detailed distribution differs in shape. A possible scaling in this case can be argued for by assuming the ratio between the final momenta and the pulse strength of any ionization probability,  $x\%$ , is almost constant,

$$\frac{p(20\%)}{E_0(20\%)} = \frac{p(x\%)}{E_0(x\%)}. \quad (21)$$

This suggests a scaling relation of the form

$$p^{\text{scaled}}(x\%) = \gamma \frac{E_0(20\%)}{E_0(x\%)} p(x\%) \quad (22)$$

with  $\gamma \sim 1$  as a free fitting parameter may work. The spectra are additionally normalized to the same total area. We observe in Fig. 8 (right panel) that the momentum range of emitted electrons from the quantum results scale reasonably well for  $\gamma = 0.8$ , while the CTMC results differ much more, both in shape and final scaled momentum range.

#### IV. CONCLUDING REMARKS

We have considered the response of  $H(n = 9d, 12d, 15d)$  atoms to a single-cycle THz pulse with durations from 0.5 to

5 ps in classical and quantum-mechanical time propagation. A scaling law has been found to be generally valid for any ionization probability and for initial  $n = 9, 12, 15$  levels when the pulse length becomes similar to, or longer than, the classical period of the  $n$  levels under consideration. We further investigated the scaling behavior in connection with the ionized momentum distribution in the long-pulse regime. The same scaling property was here found to be valid in quantum distributions and to a much lesser degree for the classical approach. The Coulomb phases have been shown to be important in the quantum scattering process as well for the initial  $n = 15d$  state. Finally, a near linear response of the characteristic momentum range has been found for ionization from a fixed  $n$  state with increasing pulse strength.

Interestingly, these phenomena have a counterpart in THz radiation from nanotips, faster electrons from narrower tips, and a linear response for a fixed tip with increased pulse strength [8]. Further investigations in this direction may lead to new imaging devices where the electron spectrum from a fixed pulse may provide structural information of the tip region itself. Before that it seems important to further investigate the scaling relations validity for single atoms in strong THz fields. This applies to electron emission probabilities at the total as well as at the differential level and to converge on parameter ranges where ionization and scattering from classical and quantum based approaches agree.

#### ACKNOWLEDGMENTS

The research has been supported by UNINETT Sigma2 AS which manages the national infrastructure for computational science in Norway. Numerical calculations were carried out at the Cray XE6 (Hexagon) supercomputer installation at Parallab at the University of Bergen (UiB).

- 
- [1] S. S. Dhillon *et al.*, *J. Phys. D: Appl. Phys.* **50**, 043001 (2017).
  - [2] M. Tonouchi, *Nat. Photon.* **1**, 97 (2007).
  - [3] J. F. Federici, B. Schulkin, F. Huang, D. Gary, R. Barat, F. Oliveira, and D. Zimdars, *Semicond. Sci. Technol.* **20**, S266 (2005).
  - [4] J. L. LaRue, T. Katayama, A. Lindenberg, A. S. Fisher, H. Öström, A. Nilsson, and H. Ogasawara, *Phys. Rev. Lett.* **115**, 036103 (2015).
  - [5] K. Kovács, E. Balogh, J. Hebling, V. Tosa, and K. Varjú, *Phys. Rev. Lett.* **108**, 193903 (2012).
  - [6] S. Li and R. R. Jones, *Phys. Rev. Lett.* **112**, 143006 (2014).
  - [7] H. Agueny, M. Chovancova, J. P. Hansen, and L. Kocbach, *J. Phys. B: At., Mol. Opt. Phys.* **49**, 245002 (2016).
  - [8] S. Li and R. R. Jones, *Nat. Commun.* **7**, 13405 (2016).
  - [9] B. C. Yang and F. Robicheaux, *Phys. Rev. A* **90**, 063413 (2014).
  - [10] B. C. Yang and F. Robicheaux, *Phys. Rev. A* **91**, 043407 (2015).
  - [11] L. Tao and A. Scrinzi, *New J. Phys.* **14**, 013021 (2012).
  - [12] M. R. Hermann and J. A. Fleck, Jr., *Phys. Rev. A* **38**, 6000 (1988).
  - [13] J. P. Hansen, T. Sørsvik, and L. B. Madsen, *Phys. Rev. A* **68**, 031401(R) (2003).
  - [14] P. G. Burke, *R-Matrix Theory of Atomic Collisions* (Springer Verlag, Berlin, 2011).
  - [15] N. C. Blais and D. L. Bunker, *J. Chem. Phys.* **37**, 2713 (1962).
  - [16] R. Abrines and I. C. Percival, *Proc. Phys. Soc.* **88**, 861 (1966).
  - [17] J. P. Hansen, J. Lu, L. B. Madsen, and H. M. Nilsen, *Phys. Rev. A* **64**, 033418 (2001).
  - [18] J. S. Cohen, *Phys. Rev. A* **64**, 043412 (2001).
  - [19] N. D. Cariatore, S. Otranto, and R. E. Olson, *Phys. Rev. A* **93**, 066702 (2016).
  - [20] J.-P. Wang and F. He, *Phys. Rev. A* **95**, 043420 (2017).
  - [21] E. A. Solov'ev, *Eur. Phys. J. D* **65**, 331 (2011).
  - [22] C. O. Reinhold and C. A. Falcón, *Phys. Rev. A* **33**, 3859 (1986).

- [23] A. Dubois and J. P. Hansen, *J. Phys. B: At., Mol. Opt. Phys.* **29**, L225 (1996).
- [24] L. F. Shampine and M. K. Gordon, *Computer Solution of Ordinary Differential Equations: The Initial Value Problem* (Freeman, San Fransisco, 1975).
- [25] R. G. Forbes, *J. Appl. Phys.* **103**, 114911 (2008).
- [26] T. Yamabe, A. Tachibana, and H. J. Silverstone, *Phys. Rev. A* **16**, 877 (1977).
- [27] I. A. Ivanov, A. S. Kheifets, K. Bartschat, J. Emmons, S. M. Buczek, E. V. Gryzlova, and A. N. Grum-Grzhimailo, *Phys. Rev. A* **90**, 043401 (2014).
- [28] E. Cormier and P. Lambropoulos, *Eur. Phys. J. D* **2**, 15 (1998).

## **PAPER III**



# Spatial transport of electron quantum states with strong attosecond pulses

M Chovancova, H Agueny, M Førre, L Kocbach and J P Hansen<sup>1</sup> 

Department of Physics and Technology, Allegt. 55, University of Bergen, N-5007 Bergen, Norway

E-mail: [jan.petter.hansen@chalmers.se](mailto:jan.petter.hansen@chalmers.se)

Received 6 July 2017, revised 18 September 2017

Accepted for publication 28 September 2017

Published 20 October 2017



## Abstract

This work follows up the work of Dimitrovsky, Briggs and co-workers on translated electron atomic states by a strong field of an atto-second laser pulse, also described as creation of atoms without a nucleus. Here, we propose a new approach by analyzing the electron states in the Kramers–Henneberger moving frame in the dipole approximation. The wave function follows the displacement vector  $\alpha(t)$ . This allows arbitrarily shaped pulses, including the model delta-function potentials in the Dimitrovsky and Briggs approach. In the case of final-length single-cycle pulses, we apply both the Kramers–Henneberger moving frame analysis and a full numerical treatment of our 1D model. When the laser pulse frequency exceeds the frequency associated by the energy difference between initial and final states, the entire wavefunction is translated in space nearly without loss of coherence, to a well defined distance from the original position where the ionized core is left behind. This statement is demonstrated on the excited Rydberg states ( $n = 10$ ,  $n = 15$ ), where almost no distortion in the transported wave functions has been observed. However, the ground state ( $n = 1$ ) is visibly distorted during the removal by pulses of reasonable frequencies, as also predicted by Dimitrovsky and Briggs analysis. Our approach allows us to analyze general pulses as well as the model delta-function potentials on the same footing in the Kramers–Henneberger frame.

Keywords: attosecond pulses, displacement, imaging, quantum control

(Some figures may appear in colour only in the online journal)

## 1. Introduction

Attosecond pulses open new possibilities of manipulating atomic and molecular states and also enable monitoring of electron motion on the atomic time scale [1]. They also add new possibilities to address deep fundamental questions of quantum physics earlier considered only in so called Gedanken-experiments, e.g. already in [2]. On the other hand, these new tools also build further on several decades of development of increasingly more sophisticated applications of laser pulses in a broad range of frequencies and combinations of various types pulses. From a theoretical point of view, it is possible to search for mechanisms and similarities across experimentally deeply separated areas. It should thus not be very surprising that this contribution to the theory relevant for attosecond physics originates from our theoretical analysis of ionization of atoms by terahertz pulses [3]. In that work, the challenge was to describe

correctly ionization by a very strong but very slow single cycle pulse (terahertz region), trying to contribute to understanding of the ionization dynamics underlying the experiments by Li and Jones [4]. Our analysis of these experiments were performed in the Kramers–Henneberger frame [3, 5], as opposed to a fixed frame analysis [6].

The main challenge in our discussed work has been the very long character of the pulses, requiring a very long numerical time integration. For the purpose of testing, we would make test runs with much stronger and very much shorter pulses—and we have accidentally observed the phenomenon which is the subject of this paper: for sufficiently sharp strong electric field pulse an atomic state, i.e. the electron density is moved in a direction in the direction of the electric force, while the nucleus remains in its original position. In a series of works about a decade ago [7–9], Briggs and Dimitrovski *et al* (BD) developed a theory for ionization of atoms by a short strong laser pulse. Their work is based on the first order Magnus expansion [10] which has been widely applied in collision processes involving

<sup>1</sup> Author to whom any correspondence should be addressed.



impulsive perturbations [11–13]. They considered a model where a short half cycle electric field were approximated by an instantaneous Dirac  $\delta$ -function. Their theory resulted in analytical, closed form expressions, for the transition amplitudes from a bound state to a continuum state with momentum  $\vec{q}$ . In the final work [14], they noted that a second half cycle field of equal strength and opposite amplitude can bring the ionized electron to rest with its initial wavefunction intact.

In the present work, we provide an alternative theory for this phenomenon. As in the case of complete electron removal in slow single cycle pulses we show that the description in the Kramer–Henneberger frame [15] offer a simple description of the dynamics. Simulations show that the criteria for wavefunction translation are fulfilled by a  $10^{14}$  W cm $^{-1}$ , 800 nm single cycle pulse applied to Rydberg atoms. It should be mentioned that a very similar analysis has been used by Zuo *et al* in [16], but for a different type of process, now known as laser induced electron diffraction. There only the half pulse single delta-function is used, with the same effect as the first of the two pulses in this case and it is of interest to observe that the mechanism considered here has already been observed in very different physical situation.

When the condition for a ‘clean removal of the nucleus’ are fulfilled, meaning actually that the electron cloud is put away, the atomic state is moved along a trajectory described by the time-dependent displacement parameter of the Kramer–Henneberger type. This implies that the distance the wave function is removed from its nucleus during a single pulse is exactly known. A sequence of suitable pulses could bring the electronic state as far away from its original position and parent nucleus as requested. From that distance electron correlations or an image of a transient coherent wavepacket will be imprinted in its subsequent time development. As noted by BD, this may constitute an interesting new imaging technique since the final decay of the electronic wavepacket can take part completely isolated from its nucleus. Imprinted characteristics in the initial electronic wavefunction of electron correlations, quantum entanglement or dynamics may be read out directly from the emission pattern since the fragmentation, or free-expansion in the one-electron case, occurs in the absence of a nucleus.

## 2. Theory

We consider the single electron time-dependent Schrödinger equation (TDSE)

$$\left[ -\frac{1}{2}\nabla^2 + V(x) + E(t)x - i\frac{\partial}{\partial t} \right] \psi(x, t) = 0 \quad (1)$$

for an atomic electron in a time dependent electric field  $E(t)$  of a strong pulse. The electric field and the vector potential are trivially related by

$$A(t) = -\int_{t_i}^t E(t') dt' \quad (2)$$

but this integral plays also another role. If a classical electron at rest is exposed to the electric field  $E(t)$ , it will be accelerated to a time-dependent velocity  $v(t) = A(t)$  of equation (2)

and will be displaced from its rest position by the displacement vector

$$\alpha(t) = \int_{t_i}^t A(t') dt'. \quad (3)$$

Numerical calculations are performed for this problem with the pulse shapes discussed below by the method described in detail in [3].

Here, we will now discuss the dynamics in an alternative picture leading naturally to coherent wavefunction translation. The dynamics may be described with reference to a coordinate system following the motion of classical free electron in the time dependent spatially constant electric field as given by the above equations (2) for velocity and (3) for the position of the origin of the new coordinate frame [15]. The transformed Hamiltonian becomes,  $H_0^{\text{KH}} = T^{-1}HT$ , with

$$T = \exp \left[ i\vec{\alpha}(t) \cdot \vec{p} + \int_{t_i}^t A(t')^2 dt' - \vec{A}(t) \cdot \vec{r} \right]. \quad (4)$$

Performing the transformation, we obtain the new Hamiltonian

$$H_0^{\text{KH}} = -\frac{1}{2}\nabla^2 + V[\vec{r} - \vec{\alpha}(t)]. \quad (5)$$

The electronic wavefunction in this frame describes an electron with origin at  $\alpha(t)$ , exposed to a moving potential of the original atomic nucleus. The corresponding translated wavefunction obeys the standard TDSE with the hamiltonian (5). In energetic ion–atom collisions, the moving potential is a Coulomb interaction of the projectile traveling on a classical trajectory  $\vec{R}(t)$ , which appear on equal footing as a target centered stationary potential. Here, the original bounding potential of the core plays the role of the projectile–electron interaction. We now review the model and the method of Briggs and Dimitrovski [14] and connect it with the KH picture. In time dependent quantum mechanics, an initial state at time  $t_i$ ,  $|\Psi_i(t_i)\rangle$  evolves into a final state at time  $t > t_i$  through the time development operator,

$$\Psi(t) = U(t, t_i)\Psi_i(t_i). \quad (6)$$

The time dependent Schrödinger equation then gives the formal expression for the time development operator for  $t \in (t_i, t_f)$

$$U(t, t_i) = e^{-i\int_{t_i}^t H(t') dt'}. \quad (7)$$

The expression is ‘formal’ since, in general, the Hamiltonian does not commute with itself at different times. The Magnus expansion defines an iterative procedure to handle the exponential expansion in increasing complexity [10]. To first order equation (7) is the approximate result. Clearly, the validity of the first order expression is a short interaction timespan  $t_f - t_i$ . Thus, the first order Magnus expansion is sometimes called the impulse approximation in atomic and nuclear collision theory [11, 12]. It can be expected to be valid when the active particle receives a uni-directional impulsive momentum kick within a short interaction time compared to the characteristic time scale of the initial state. In strong field physics, the Magnus expansion applies to a series of strong and short half cycle pulses interacting with a one-electron atom ground state [7, 8] or Rydberg atom traveling on a classical orbit [17].



Consider now an electric field  $\vec{E}(t)$  given by a sum of two  $\delta$ -functions [7],

$$\vec{E}(t) = \vec{A}_0 \delta(t - t_1) - \vec{A}_0 \delta(t - t_2), \quad (8)$$

where  $t_1 (t_2 > t_1)$ . This pulse can be viewed as an approximation to a single cycle pulse with  $t_1$  and  $t_2$  being the times of maximum pulse strength. Inserting this expression in the first order Magnus expansion, we obtain the approximate wavefunction after the second kick,  $t > t_2$ ,

$$\begin{aligned} \Psi_f(t) = & e^{-iH_0(t-t_2)} [e^{i\vec{A}_0 \cdot \vec{r}} e^{-iH_0(t_2-t_1)} e^{-i\vec{A}_0 \cdot \vec{r}}] \\ & \times e^{-iH_0(t_1-t_i)} \Psi_i(t_i). \end{aligned} \quad (9)$$

We identify  $\vec{A}_0$  as the negative constant vector field,  $\vec{A}(t) = -\int_0^t \vec{E}(t') dt'$ . It is nonzero only in the time interval  $(t_1, t_2)$ . This was called the modified Magnus approximation in [7–9] since it involves an additional period of free evolution between the two impulsive interaction regions with the electric field. In general, the free evolution period induces distortions of the original wavefunction. However, under certain conditions of strong and extremely short electric pulses it was shown [14] that the entire initial wavefunction is translated in space without distortion. The necessary conditions behind this phenomenon is now analyzed within the KH frame.

The constant vector potential of a  $\delta$ -function pulse has its direct analog in a fast charged particle traveling on a straight line trajectory at constant velocity  $\vec{v} = \vec{R}$ . The Galilean invariant spectrum of eigenstates in the moving system with velocity ( $\vec{\alpha} = -\vec{A}_0$ ) can be obtained from the system at rest ( $\vec{\alpha} = 0$ ) by providing the eigenstates of the moving system with plane wave translational factors [18]. The moving undistorted states following the  $\delta$ -function kick are then described in the stationary coordinate system as,

$$\Psi_n^{\text{KH}} = e^{-i(\vec{A}_0 \cdot \vec{r} + \frac{1}{2} A_0^2 t)} \Psi_n(\vec{r} - \vec{\alpha}_0, t), \quad (10)$$

where  $\Psi_n$  is an arbitrary eigenstate of the stationary Hamiltonian ( $\alpha = 0$ ). It implies that a ‘single cycle double  $\delta$ -function pulse’ as described by equation (8) takes any initial state of a one-electron atom and translate it from the origin to a state centered around the position  $A_0 \tau$ . Then clearly, for  $A_0 \tau \gg \langle r_n \rangle$ , with  $r_n$  a characteristic radius of the initial state, a localized state without a nucleus can be formed. In general, the wavefunction is completely described by an expansion in all basis states of the moving system,

$$\Psi(\vec{r}, t) = \sum_j c_j \Psi_j^{\text{KH}}(\vec{r} - \vec{\alpha}_0, t). \quad (11)$$

In the following, we will limit the discussion to the part of the expansion including only the bound states, the unbound states are in this context only continuation of the least bound part. The criterion for the formation of a translated localized state identical in shape to the initial wavefunction can be discussed in this model of single velocity boost. This situation has been discussed in several connections in the physics of atomic collisions, known as ionization amplitude by the nucleus recoil, and has been discussed by Migdal already in 1941, as nicely reviewed in somewhat younger work on ionization by neutrons bouncing off the atomic nucleus [19]. There the condition

applies to the opposite process—the state should keep its identity and remain on the moving center, but the conditions are the same. It is the requirement that all expansion coefficients,  $c_j$  in the expression above remain negligible, except for the initial state,  $|c_n| = 1$ . When  $\Psi(\vec{r}, 0) = \Psi_n(\vec{r})$ , the expansion coefficients for a one-electron atom takes the form

$$c_j = \langle \Psi_j^{\text{KH}} | \Psi_n \rangle = \int d^3r \Psi_j^*(\vec{r}) e^{i\vec{A}_0 \cdot \vec{r}} \Psi_n(\vec{r}). \quad (12)$$

The integral can be computed analytically and can be expressed as a finite sum [20],

$$c_j^n = \sum_i a_i \frac{A_0^{k_i}}{(\alpha_{j,n}^2 + A_0^2)^{l_i}} Y_{L_i, M_i}(\hat{A}_0), \quad (13)$$

where  $k_i < l_i$  are integers,  $\alpha_{j,n} = 1/n + 1/j$  and  $Y_{L_i, M_i}$  is a spherical harmonics function of the two angles  $\hat{A}_0 = (\theta_{A_0}, \phi_{A_0})$ . A closer inspection of the expansion coefficients shows that the coupling to other states decreases drastically with increasing initial principal quantum number  $n$ . For example, for  $l_j = m_j = l_n = m_n = 0$  states the leading term of equation (13) takes the form

$$c_j^n \sim \frac{\alpha_{j,n}^3}{(\alpha_{j,n}^2 + A_0^2)^2} \cdot \frac{1}{\sqrt{nj}} \quad (14)$$

which decays fast for increasing initial  $n$  and  $A_0$ . For low values of  $n$ , the decay is slower than for high values, see figure 1, which imply that an initial  $1s$  wavefunction in the moving system will fast expand during its transport on the trajectory  $\alpha(t)$ . On this trajectory it will behave e.g. as a free particle initially fixed in space. Figure 1 also illustrate that for high initial  $n$  states, the components of states different from the initial state fast becomes vanishingly small. As a consequence an initial Rydberg state will keep larger chance to remain in its original shape as it travels on the  $\alpha(t)$  trajectory.

The wave function evolution for two initial states exposed to the double delta function of equation (8) is propagated numerically in time between the start and stop ‘kick’ in figure 2 for the ground state ( $n = 1$ ) and the excited state  $n = 15$ , respectively. To illustrate the dynamics most clearly we have applied two different interaction strengths and time intervals between the kicks. In both cases, the center of the wave function is given by the displacement vector,  $\vec{\alpha}_0(t)$ . We observe, as a consequence of the results in figure 1, that the probability density of the excited state  $n = 15$  (lower panel) propagates with no-distortion in shape. The ground state on the other hand, expands as shown in the upper panel since, for the ground state, the boost coefficients (11) are orders of magnitude larger than the  $n = 15$  state.

For finite pulse cycles equation (10) is no longer exact. The departure from the exact translated ground state can now be assessed by first order theory in the moving frame based on the Hamiltonian

$$H^{\text{KH}} = H_0^{\text{KH}} + V[\vec{r} - \vec{\alpha}(t)] - V[\vec{r} - \vec{\alpha}_0(t)]. \quad (15)$$

The two potentials refer to different displacements, the first to the accelerating frame  $\alpha(t) = -\int_{t_1}^t \vec{A} dt'$  of the real pulse, the second to the constant velocity axillary frame  $\alpha_0(t) = A_0 t$  of

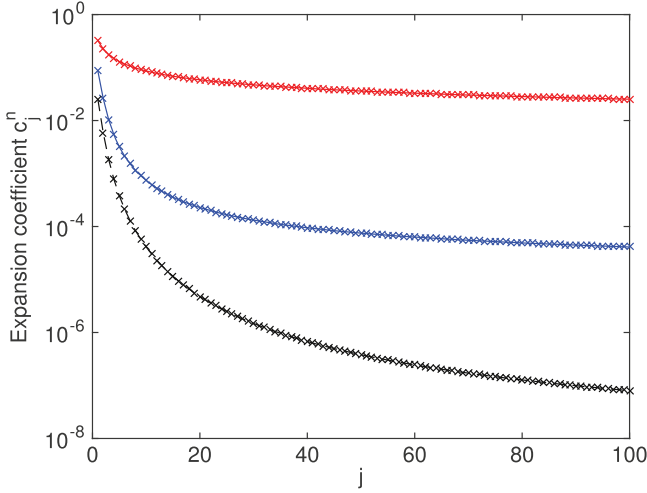


**Figure 1.** Values of the boost expansion coefficients  $c_j^n$  of equation (11) for three initial  $n, s$ —states as function of the principal quantum number denoted by  $j$ . The initial states are  $n = 1$  (red),  $n = 10$  (blue),  $n = 100$  (black) and  $A_0 = 1$  in all three cases.

a  $\delta$ -function pulse. It is convenient to write  $\vec{\alpha}(t) = \vec{\alpha}_0(t) + \vec{\alpha}_1(t)$ . Then  $\alpha_1 \ll \alpha_0$  for a strong and short laser pulse. In case of Coulomb interactions, the perturbing potential of equation (15) can be multipole expanded resulting in the leading term,

$$V[\vec{r} - \vec{\alpha}(t)] - V[\vec{r} - \vec{\alpha}_0(t)] \approx -\frac{\vec{\alpha}_1 \cdot \vec{r}_p}{r_p^3} \quad (16)$$

with  $\vec{r}_p \equiv \vec{r} - \vec{\alpha}_0(t)$ . If the effect of this perturbation is small for any final state, the shape of the initial charge density remains translated and undistorted. The effect of the asymptotic perturbation may be investigated within first order perturbation theory of the system referring to constant velocity translation and for a simple sinusoidal full cycle linear polarized pulse,  $\vec{E}(t) = \vec{e}_z \sin(\omega t)$ ,  $\omega = 2\pi/T$  ( $t \in (0, T)$ ). The initial wavefunction, equation (10) in coordinate representation, becomes  $\Psi_i^{KH}(\vec{r}_p) \exp(-i\varepsilon_i t)$ . The first order amplitude for a transition to another state  $\Psi_f^{KH}$  is

$$a_{fi} = i \int_0^T e^{i(\varepsilon_f - \varepsilon_i)t'} \langle \Psi_f^{KH} | \frac{\vec{r}_p}{r_p^3} | \Psi_i^{KH} \rangle \vec{\alpha}_1(t') dt'. \quad (17)$$

For the plain sine pulse  $\alpha_1(t) = E_0/\omega^2 \sin(\omega t)$ , and by defining  $\omega_{fi} = \varepsilon_f - \varepsilon_i$ , the equation above is brought to the form

$$a_{fi} = i V_{fi}^{KH} \frac{E_0}{\omega^2} \int_0^T e^{i\omega_{fi}t'} \sin(\omega t') dt'. \quad (18)$$

Obviously, the transition amplitude is seen here to fast become vanishingly small for any final state as the photon energy of the central laser frequency exceeds the energy separation between the final and the initial states. The criterion for undistorted translation of a bound state of energy  $\varepsilon_i$  becomes

$$\omega \gg \omega_{fi}, \quad (19)$$

for any final state which are populated through the first order expression, equation (17). Even if based on a simple single

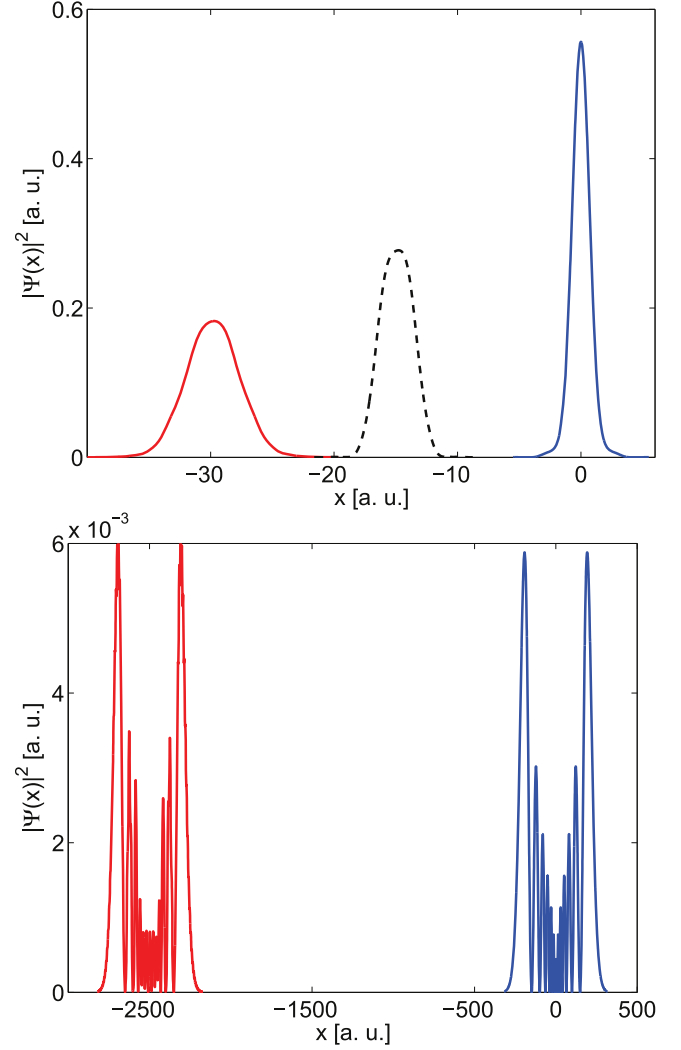


**Figure 2.** Electron probability densities resulting from the propagation of the wavefunction exposed to a pulse represented by two  $\delta$ -function potential equation (8). The upper panel is for the initial ground state  $n = 1$ , the pulse strength  $E_0 = 10$  a.u. and the time between the two interactions are 3 a.u. In the lower part, the initial state is  $n = 15$ , the pulse strength  $E_0 = 10$  a.u. and the time between the two interactions is 250 a.u. At the beginning, the position of the wave function is centered around origo (blue lines) and probability densities at the end at  $t = T$  are shown as red lines. The black dash-dash line (upper panel) shows the position and shape of the translated state  $n = 1$  at the time  $T/2$ . The calculations use the 1D model developed and described in our recent work [3].

cycle pulse, the result is general and can be obtained for any symmetric optical cycle. It contains the criterion from the validity of the Magnus expansion [14] as a special limitation, that the orbital period of the initial state should exceed the optical cycle. In principle, the criterion is never achieved since arbitrary high momentum states exist which are dipole coupled to the initial state. In practice the coupling to high momentum states fast becomes vanishingly small which realize coherent displacement of the initial state. For a ground state hydrogen atom this correspond to a cycle period below 24 as while for excited states the pulse duration may be order of magnitudes longer because of the vanishing small components of states different from the traveling initial state in the expression of

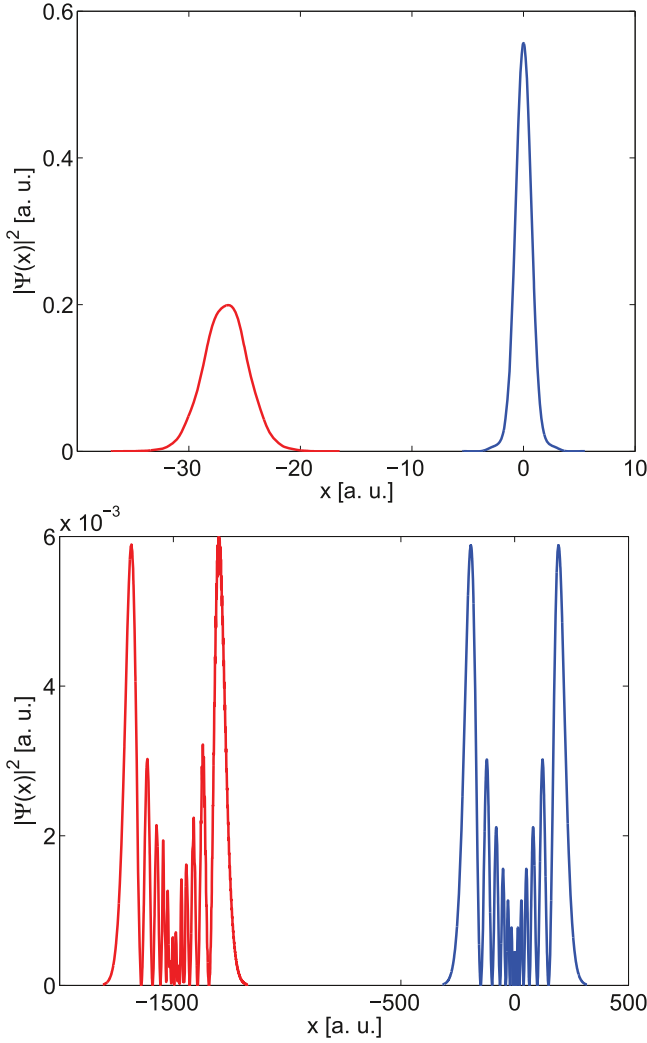


**Figure 3.** Electron probability densities (red curves) resulting from the propagation of the wavefunction exposed to the single-cycle laser pulse of equation (20) with frequency  $\omega = \pi/3$  a.u., pulse strength  $E_0 = 100$  a.u. (upper panel, initial  $n = 1$ ) and  $\omega = \pi/100$  a.u., pulse strength  $E_0 = 5$  a.u. (lower panel, initial  $n = 15$ ). Initially, the ground state  $n = 1$  and excited state  $n = 15$  are centered at origo (blue lines). The calculations use the 1D model developed and described in our recent work [3].

equation (11). Note also that the analysis applies to a sequence of pulses, as well as which allow for the transportation of the initial state as far away from the initial position as given by the total displacement of  $N$  pulses,  $\alpha_N = NE_0/\omega^2$ . For large  $N$ ,  $E_0$  it implies that the initial charge distribution can be translated away from its Coulomb fields, into a ‘observation region’ where the fragmentation spectrum can be analyzed without influence of nuclear charges.

We end by a simple demonstration of the above analysis for pulses of finite duration. The vector potential,

$$A(t) = \frac{E_0}{4\omega} \sin^4(\omega t), \quad t \in (0, T = \pi/\omega) \quad (20)$$

results in a single cycle electric field

$$E(t) = -E_0 \sin^3(\omega t) \cos(\omega t) \quad (21)$$

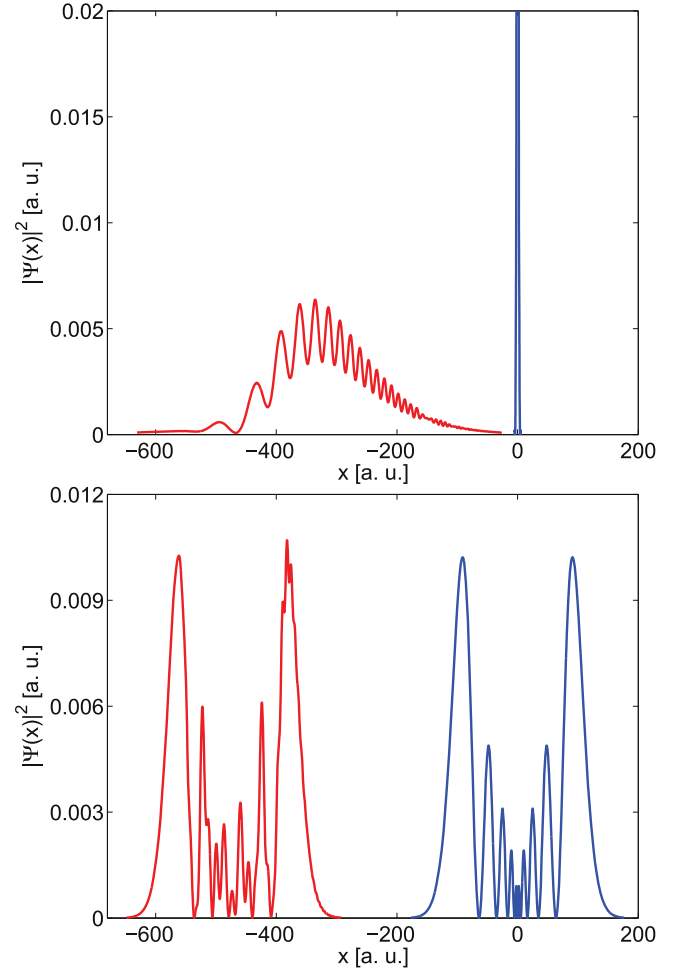


**Figure 4.** Electron probability densities (red curves) resulting from the propagation of the wavefunction exposed to the single-cycle laser pulse of equation (20): upper panel is initial  $n = 1$  and lower panel is initial  $n = 15$ . The pulse strength is  $E_0 = 1$  a.u. and the frequency  $\omega = 0.025$  a.u. in both calculations. Initially, the ground state  $n = 1$  and excited state  $n = 15$  are centered at origo (blue lines). The calculations use the 1D model developed and described in our recent work [3].

and translation

$$\alpha(t) = \underbrace{-\frac{3E_0}{32\omega}t}_{\alpha_0(t)} + \underbrace{\frac{E_0}{128\omega^2}[8\sin(2\omega t) - \sin(4\omega t)]}_{\alpha_1(t)} \quad (22)$$

which at the end of the pulse is  $\alpha(T) = -3E_0\pi/32\omega^2$ .

In figure 3, the wavefunction is evolved in time with two different initial states and laser pulses of the form of equation (20). The final probability densities are seen to follow the same pattern as the  $\delta$ -function pulses, which is expected from the above analysis with the applied pulse parameters. In figure 4, however, the situation changes: we consider a single set of pulse parameters where the ground state no-longer would preserve its shape due to the low frequency of the pulse. In the upper panel of the figure the ground state has, precisely as expected, been distorted in addition to the translation by the pulse. At the same time, this frequency is sufficiently high to be state preserving for high excited states, as indicated by the initial excited state  $n = 10$  in the lower panel of the figure.

### 3. Concluding remarks

In this work, we have performed a new analysis of a phenomenon discovered about a decade ago by Dimitrovsky, Briggs and co-workers [14]: a short intense single cycle electromagnetic pulse can translate an electronic quantum state away from its original position centered around its nucleus to a new center far off the original position and without any significant change of the initial wavefunction. To achieve this for ground state wavefunctions, a field strength order of magnitude stronger than the unit electric field strength needs to be applied within a time scale of just a few attoseconds. For excited states, the criteria become much more realistic and for example a  $10^{14}$  W cm<sup>-2</sup>, 800 nm single cycle pulse applied to Rydberg atoms will translate the atomic state, without serious distortion, to a well defined distance off the original position.

The analysis has been performed for a one-electron system in 1D. However, we stress that the analysis is dimensional independent. It applies in principle equally well to multi-electron systems since the multi-electron translation operator is a simple product of one-electron translation operators, see, equation (4). It will transfer an initial target oriented multi electron state to a common moving frame where exactly the same analysis as here performed for one-electron states can be carried out. Thus, short, strong displacement pulses may become a new imaging technique of correlations, entanglement and time dependent wavepacket development of atomic and molecular and quantum systems.

### Acknowledgments

The research has been supported by a grant from Norwegian Metacenter for Computational Science.

### ORCID iDs

J P Hansen  <https://orcid.org/0000-0002-8735-3153>

### References

- [1] Calegari F, Sansone G, Stagira S, Vozzi C and Nisoli M 2016 *J. Phys. B: At. Mol. Opt. Phys.* **49** 062001
- [2] Schrödinger E 1935 *Naturwissenschaften* **23** 807
- [3] Agueny H, Chovancova M, Hansen J P and Kocbach L 2016 *J. Phys. B: At. Mol. Opt. Phys.* **49** 245002
- [4] Li S and Jones R R 2014 *Phys. Rev. Lett.* **112** 143006
- [5] Chovancova M, Agueny H, Rørstad J J and Hansen J P 2017 *Phys. Rev. A* **96** 023423
- [6] Yang B C and Robicheaux F 2015 *Phys. Rev. A* **91** 043407
- [7] Dimitrovski D, Solov'ev E A and Briggs J S 2004 *Phys. Rev. Lett.* **93** 083003
- [8] Dimitrovski D, Poloczek J and Briggs J S 2006 *J. Phys. B: At. Mol. Opt. Phys.* **39** 3019
- [9] Dimitrovski D, Götz J and Briggs J S 2007 *J. Phys. B: At. Mol. Opt. Phys.* **40** 4355
- [10] Blanes S, Casas F, Oteo J A and Ros J 2009 *Phys. Rep.* **470** 151
- [11] Chew G F and Wick G C 1952 *Phys. Rev.* **85** 636
- [12] Kocbach L 1980 *J. Phys. B: At. Mol. Phys.* **13** L665
- [13] Reinhold C O, Melles M, Shao H H and Burgdörfer J J 1993 *J. Phys. B: At. Mol. Opt. Phys.* **26** L659
- [14] Briggs J S and Dimitrovski D 2008 *New J. Phys.* **10** 025013
- [15] Popov A M, Tikhonova O V and Volkova E A 2003 *J. Phys. B: At. Mol. Opt. Phys.* **36** R125
- [16] Zuo T, Bandrauk A D and Corkum P B 1996 *Chem. Phys. Lett.* **259** 313
- [17] Simonsen S I, Sørngård S A, Førre M and Hansen J P 2012 *Phys. Rev. A* **86** 043423
- [18] Dubois A, Hansen J P and Nielsen S E 1993 *J. Phys. B: At. Mol. Opt. Phys.* **26** 705
- [19] Baur G, Rosel F and Trautmann D 1983 *J. Phys. B: At. Mol. Phys.* **16** L419
- [20] Hansen J P and Dubois A 1992 *Comput. Phys. Commun.* **67** 456

# Appendices



# Atomic Units

Through the thesis Hartree atomic units (a. u.) have been used unless stated otherwise. In this set of units the electronic mass, the elementary charge, the angular momentum and the electrostatic constant are all scaled to unity:  $m_e = e = \hbar = 4\pi\epsilon_0 = 1$ .

Fundamental and derived Hartree atomic units

Quantity	Unit	Physical significance	Value in SI-units
Mass	$m_e$	Electron mass	$9.109\,38 \times 10^{-31}$ kg
Charge	$e$	Absolute value of electron charge	$1.602\,18 \times 10^{-19}$ C
Angular momentum	$\hbar$	Planck constant divided by $2\pi$	$1.054\,57 \times 10^{-34}$ kg
Electrostatic constant	$4\pi\epsilon_0$	$4\pi$ times the permittivity of free space	$1.112\,65 \times 10^{-10}$ Fm <sup>-1</sup>
Length	$a_0 = \frac{\hbar}{m_e c \alpha}$	Bohr radius of atomic hydrogen	$5.291\,77 \times 10^{-11}$ m
Velocity	$v_0 = \alpha c$	Magnitude of electron velocity in first orbit	$2.187\,69 \times 10^6$ ms <sup>-1</sup>
Energy	$E_h = \alpha^2 m_e c^2$	Twice of binding energy of atomic hydrogen	$4.35975 \times 10^{-18}$ J = 27.2114 eV
Frequency	$f = \frac{v_0}{2\pi a_0}$	Angular frequency of electron in first Bohr orbit divided by $2\pi$	$6.579\,69 \times 10^{15}$ s <sup>-1</sup>
Electric field strength	$F_0 = \frac{e}{(4\pi\epsilon_0)a_0^2}$	Strength of the Coulomb field experienced by an electron in the first Bohr orbit of atomic hydrogen	$5.142\,21 \times 10^{11}$ Vm <sup>-1</sup>

Here  $\alpha = e^2/(4\pi\epsilon_0\hbar c) \sim 1/137$  is the fine structure constant.

Hartree atomic units should not be confused with Rydberg atomic units, which are based on slightly different scaling assumptions:  $4\pi\epsilon_0 = 1$ ,  $m_e = 1/2$ ,  $\hbar = 1$  and  $e = 1/\sqrt{2}$ . Consequently the unit of energy in the two systems differs by a factor of two, i.e.,  $E_H = 2E_{\text{Ry}}$ .





---

# Derivation of Quantum Scattering Formulae

---

A one-electron wavefunction  $\Psi(\mathbf{r})$  which has been exposed to a time-dependent from  $(t_i, t_f)$  field may be partly of fully excited or ionized. It takes the following form at  $t_f$ ,

$$\Psi(\mathbf{r}, t_f) = \sum_m a_m(t_f) \Phi_m(\mathbf{r}) + \sum_n f_{i,n}(\Omega, t_f) \frac{e^{ip_n r}}{r} \quad (1)$$

The first part is a sum over bound states while the second is an outgoing wave with  $f_{i,n}$  being the scattering amplitude for scattering into a solid angle element  $\Omega_n$  of the outgoing wave vector when initially the wavefunction is in the state  $\Phi_i(\mathbf{r})$ . At  $t > t_f$   $|a_m|$ ,  $|f_{i,n}|$  does not depend on time. The differential cross section is,

$$\frac{d\sigma}{p^2 dp d\Omega} = |f_{i,n}(\Omega, t_f)|^2 \quad (2)$$

which is the relative (differential) flux of momentum in a direction perpendicular through the solid angle element  $\Omega$ . When using the result of a numerical solution of the TDSE as a starting point for differential fluxes it is implicitly assumed that the wavefunction exist (unit norm) on a large enough grid and that after a time  $t > t_f$  ( $= T/\beta$  in our case), there are no time dependent interactions:  $H = H_0$ . Our wavefunction is then, at  $t = t_f$

$$\Psi(r_i, \theta_j, t_f) = \sum_{l=0}^{L_{max}} f_l(r_i, t_f) e^{i\mathbf{p} \cdot \mathbf{r}} Y_{l,0}(\theta_j). \quad (3)$$

Note that this is the 'reduced' wavefunction, see [?]. All radial functions have been multiplied with  $r$  such that the normalization is simply,

$$1 = \sum_{l=0}^{L_{max}} \int_0^{r_{max}} dr |f_l(r)|^2 \quad (4)$$

Division with ' $r$ ' or needs to be taken into account when equating the numerical wavefunction with Eq. (1). To extract differential quantities one need (and we may in fact always do it like this) to project onto the basis of Coulomb functions existing on the very same grid. From the solution of the Coulomb problem we extract a discrete set of basis functions which are zero at the end of the grid.

But let us first see what happens when we project onto a plane wave basis  $|\mathbf{p}\rangle$ , with

$$\langle \mathbf{r} | \mathbf{p} \rangle = \frac{1}{(2\pi)^{3/2}} e^{i\mathbf{p} \cdot \mathbf{r}} \quad (5)$$

The calculation will involve using a well known expansion of the plane wave as,

$$e^{i\mathbf{p} \cdot \mathbf{r}} = 4\pi \sum_{L,M \in (-L,L)}^{\infty} i^L j_L(pr) Y_{L,M}^*(\hat{p}) Y_{L,M}(\hat{r}) \quad (6)$$

Here  $j_L$  is the spherical Bessel function,  $j_L(x) = \frac{1}{\sqrt{x}} J_{l+0.5}(x)$ .

Then,

$$\langle \mathbf{p} | \Psi \rangle = \sum_{l=0}^{L_{max}} (-i)^l \left[ \sqrt{\frac{2}{\pi}} \int_0^\infty r f_l(r, t) j_l(pr) dr \right] Y_{l,0}(\hat{p}) \quad (7)$$

$$= \sum_{l=0}^{L_{max}} \tilde{f}_l(p) Y_{l,0}(\hat{p}) \quad (8)$$

since  $\int d\hat{r} Y_{L,M}^*(\hat{r}) Y_{l,m}(\hat{r}) = \delta_{L,l} \delta_{M,m}$ . **This is the full time-dependent wavefunction in momentum space.** Clearly, according to the interpretation of quantum mechanics,  $|\sum_{l=0}^{L_{max}} p_i \tilde{f}_l(p_i) Y_{l,0}(\hat{p})|^2 dp$  is the probability of the total wavefunction to have a momentum component  $p_i$ .

We shall be interested in momentum components belonging to outgoing waves, not all momentum components above which also include the contribution from bound states. By expressing the numerical radial wavefunction as a bound part and a continuum part,  $f_l(r, t_f) = f_l^b(r, t_f) + f_l^c(r, t_f)$  it is straight forward to replace  $f_l(r, t)$  by  $f_l^c(r, t_f)$  in the equation above and we obtain,

$$\langle \mathbf{p} | \Psi^c \rangle = \sum_{l=0}^{L_{max}} \left[ \sqrt{\frac{2}{\pi}} \int_0^\infty r f_l^c(r, t) j_l(pr) dr \right] Y_{l,0}(\hat{p}) \quad (9)$$

$$= \sum_{l=0}^{L_{max}} \tilde{f}_l^c(p) Y_{l,0}(\hat{p}) \quad (10)$$

The differential cross section per (scalar) momentum becomes Eq. (9) of the manuscript.

$$\frac{d\sigma}{dp_n} = \int d\hat{p} p^2 |\langle \mathbf{p} | \Psi(\mathbf{r}, t_f) \rangle|^2 = \sum_{l=0}^{L_{max}} |p_n \tilde{f}_l^c(p_n, t_f)|^2 \quad (11)$$

The differential angular resolved cross section can hardly be obtained in this way. That is because the momentum states are not the correct basis of the Coulomb problem. One way to understand this is to consider an alternative basis expansion in terms of the bound states and the discrete continuum states which vanish at  $r = r_{max}$ ,

$$\Psi(\mathbf{r}, t_f) = \sum_m a_m(t_f) \Phi_m(\mathbf{r}) + \sum_n b_n(t_f) \Phi_n^c(\mathbf{r}) \quad (12)$$

The second sum is the discretized representation of the continuum,  $\Phi_n^c(\mathbf{r}) = \phi_{n,l}^c(r; p_n) Y_{l,0}(\hat{r})$ . Now, the projection onto momentum states becomes

$$\langle \mathbf{p} | \Psi \rangle = \sum_{l=0}^{L_{max}} \sum_n (-i)^l \left[ \sqrt{\frac{2}{\pi}} \int_0^\infty r^2 j_l(pr) \phi_n^c(r, p_n) dr \right] b_n(t_f) Y_{l,0}(\hat{p}) \quad (13)$$

The term in the parenthesis is an overlap, in general nonzero for any  $p$ , which makes it very troublesome to compute. In addition, one needs the set of functions  $\phi_n^c(r, p_n)$  on pre-calculated form. This is the basis defined by being radial solutions of  $H_0$  with positive energy and vanishing at  $r_{max}$ . Therefore, when angular quantities which will be considered it would be good if we instead could calculate them directly from the numerical basis at hand, in radial ( $f_l^c(r)$ ) or momentum space ( $\tilde{f}_l^c(p)$ ).

In text books, it is shown that the solution of the Coulomb problem in terms of outgoing regular basis functions (vanishing at  $r \rightarrow 0$ ) can be written in atomic units,  $p = k$ ,  $E = p^2/2$ ,

$$\Psi_C(\mathbf{r}) = 4\pi \sum_{l=0}^{\infty} \sum_n (i)^l e^{i\delta_l} \frac{F_l(\eta; rp)}{pr} Y_{l,0}^*(\hat{p}) Y_{l,0}(\hat{r}) \quad (14)$$

where  $\eta = 1/p$  for hydrogen, the Coulomb phase shift is  $\delta_l(p_i) = \arg[\Gamma(l+1-i/p_i)]$  and  $F_l$  is the solution to the reduced radial Schrödinger equation with the Coulomb potential and has the asymptotic behaviour,

$$F_l \underset{r \rightarrow \infty}{\sim} \sin(pr - \frac{1}{2}l\pi - \eta \ln(2pr) + \delta_l) \quad (15)$$

By comparing, the relation between the continuum basis functions of Eq. (12) and Eq. (15), becomes,

$$\phi_{n,l}^c(r; p_n) = \frac{F_l(\eta; rp_n)}{4\pi r} \quad (16)$$

The expansion in a basis with the correct asymptotic phases is therefore

$$\Psi_C(\mathbf{r}) = \sum_{l=0}^{\infty} \sum_n (i)^l e^{i\delta_l} \phi_{n,l}^c(r; p_n) Y_{l,0}^*(\hat{p}) Y_{l,0}(\hat{r}) \quad (17)$$

This makes projection onto these states particularly simple:

$$\langle \Psi_C(\mathbf{r}) | \Psi(\mathbf{r}, t_f) \rangle = \frac{1}{p} \sum_{l=0}^{L_{\max}} \sum_n (-i)^l e^{-i\delta_l} b_n(t_f) Y_{l,0}(\hat{p}) \quad (18)$$

The differential cross section per momentum again becomes,

$$\frac{d\sigma}{dp_n} = \int d\hat{p} p_n^2 |\langle \Psi_C(\mathbf{r}) | \Psi(\mathbf{r}, t_f) \rangle|^2 = \sum_{l=0}^{L_{\max}} |b_n(t_f)|^2 \quad (19)$$

The sum over  $l$  for fixed  $n$  means to take the sum of probabilities for fixed momentum (or energy). The differential angular cross section becomes,

$$\frac{d\sigma}{d\hat{p}} = \int dp p^2 |\langle \Psi_C(\mathbf{r}) | \Psi(\mathbf{r}, t_f) \rangle|^2 = \sum_n \left| \sum_{l=0}^{L_{\max}} (-i)^l e^{-i\delta_l} b_n(t_f) Y_{l,0}(\hat{p}) \right|^2 \quad (20)$$

cf. Eq. (9) of [54].

The formulae becomes equally simple for a grid expansion since,  $b_n(t_f) = \langle \phi_{n,l}^c(r; p_n) | f_l^c(r, t) \rangle$

$$\langle \Psi_C(\mathbf{r}) | \Psi(\mathbf{r}, t_f) \rangle = \sum_{l=0}^{L_{\max}} \sum_n (-i)^l e^{-i\delta_l} \langle \phi_n | f_l \rangle Y_{l,0}(\hat{p}) \quad (21)$$

$$= \sum_{l=0}^{L_{\max}} (-i)^l e^{-i\delta_l} \tilde{f}_l^c(p, t_f) Y_{l,0}(\hat{p}) \quad (22)$$

The last equation is valid precisely because the sum of projections is exactly equal to the Fourier transform of the continuum part of  $f_l(r, t_f)$ :

$$\sum_n \langle \phi_n | f_l \rangle = \sum_n \langle \phi_n | f_l^c \rangle = \sum_n \int dp \langle \phi_n | p \rangle \langle p | f_l^c \rangle = \tilde{f}_l^c(p) \quad (23)$$

The differential cross sections now becomes,

$$\frac{d\sigma}{dp_n} = \int d\hat{p} p_n^2 |\langle \Psi_C(\mathbf{r}) | \Psi(\mathbf{r}, t_f) \rangle|^2 = \sum_{l=0}^{L_{max}} |p_n \tilde{f}_l^c(p_n, t_f)|^2 \quad (24)$$

and

$$\frac{d\sigma}{dp_n d\hat{p}} = p_n^2 |\langle \Psi_C(\mathbf{r}) | \Psi(\mathbf{r}, t_f) \rangle|^2 = \left| \sum_{l=0}^{L_{max}} (-i)^l e^{-i\delta_l} p_n \tilde{f}_l^c(p_n, t_f) Y_{l,0}(\hat{p}) \right|^2 \quad (25)$$

Observe that Eq. (11) and Eq. (24) are completely identical. This has to do with the definition of  $f_l^c$ : Having subtracted the "bound part" it is implicitly expressed in a basis of positive energy scattering states. However, for left-right (or forward-backward) scattering we have to use Eq. (25) and sum over angles,  $\theta \in (0, \pi/2)$  for forward scattering,  $\theta \in (\pi/2, \pi)$  for backward scattering. The additional phases in the last equation and their consequences are the origin of the new figure.